HUMBOLDT-UNIVERSITÄT ZU BERLIN

Characterization of hybrid solar cells prepared from poly-thiophenes and silicon

---

Dissertation

zur Erlangung des akademischen Grades

doctor rerum naturalium

(Dr. rer. nat.)

im Fach Physik

eingereicht an der

Mathematisch-Naturwissenschaftlichen Fakultät

der Humboldt-Universität zu Berlin

von

Dipl.-Ing. Matthias Karl Ludwig Zellmeier

Präsident der Humboldt-Universität zu Berlin
Prof. Dr. Jan-Hendrik Olbertz

Dekan der Mathematisch-Naturwissenschaftlichen Fakultät
Prof. Dr. Elmar Kulke

Gutachter:
1. Prof. Dr. Norbert Koch
2. Prof. Dr. Norbert H. Nickel
3. Prof. Dr. Norbert Esser

Tag der mündlichen Prüfung: 04.11.2016

Abstract

The scope of this thesis was the development of a hybrid solar cell based on silicon in which the inorganic semiconductor, the organic polymer and the contact system are combined in such a manner to result in a photovoltaic device with high power conversion efficiency. To reach this goal several measures were taken. New polymer materials derived from the prototypical organic semiconductor poly(3-hexylthiophene-2,5-diyl) (P3HT), namely poly(3-[3,6-dioxaheptyl]-thiophene) (P3DOT) and poly(3-[2,5,8-trioxanonyl]-thiophene) (P3TOT), were extensively characterized regarding its structural properties. Poly-thiophene/c-Si hybrid solar cells fabricated from these new polymers exhibited power conversion efficiencies up to 11 %.

The energy level alignment of these poly-thiophene/c-Si hybrid interfaces was studied using photoelectron spectroscopy. Furthermore, the influence of the contact system on the underlying wafer is investigated with surface photovoltage measurements. The measurements revealed the formation of an inversion layer beneath the silicon surface due to the semitransparent metal contact used in the devices. Therefore, these devices can be classified as MIS inversion layer solar cells.

To further improve the hybrid poly-thiophene/c-Si solar cells by substituting the semitransparent metal contact, graphene was implemented in the device design as a transparent front contact. The carbon monolayer only absorbs 2.7 % of the incident light and has excellent electronic properties. The CVD grown graphene sheet had a lateral size of up to 1 cm^2 and was applied onto the solar cell using a non-destructive and water-free transfer process. However, despite the successful transfer the power conversion efficiency was restricted by the low fill factor due to a low charge carrier density in the graphene. A calculation based on the electrical losses indicated that the problem could be overcome by a combination of multilayer graphene and an additional metal grid structure to increase conductivity.

As a last step, hybrid solar cells in the combination P3HT/polycrystalline silicon absorbers on glass were fabricated for the first time. The inverted device structure used for these solar cells proved beneficial for the lifetime. These devices were stable for up to 3 months without additional encapsulation.

Kurzzusammenfassung

Das Hauptaugenmerk dieser Arbeit liegt auf der Entwicklung einer Hybridsolarzelle, in der der anorganische Halbleiter Silizium, das organische Polymer und das Kontaktsystem so aufeinander abgestimmt sind, dass ihre Kombination zu einem Bauelement mit hohem Wirkungsgrad führt. Um dieses Ziel zu erreichen wurden verschiedene Maßnahmen ergriffen. Neue Polymermaterialien, abgeleitet von dem prototypischen organischen Halbleiter poly(3-hexylthiophen-2,5-diyl) (P3HT), namentlich poly(3-[3,6-dioxaheptyl]-thiophen) (P3DOT) und poly(3-[2,5,8-trioxanonyl]-thiophen) (P3TOT), wurden umfassend hinsichtlich ihrer Struktur untersucht. Poly-thiophen/c-Si hybride Solarzellen, hergestellt aus diesen neuen Polymeren, erreichten Effizienzen bis zu 11 %.

Die vollständigen Banddiagramme dieser Poly-thiophen/c-Si Hybridgrenzflächen wurden mittels Photoelektronenspektroskopie aufgenommen. Außerdem wurde der Einfluss des Kontaktsystems auf die darunter liegenden Schichten mittels Oberflächenspannungsspektroskopie untersucht. Das Resultat dieser Messungen weißt eine Inversionslage unter der Siliziumoberfläche nach, die sich aufgrund des verwendeten semitransparenten Metallkontaktes formt. Dadurch lassen sich diese Bauteile als MIS-Inversionsschicht-Solarzelle kategorisieren.

Um die Hybridsolarzellen weiter zu verbessern, wurde versucht den semitransparenten Metallkontakt durch Graphen zu ersetzen. Diese Kohlenstoffmonolage besticht durch eine geringe Absorption von nur 2,7 % bei herausragenden elektronischen Eigenschaften. Das Graphen wurde durch einen CVD-Prozess gewachsen und erreichte eine laterale Ausdehnung von bis zu 1 cm^2. Der Übertrag auf die Solarzelle erfolgte mittels eines Wasser- und Zerstörungsfreiem Transferprozess. Trotz dem erfolgreichen Aufbringen des Graphen limitierte ein geringer Füllfaktor aufgrund der geringen Ladungsträgerdichte im Graphen den Wirkungsgrad der Solarzelle. Eine Berechnung der elektrischen Verluste weist darauf hin, dass eine Kombination aus mehrlagigem Graphen und zusätzlichem Metallkontaktgitter Abhilfe schaffen kann.

In einem letzten Schritt wurde das Polymer P3HT zum ersten Mal mit polykristallinen Siliziumabsorbern auf Glas kombiniert. Die invertierte Zellstruktur, die hierbei zu Anwendung kam, erwies sich als Vorteilhaft für die Lebensdauer der Solarzelle. Diese waren ohne zusätzliche Verkapselung 3 Monate stabil.

Table of contents

1. Introduction

1.1 Why hybrid solar cells?

The term "hybrid" is used to describe a growing variety of combinations of inorganic and organic materials; to name a few, the incorporation of organic molecules in an inorganic matrix (or vice versa) [1,2] for desired physical properties, functionalization of surfaces (grafting) [3], or organic/inorganic heterostructures.

The latter is the approach followed in this work. Silicon and polythiophenes are combined to develop a highly efficient hybrid solar cell. The current is mainly generated in the low band-gap inorganic material which also provides good charge collection due to its superior charge carrier diffusion lengths and intrinsically free charge carriers at room temperature. Furthermore, the concept of the hybrid heterostructure solar cell takes advantage of the simple manufacture of organic materials. The use of solution processing at moderate temperatures on any substrate for the fabrication of electronic devices is desirable for a wide range of applications, with a view of reducing production costs. Efforts to manufacture high quality silicon layers from solution to avoid conventional vacuum processes and vapour-phase deposition were made with some success. High charge carrier mobilities [4] and promising thin-film solar cell efficiencies were achieved [5,6]. However, solution processed silicon layers still rely on high temperatures of ~500 °C to convert the precursor material into silicon thin-films.

Efficiencies of solar cells from conjugated organic materials are still below 12 % [7] despite considerable efforts. While further increases are likely, optimization proofs difficult due to the excitonic nature of organic materials. A generalized formulation of the Shockley-Queisser limit, which takes processes occurring at the donor-acceptor interface into account, predicts significantly lower efficiencies as the classical Schockley-Queisser result for non-excitonic inorganic solar cells [8].

Hybrid solar cells combining n-type silicon as a cathode are a promising and new approach. Publications comprise a variety of organic materials [9–13]. The combinations with the organic materials poly(3,4-ethylenedioxythiophene):poly(styrenesulfonate) (PEDOT:PSS) and poly(3-hexylthiophen-2,5-diyl) (P3HT), both, exceeded efficiencies of 10 % [14,15]. Especially the highly conductive hole transport material PEDOT:PSS on crystalline silicon is subject to many publications with continuously increasing efficiencies [16–19]. The highest efficiency of 17.4 % with an estimated efficiency potential of 21.2 % was achieved in a device using the polymer as the back side contact of the wafer and shows impressively the potential of the concept of the hybrid heterostructure solar cell.

1.2 Scope of the thesis

Despite the relatively short time of development for hybrid heterostructure solar cells impressive results were achieved. However, relevant working principles have scarcely been investigated or are limited to PEDOT:PSS as a hole extraction layer. The excellent conductivity and transparency make the material a good choice for this task. However, while the material is based on polythiophenes, it has the particular purpose of high conductivity and is to that intent doped to its metallic state [20–22]. Generalized conclusions on hybrid inorganic/organic semiconductor devices are therefore difficult to make. Scope of this thesis is the establishment of a c-Si/polythiophene heterostructure design with a relevant efficiency of 10 %. The development of this hybrid solar cell requires the combination of a carefully matched combination of inorganic semiconductor, organic polymer and contact system. The investigations to achieve this ambitious goal include the topics of charge carrier generation mechanism, the influence of the energy level positions and structural properties of the solution processed materials or hydrophilic substitutions on the polymers. Furthermore, the device design is developed to overcome efficiency limiting restrictions. In this context an inverted device structure was realized and the advantages analyzed. Additionally, large-area graphene was tested in the device as a transparent and conductive front

contact. The material combines abundance and high transparency with good electrical properties and uses a non-destructive wet transfer process suitable for the deposition onto soft organic materials.

2. Fundamentals

In this chapter, fundamental aspects and textbook knowledge on which the analysis of the experimental data is based on will be briefly reviewed. Given that silicon is probably the most prototypical semiconductor and therefore subject of many basic textbooks and lectures, it will only be shortly introduced and compared to its organic counterpart. The interested reader is referred to reference [23] or reference [24] for more device principles.

For organic materials the different bond types leading to its characteristic π-conjugation will be introduced. As a next step, the forces between molecules and the consequential structural properties will be included, which directly influence the physical properties of the organic materials. Solution-processable poly(-3alkythiophenes)have been used as the model system.

In the following section, the basics of photovoltaic energy conversion and few important device concepts are discussed, including amorphous silicon/crystalline silicon heterojunction solar cells.

2.1 Inorganic semiconductors

Consider an alternating influence of atoms brought into close proximity. The increasing interaction with decreasing distance of the hull electrons with the core potentials of the next or after the next atoms split the orbitals in binding and antibinding, which eventually will form energy bands. The number of states in every band is the number of atoms making up the solid state body. The smaller the interatomic distance r gets, the further the energy bands split up and the separate states form a continuum at first (see Fig. 1). In this region metals are found. For closer distances a discrete gap without charges, the band gap E_{Gap}, forms. Semiconductors are found in the band-gap region of E_{Gap} = 0.3…3 eV. Below, the thermal excitation from occupied in unoccupied states is too high and leads to an increase of conductivity. These materials are called semi-metals. Higher band gap materials are termed insulators. However, the band gap region interesting for solar energy conversion is between 0.6 eV and 1.8 eV.

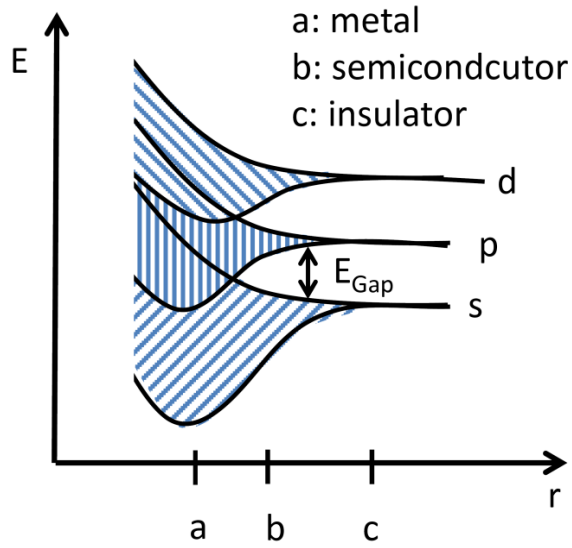

Fig. 1: Widening of the sharp energy levels into bands and finally into a quasi-continuous energy region with decreasing interatomic distance, r (after Slater [25]). s, p and d identify the quantum numbers of orbitals forming the respective bands.

2.1.1 Silicon

Silicon is the most important semiconductor for photovoltaic industry. At present, crystalline silicon (c-Si) devices still constitute around 90 % of the market share [26]. Silicon´s dominant position is the result of the almost ideal band gap of 1.12 eV at room temperature for light harvesting [27] and its abundance in nature. Silicon in the form of silica makes up 28 % of the earth`s crust and silicon is second only to oxygen in abundance.

The solid state of silicon may be roughly classified in two groups from the viewpoint of atomic configuration: crystalline silicon and non-crystalline or amorphous silicon. A crystal is defined as a solid composed of atoms arranged in a three-dimensionally periodic pattern. When the periodicity of the atomic arrangement extends throughout the crystal, it is called a single crystal. A crystalline material in which the periodicity of structure is interrupted at boundaries is called a polycrystalline material and may be seen as a solid formed by many small single crystals, namely grains, interrupted at boundaries.

2.1.2 Crystal structure

The 3-dimensional crystal is described by three primitive basis vectors $\vec{a}$, $\vec{b}$, $\vec{c}$. The crystal remains invariant under translation through any vector that is the sum of integral multiples of the basis vectors. The lattice sites are defined by [23]:

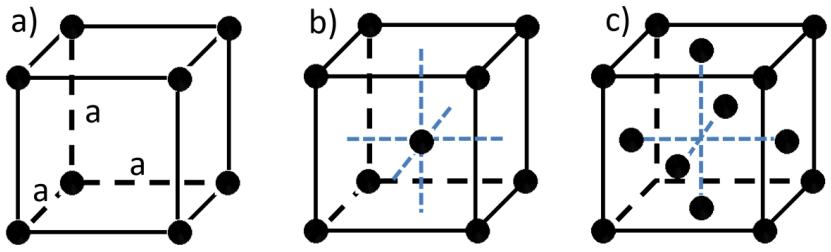

Fig. 2: a) simple cubic (sc), **b)** body-centered cubic (bcc) and **c)** face-centered cubic (fcc) lattice structures. *a* is the lattice constant.

$$\vec{R} = m\vec{a} + n\vec{b} + p\vec{c} \qquad (1)$$

where m, n, and p are integers.

Fig. 2 shows some important cubic unit cells. Cubic unit cells are defined by three equal axes at right angles. Many important semiconductors, e.g. silicon, have a diamond crystal structure (see Fig. 3), in which each atom is surrounded by four equidistant nearest neighbors, which lie at the corners of a tetrahedron. The diamond lattice can be considered as two interpenetrating face-centered cubic lattices shifted by (a/4, a/4, a/4). The lattice constant a of Si at room temperature is 5.43095 Å. For a set of basis vectors, a set of reciprocal lattice basis vectors $\vec{a}^*$, $\vec{b}^*$, $\vec{c}^*$ is defined according to [23]:

$$\vec{a}^* = 2\pi \frac{\vec{b}\times\vec{c}}{a\cdot b\times c} \;, \vec{b}^* = 2\pi \frac{\vec{c}\times\vec{a}}{a\cdot b\times c} \;, \vec{c}^* = 2\pi \frac{\vec{a}\times\vec{b}}{a\cdot b\times c} \quad . \qquad (2)$$

In addition, $\vec{\imath}\cdot\vec{\jmath}^* = 2\pi\cdot\delta_{ij}$ needs to be fulfilled.

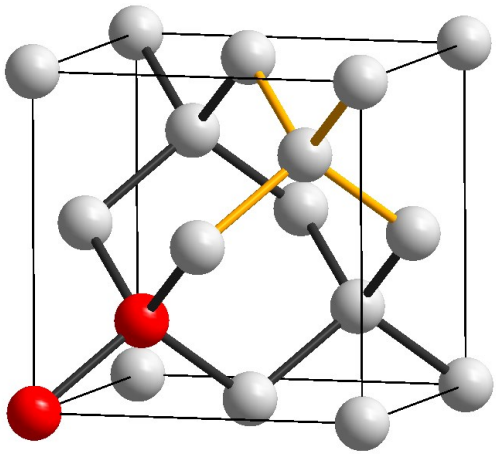

Fig. 3: Diamond structure unit cell build up of two face-centered cubic lattices shifted against each other by (a/4, a/4, a/4). Basis atoms are colored in red. Bonds of the tetrahedal phase of next neigbouring atoms are highlighted in orange.

These vectors define the reciprocal lattice [23]

$$\vec{G} = h\vec{a}^* + k\vec{b}^* + l\vec{c}^* \tag{3}$$

where h, k, l are integers.

h, k, and l are commonly used to define various planes in a crystal as every vector of the reciprocal lattice is normal to a set of planes in the real space lattice. To define these Miller indices the following rules apply:

1. Find the intercept with the three basis axes in multiples of the lattice constant
2. The reciprocal values of these numbers are reduced to the smallest integers having the same ratio
3. The result in brackets (hkl) are the Miller indices for a single plane

Planes with an equivalent symmetry use {hkl}. Crystal directions are identified by [hkl]. <hkl> depicts a full set of equivalent directions.

2.1.3 Electronic structure

The periodic structure of a crystalline solid is of particular importance. It is the basis for the Bloch theorem, which provides solutions $\psi_k(\vec{r})$ for the one-electron Schroedinger equation in the presence of a periodic potential $V(\vec{r})$ with the periodicity of the lattice [23]:

$$\left[-\frac{\hbar^2}{2m}\nabla^2 + V(\vec{r})\right]\psi_k(\vec{r}) = E_k\psi_k(\vec{r}) \quad . \tag{4}$$

$\hbar$ is the reduced Planck´s constant. The solution (Bloch function) is of the form [23]:

$$\psi_k(\vec{r}) = e^{j\vec{k}\vec{r}}U_n(\vec{k},\vec{r}) \quad . \tag{5}$$

$U_n(\vec{k},\vec{r})$ is periodic in $\vec{r}$ with the periodicity of the direct lattice and n is the band index. At two interacting atoms the eigenstates of the individual atoms would split up into two eigenstates of the interacting system.

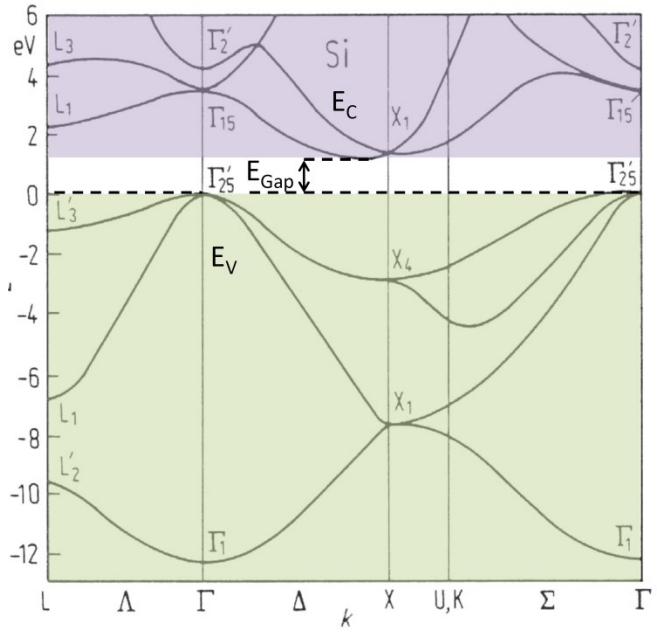

Fig. 4: Energy-band structure of the indirect semiconductor silicon [28]. Conduction (E_C) and valence (E_V) band region are highlighted in color

Those emerging eigenstates are usually not degenerated. In a solid with ~10^{23} atoms cm^{-3} the discrete eigenstates of the single atoms are split into so many new eigenstates so that these can be treated as a continuum. Consequently, the energy bands of a crystal are formed.

Fig. 4 shows the energy-band structure of Si. The band below the energy gap E_{Gap} is called the valence band E_V. The conduction band E_C is located at higher energy. For Si, the conduction band is located close to the X point in the <100>-direction. Thus, it is not at the same point in the k-space as the minimum of the conduction band. Therefore Si is called an indirect semiconductor.

2.1.4 Comparison of organic and inorganic semiconductors

The opto-electronic properties of organic and inorganic semiconductors differ in many aspects. The underlying reasons are found on the atomic scale. Inorganic semiconductors form several eV wide valence and conduction bands, due to the strong bonding among atoms. Transitions between them

dictate the optical absorption. Strong coupling also implies high charge carrier mobility in the order of 10^3 $cm^2\,Vs^{-1}$ with carrier mean free path length exceeding interatomic spacing by far. In organic semiconductors weak coupling between the strongly chemically bonded molecular building blocks define the physical properties. Consequently, the molecular building blocks retain their identity. Valence and conduction bands are small, in the order of several hundred meV [29,30] and the charge carrier mobility is in the range of 1 $cm^2\,Vs^{-1}$. Furthermore, inorganic semiconductors have high dielectric constants of $\epsilon \geq 10$and the binding energies of the Wannier-like excitons are in the order of 10 meV. Exzitonic effects are only noticeable at low temperatures and optically generated charges at room temperature can be considered as intrinsically free. In organic semiconductors the dielectric constant is in the order of 3-4 and the coulombic binding energy of the electron-hole pair is larger than k_BT at room temperature. Electron-hole pairs confined to a single molecule (Frenkel excitons) have to overcome the excitonic binding energy which is in the range of 1 eV [31]. As a consequence, absorption and luminescence spectra resemble those of the molecular building blocks

Tab. 1: Comparison of crystalline silicon, amorphous silicon and the prototypical organic semiconductor crystalline anthracene. Please note that the range of values for mobility and dielectric constant is due to the anisotropic properties of the different crystal directions in anthracene, while variations in a-Si are caused by different preparation methods or sample history.

	crystalline silicon (c-Si)	amorphous silicon (a-Si)	anthracene ($C_{14}H_{10}$)
type	indirect	indirect	excitonic
E_{Gap}(T=300 K) [eV]	1.12 [23]	1.1 - 1.8 [32]	4.1 [31]
mobility e/h [cm^2/Vs]	1500/450 [23]	0.003 - 0.8 / 10^{-4} [32]	0.39 - 1.73 / 0.73 - 2.07 [32]
exciton binding energy [eV]	15.01×10^{-3} [33]	-	1.0 [34]
melting temperature [K]	1688 [23]	1420 [35]	489.0 [32]
density [g/cm^3]	2.328 [23]	≈ 2.21 [36]	1.28 [32]
dielectric constant	11.9 [23]	-	2.9 - 4.11 [32]

2.2 Organic semiconductors

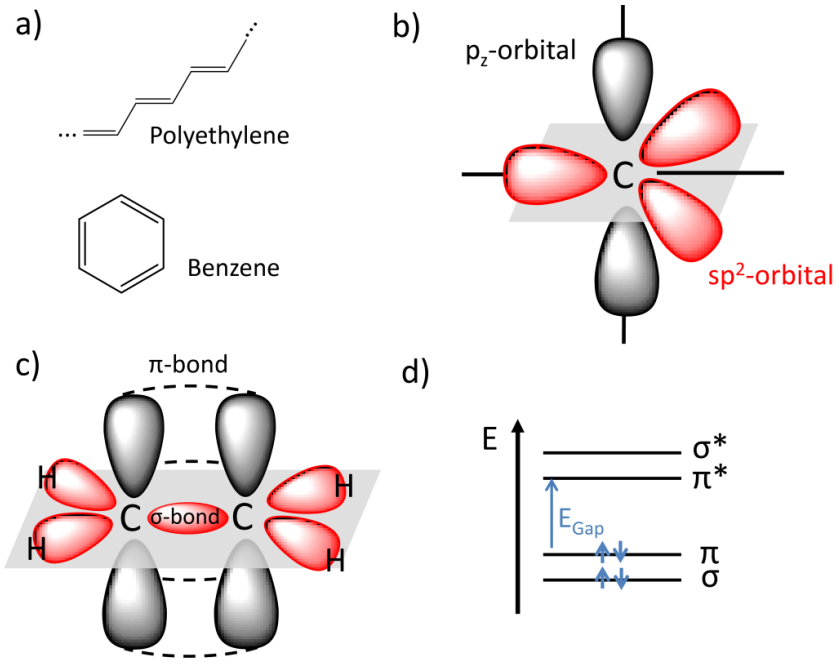

Fig. 5: a) Polyethylene and Benzene as examples for conjugated systems with an alternating single and double bond system. **b)** sp^2 hybridized carbon atoms feature three sp^2 orbitals in a common plane and the perpendicular p_z-orbital. **c)** In ethylene, $H_2C = CH_2$, two sp^2 orbitals form the σ-bond between two adjacent carbon atoms. The p_z orbitals form the delocalized π-bonds. In **d)** the energetic relations of the bonds in ethylene are sketched (* denotes antibonding character of some orbitals). E_{Gap} is connected to lower excitation energy of the weakly bound π-system.

modified by crystal effects. Generally, organic molecular and polymeric semiconductors are hydrocarbon-based compounds in which the electrons form a conjugated system of alternating single and double-bonds. This alternating bonding sequence either forms the backbone of a polymer or the aromatic ring system of polycyclic hydrocarbons (see Fig. 5). In both cases we can distinguish between two types of chemical bonding, the σ-bonds and the π-bonds (or π-electrons). The σ-bonds are formed from the sp^2 hybrid orbitals of two neighboring C atoms or from the sp^2 hybrid orbital of one C atom and the 1s orbital of an H atom in a common plane. The π-bonds are formed by the p_z orbitals and are oriented perpendicular to plane of the sp^2 hybrid orbitals.

The σ-bonds are strongly localized and form the skeleton of the molecule due to the strongly reduced energy compared to the four valence electrons of the free carbon atom. The spatial extent of a p_z orbital is small and therefore only form weakly bonds compared to σ-bonds. However, these bonds form the delocalized π-electron system. Since the π-electrons are only weakly bound, they have the lowest electronic excitation energy of the molecule. The ground-state electron-occupied π-orbital with the highest energy (highest occupied molecular orbital, HOMO) and the unoccupied π orbital with the lowest energy (lowest unoccupied molecular orbital, LUMO) are of particular importance for the semiconducting properties of these materials. To be more specific, the energy difference between HOMO- and LUMO-states gives rise to the band gap of the material and enables optical light absorption and emission.

2.2.1 Bonding forces in organic semiconductors

The physical properties of an organic crystal are not only determined by the features of its building blocks. The interactions between molecules determine the structure of a crystal and are therefore fundamental to the understanding of properties like charge carrier mobility. The following section will discuss the forces leading to the crystallization between neutral and nonpolar molecules.

Attractive forces

The interaction between neutral and nonpolar molecules is related to the interaction between two permanent dipoles $|\vec{p}_1|$and $|\vec{p}_2|$ with a distance *r* from each other. For a parallel orientation the interaction can be described as follows [37]:

$$F = -\frac{dV}{dr} = -\frac{1}{4\varepsilon_0\pi}\frac{6|\vec{p}_1||\vec{p}_2|}{r^4} \qquad (6)$$

where ε_0 denotes the dielectric constant.

A similar attractive force is developed between a permanent dipole and a polarizable nonpolar molecule. The nonpolar molecule has a polarizability α due to the large π-conjugated electron system. The electric field of the permanent dipole causes an induced dipole moment $|\vec{p}_{ind}|$ proportional to the electric field $|\vec{E}|$, resulting in the attractive force [37]

$$F = -\frac{1}{4\varepsilon_0\pi}\frac{6|\vec{p}_1||\vec{p}_{ind}|}{r^4} = -\frac{1}{4\varepsilon_0\pi}\frac{6|\vec{p}_1|}{r^4}\alpha|\vec{E}| = -\frac{1}{(4\varepsilon_0\pi)^2}\frac{12|\vec{p}_1|^2\alpha}{r^7} \qquad (7)$$

and their potential energy [37]

$$V = -\int_0^r F dr = -\frac{1}{(4\varepsilon_0\pi)^2}\frac{2|\vec{p}_1|^2\alpha}{r^6} = -\frac{A}{r^6} \quad . \qquad (8)$$

A similar term can be derived between two neutral, nonpolar molecules without a permanent molecular dipole. The cause for the van der Waals force or dispersive force is the fluctuating dipole moment due to temporarily fluctuations in the charge distribution on a very short time scale. These fluctuating dipoles induce dipoles in neighboring molecules resulting in an attractive force according to [37]:

$$F = -\frac{1}{(4\varepsilon_0\pi)^2}\frac{A'\alpha^2}{r^7} \quad . \qquad (9)$$

The factor A' is specific to the molecule and takes form and symmetry of the molecule into account. The corresponding potential is proportional to r^{-6} [37]:

$$V = -\frac{1}{(4\varepsilon_0\pi)^2}\frac{A'\alpha^2}{6r^6} \quad . \qquad (10)$$

As a consequence, the dispersive forces between organic molecules is short range and weak compared to other forces, e.g. ionic interactions (see Tab. 2).

Repulsive forces

Additionally to the attractive forces, repulsive forces become significant at very small distances. These forces are caused by the Pauli or Coulomb repulsion of the electrons and prevent the collapse of the crystal. Often the Lennard-Jones potential is used to describe the sum of attractive and repulsive potentials as an effective potential [37]:

$$V = \frac{B}{r^{12}} - \frac{A}{r^6} \quad . \tag{11}$$

B and A are empirical constants. The minimum energy position defined by $^{dV}/_{dr} = 0$ determines the equilibrium distance r_0.

Tab. 2: Comparison of different molecular interactions [taken from [38]].

interaction	proportionality of potential to distance r	typical bond energies kj mol^{-1}
ion-ion	r^{-1}	250
ion-dipole	r^{-2}	15
dipole-dipole (permanent)	r^{-3}	2
dipole-dipole (induced)	r^{-6}	0.2
dispersion	r^{-6}	2

2.2.2 Polythiophene semiconductors

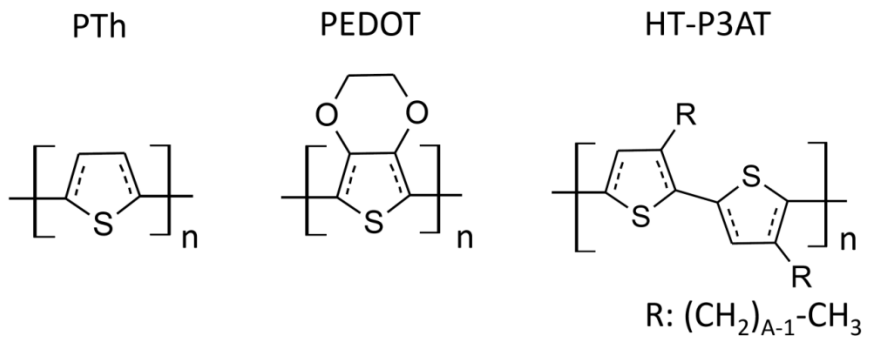

Fig. 6: Examples of poly-thiophenes: Poly(thiophene-2, 5-diyl) (PTh), poly(ethylenedioxythiophene) (PEDOT), head-to-tail coupled poly(3-alkylthiophene-2, 5-diyl) (HT-P3AT). R illustrates the possibility of different alkyl chain lengths in P3ATs.

Unsubstituted polythiophenes (PTh) are insoluble materials which cannot be processed from solution. PTs with substituents such as alkyl chains are soluble in common organic solvents and have been widely studied. PTs are intrinsically semiconducting and a variety has been explored for the use in different application, e.g. organic field effect transistors [39], organic light emitting diodes [40] and organic solar cells [41]. Poly-thiophene and the probably most common representatives are shown in Fig. 6. P-doped poly(3,4-ethylenedioxythiophene) is already used in an industrial scale in capacitor electrodes and as an antistatic material. Sufficiently long alkyl side-chains on poly(3-alkylthiophenes) provide the solubility needed for processing and head-to-tail coupling of the polymer repeating units helps to promote self-assembly of a microcrystalline structure.

2.2.3 Self-assembled microcrystalline polyalkylthiophenes

Weak van-der-Waals interactions are the attractive forces in molecular crystals. Taking into account the strong repulsive forces one can expect the molecules to crystallize in an ordered dense packed structure. Packing coefficients, the volume of molecules in the unit cell in relation to the unit cell, range in the order of 0.68 (benzene) up to 0.80 (perylene) [37]. The optimum

packing for molecular crystals consisting of oligacenes, e.g. naphtalene or anthracene, is reached in a “herringbone” structure, consisting of two molecules in the unit cell. This packing takes into account that seemingly planar molecules have a structure due to the electron cloud around them. The positions of the atoms in the molecule correlate to “hills” and the space in between to “valleys”. In the densest packing structure the positions of these “hills” is subtended to the positions of “valleys” in the neighboring molecules. This principle can be transferred to related organic materials; in this case polyalkylthiophenes. The cofacial π-π-stacking of this material class, which will be described in more detail in the next paragraph for poly(3-hexylthiophene-2, 5-diyl) (P3HT), is subjected to the same binding forces as described above. As a consequence, two neighboring polymer chains are shifted parallel to each other along the polymer chain by one thiophene ring. Thereby the direct facing of sulfur atoms in neighboring chains with its high electron density is avoided.

2.2.4 The crystalline structure of poly(3-alkythiophene)

P3HT belongs to the class of P3ATs with hexyl side chains (C_6H_{13}) attached to the 3rd position of every thiophene ring (see Fig. 6). For head-to-tail repeating units of the monomer, the formation of a lamellar structural order has been observed for solution processed thin-films. These polymers with a lamellar π-stack show a phase separation. Highly ordered domains are embedded in an amorphous matrix and the behavior is usually referred to as semi-crystallinity. The portion of crystalline and amorphous regions in the film is strongly dependent on preparation conditions [42], molecular weight [43], or solvents [44]. The crystalline regions promote the charge transport in the material due to the highly delocalized π-conjugated system of the coplanar polymer chains. These ordered domains are formed by the alignment of planarized and cofacial-stacked polymer chains with a π-π-interaction in the [010] - crystallographic direction of the orthogonal unit cell (see Fig. 7). Along the [100] - direction the spacing is determined by the hexyl side chain. Consequently, this value changes for other P3ATs with different chain

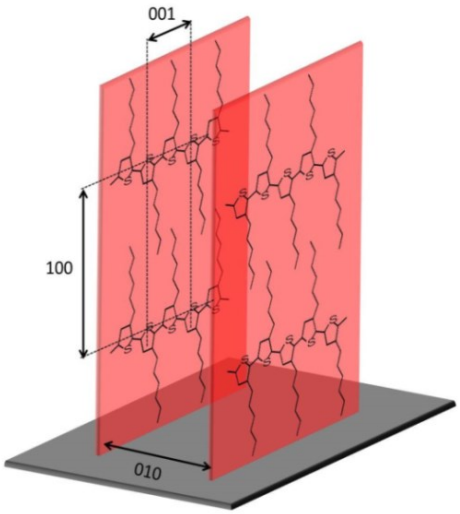

Orthogonal unit cell parameters:

(100)	16.63 Å
(010)	7.75 Å
(001)	7.77 Å
calculated density:	1.11 g/cm^3

Fig. 7: Sketch of the crystalline structure for P3HT and correspondig unit cell parameters [values taken from [45]].

length [45,46]. In the case of P3HT, the largest spacing between the polymer backbones prevents π-π-interaction. In the crystalline structure, the [001] - direction is formed by the planar backbone of the polymer. High resolution structural measurements reveal that ordered domains occur as fibril or needle-like structures. The planar poly-thiophene backbones are oriented perpendicular to the long axis of the fibril. Furthermore, the contour length of the polymer correlates with the fibril width for low and medium molecular weight polymer materials [47]. In disordered domains ring-to-ring torsion and kinks along the polymer chain disrupt the π - conjugation of the backbone, leading to a wide distribution of conjugation length.

The current notion of high-performance, high-mobility P3HT features a microstructure in which the well-conducting and crystalline regions are bridged by single polymer strands. The connectivity between adjacent ordered parts helps to overcome the energetic offset between crystalline and amorphous regions. Hence, high mobility polymers comprise a microstructure with a sufficiently large crystalline fraction, creating a network to sustain an efficient charge transport [48–50].

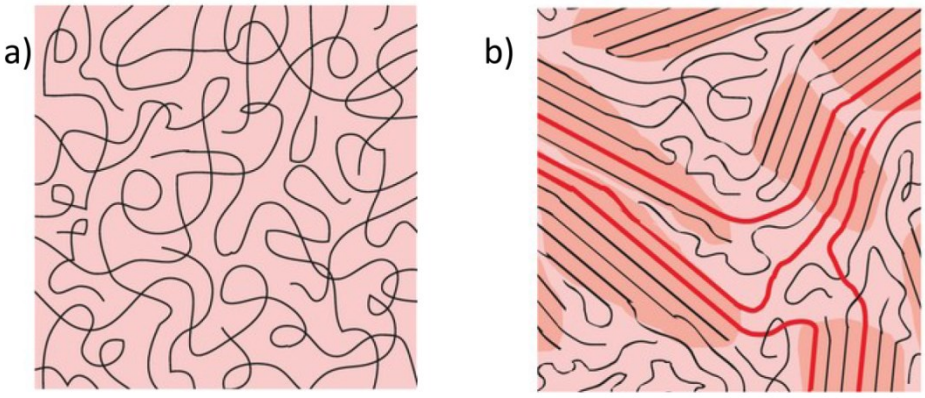

Fig. 8: Sketch of the P3HT morphology for **a)** fully amorphous and **b)** high performance layer consisting of amorphous and crystalline regions. Nearby crystalline regions are bridged by single polymer strands [taken from [50]].

2.2.5 Absorption of visible light in linear π-stacked polyalkylthiophenes

Absorption of photons in the energy range of visible light is connected to an interaction in with the outer shell electrons, the valence electrons of the atoms. The time scale, in which the absorption occurs is about 10^{-15} s. The vibrations of atomic nuclei occur on a time scale of 10^{-12} s. The positions of the atomic nuclei are not changed during the absorption of visible light. The absorption of a photon with an energy hν by a polymer/molecule is similar. The molecule needs to have excitable energy states of the corresponding photon energy $h\nu = E_n - E_0$. Here, E_n and E_0 denote an excited state and the ground state, respectively (see Fig. 5 d): π-π*-transition). From a quantum mechanical point of view, the transition between the two energy states causes a change in the charge distribution and therefore to a change of the dipole moment. The absorption is allowed, if the transition dipole moment is nonzero. The rate of transition k_{if} between an initial state Ψ_i and a final state Ψ_f is described by the well-known *Fermi's golden rule* [51]:

$$k_{if} = \frac{2\pi}{\hbar}\left|\langle\Psi_f|\mathcal{H}'|\Psi_i\rangle\right|^2\rho \quad . \tag{12}$$

$\mathcal{H}'$ describes the perturbing Hamiltonian that causes the transition, e.g. the absorbed light, and ρ is the density of final states. With the complete molecular wave function $\Psi_{total} = \Psi_{el}\Psi_{spin}\Psi_{vib}$ and the dipole operator, $e\hat{r}$, for the Hamiltonian we obtain [51]:

$$k_{if} = \frac{2\pi}{\hbar}\rho\left|\langle\Psi_{el,f}|e\hat{r}|\Psi_{el,i}\rangle\right|^2\left|\langle\Psi_{spin,f}|\Psi_{spin,i}\rangle\right|^2\left|\langle\Psi_{vib,f}|\Psi_{vib,i}\rangle\right|^2 \quad . \quad (13)$$

Spins would only be affected by the magnetic component of light and are therefore neglected. The nuclei are to slow to response to interact with the disturbance. As a consequence, the dipole operator only affects the electronic factor (see 13). However, the macroscopic intensity of absorption depends

Tab. 3: Transitions and corresponding optical absorption [taken from [52]]

transition type	**absorption region [nm]**	**extinction coefficient [mol^{-1} cm^{-1}]**
$\sigma \longrightarrow \sigma^*$	100-200	10^3
n$\longrightarrow\sigma^*$	150-250	10^2-10^4
$\pi \longrightarrow \pi^*$		10^2-10^4
isolated π-bonds	180-250	
conjugated π-bonds	220-IR	
n$\longrightarrow\pi^*$		1-400
isolated groups	220-320	
conjugated segments	250-IR	

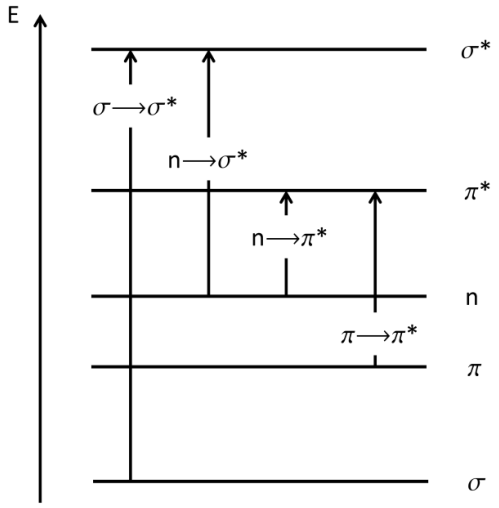

Fig. 9: Energetic positions of molecular orbitals (not to scale) and possible transitions induced by absorption. π- and σ-transitions occur on the same molecule, n denotes possible transitions from non-bonding orbitals. * marks non-binding character of some orbitals.

on all three factors. If the value for the integral $\langle \Psi_{el,f} | e\hat{r} | \Psi_{el,i} \rangle$ is different from zero, a transition is dipole-allowed, if not the transition is dipole-forbidden. Furthermore, the value of the integral is connected to the overlap of the final and initial wave functions. Transitions rates of orbitals located on the same molecule (π -π*-transitions or σ-σ*-transitions) have higher overlaps than transitions involving molecules on different sites. Examples are charge-transfer (CT) transitions or transitions from nonbonding n orbitals, which are located on heteroatoms like oxygen, nitrogen or phosphorus. Possible transitions always occur from a ground state to a higher energy π*- or σ*-orbital. The possible transitions are summarized in Fig. 9. Furthermore, the value of the integral will increase for well extended orbitals as the value for the transition dipole increases. As a consequence, absorption and fluorescence intensity increases with oligomer length [53]. The optical properties of different transitions are compared in Tab. 3. The value for the spin integral $\langle \Psi_{spin,f} | \Psi_{spin,i} \rangle$ is either 0 if the spin of the initial and final state differ or 1 if they are equal. Hence, only transitions between triplet states or

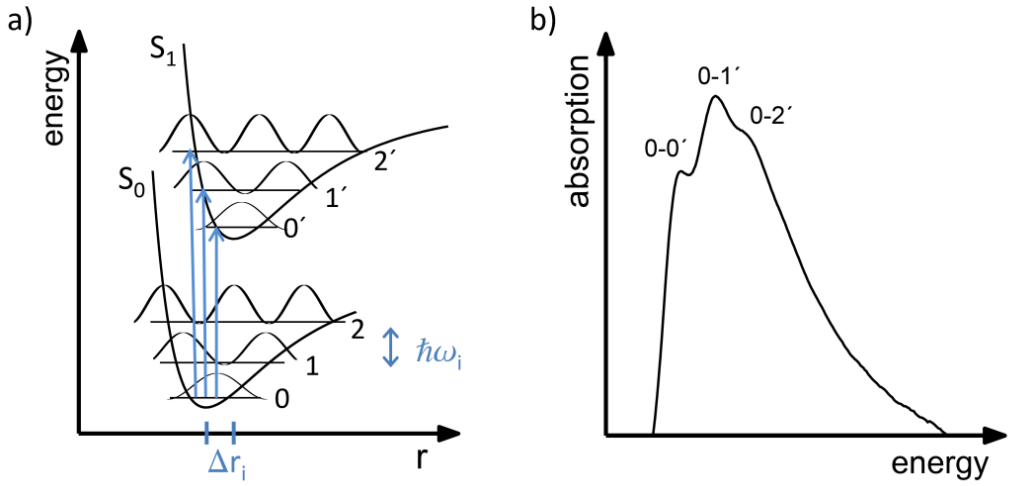

Fig. 10: a) Schematic of the Franck-Condon principle ($\Delta r = 0$ during transition). Transition arrows indicate how the overlap of the vibrational wave functions can determine the shape of the absorption. **b)** Absorption spectrum with vibrational transitions indexed.

singlet states are spin-allowed. However, fluorescence is an experimentally observed luminescence originating from the $T_1 \longrightarrow S_0$ transition. To explain this spin-forbidden transition, one has to take spin-orbit coupling into account. The interested reader is referred to [54].While the electronic part of (13) controls the intensity of the transition, the integral $\langle \Psi_{vib,f} | \Psi_{vib,i} \rangle$ is responsible for the shape. Absorption takes place from the zeroth vibrational level of the ground state into one of the vibrational levels of the excited state. Typical quantization of vibrational energy levels is in the order of 100-300 meV [51]. As shown in Fig. 10 the potential energy curve of the excited state S_i is displaced by Δr_i along the binding distance axis *r*. A descriptive explanation is quite straightforward. In the excited state the one electron of the molecule is elevated to an antibonding orbital, leading to a reduced electron density between the atomic cores and therefore a larger equilibrium distance (see section 2.2.1). The intensity of the absorption correlates with the overlap of the vibrational wave functions $\langle \Psi_{vib,f} | \Psi_{vib,i} \rangle$ and the integral of the Franck-Condon-overlap. The square $|\langle \Psi_{vib,f} | \Psi_{vib,i} \rangle|^2$ is called the Franck-Condon-factor F and describes the probability for a transition from the 0^{th}

vibrational level of the ground state to the m[th] vibrational level of the excited state [51]:

$$\left|\langle \Psi_{vib,f} | \Psi_{vib,i} \rangle\right|^2 = \frac{S}{m!} e^{-S} \quad . \qquad (14)$$

S is the Huang-Rhys-parameter, which describes the coupling of an electronic transition to a vibrational excitation. For a stiff molecule with rigid bonds and a small displacement Δr, usually, the 0-0´ transition is dominant. For a more flexible molecule higher vibrational molecules can form the peak with the highest intensity (see Fig. 10b).

In amorphous films or solutions these peaks of the superposed vibronic transitions are not visible. An inhomogeneous broadening of the π-π*-transition due to a wider distribution of conjugation lengths at a lower mean chain length is the reason [55]. In crystalline regions polyalkylthiophenes chains are planarized with a board-like system of extended polymer backbones. The degree of planarity and therefore effective conjugation length is dependent on molecular weight [48], choice of solvent [56] and temperature [57]. As an example, the thermochroism in P3ATs, which is a pronounced hypsochromic shift with heating, was explained by an increasing twist between neighboring thiophene rings. The twist out of planar configuration of the backbone is accompanied by a reduced effective conjugation length what in turn leads to the blue shift in the absorption spectrum.

2.3 Current-voltage characteristics and solar cell parameters

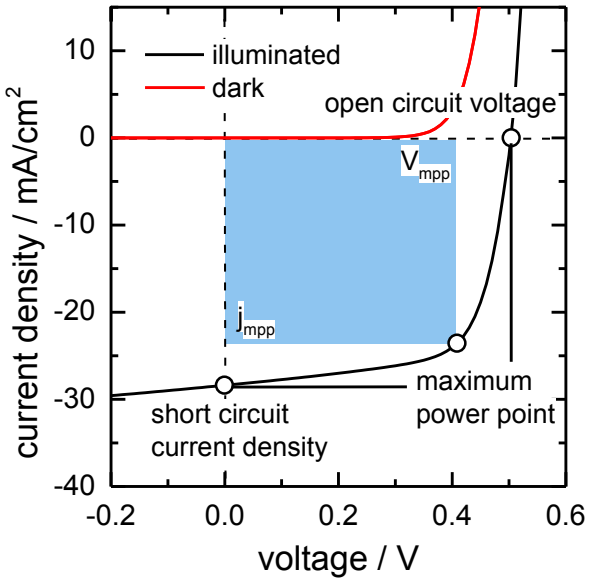

Fig. 11: Example of a current density – voltage (j(V)) curve in the dark and under illumination

The most important parameter describing the performance of a solar cell is the maximum power conversion efficiency, η, which is defined as the ratio between the maximum power point P_{mpp} and the incident radiation power P_L[58]:

$$\eta = \frac{P_{mpp}}{P_L} \quad . \tag{15}$$

P_{mpp} can be calculated from characteristic parameters of the solar cells, i.e. the open circuit voltage V_{OC}, the short circuit current density j_{SC}, and the fill factor FF. The values for these parameters can be determined from the j(V)-curve under illumination as presented in Fig. 11. V_{OC} is defined as the intercept with the voltage axis at which no net current is flowing. The short circuit current density is the current flowing under illumination without an applied external voltage. The fill factor describes the ration between the maximum power and

the product of V_{OC} and j_{SC}. The fill factor describes the "squareness" of the j(V)-curve. Equation (15) can be rephrased as [58]:

$$\eta = \frac{P_{mpp}}{P_L} = \frac{V_{mpp} \cdot j_{mpp}}{P_L} = \frac{V_{OC} \cdot j_{SC} \cdot FF}{P_L} \quad . \qquad (16)$$

V_{mpp} and j_{mpp} term the current density and voltage at the maximum power point.

The parameters V_{OC}, j_{SC} and FF are ultimately limited by the material`s properties making up the solar cell. An upper limit for the open circuit voltage of a solar cell is obviously the band gap. Lower values are caused by recombination processes in the material. Additionally, unavoidable black body radiation at room temperature limits V_{OC} and η what is known as the detailed balance limit [27]. A less general case will be explained in the following. Assuming a pn-junction in thermal equilibrium, the net current flow is zero and the Fermi-energy is constant [58] and we obtain:

$$E^0_{F(p)} = E^0_{F(n)} = E_{F0} \quad . \qquad (17)$$

The Fermi-energy is closer to the valence band edge in the neutral region at the p-type doped side ($E^0_{F(p)}$) and closer to the conduction band edge in the neutral region in the n-type doped side ($E^0_{F(n)}$) of the p/n-junction (see Fig. 12 a). In alignment, both values have the energy E_{F0}. By forming a contact of the two materials, a diffusion current of holes flows from the p-side into the n-side and electrons from the n- inte the p-side, respectively. the current leads to the evolution of a space charge region (SCR) and an increasing potential difference between p- and n-side until the drift current due to this field compensates the diffusion current. As a result the band diagramm with the electrostatic potential U_D shown in Fig. 12 is formed. U_D depends on the doping densities in N_A and N_D in the respective semiconductor and can be calculated to [58]:

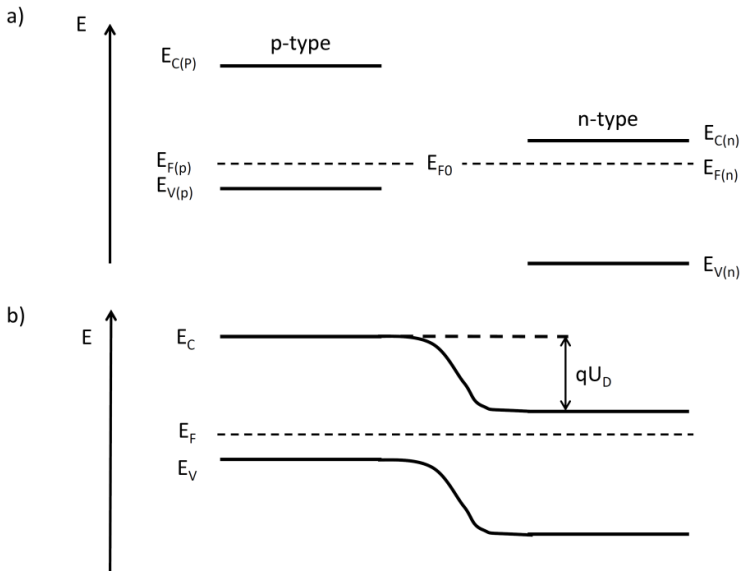

Fig. 12: a) Alignment of the Fermi-energy of contacted p-type and n-type doped semiconductors in thermal equilibirium. **b)** Schematic band diagram of a pn-junction in the thermal equilibrium. U_D denotes the diffusion potential of a pn-junction.

$$U_D = \frac{k_B \cdot T}{q} \cdot ln \frac{N_A \cdot N_D}{n_i^2} \quad , \tag{18}$$

where n_i is the intrinsic charge carrier density. U_D is the upper limit of the open-circuit voltage for a pn-homojunction when only diffusion currents are taken into account. Furthermore, higher doping densities of the p- or n-doped semiconductor or of both and the use of materials with lower intrinsic charge carrier densities will lead to an increase in V_{OC}. However, the useful doping range is limited by intrinsic processes, e.g. radiative or Auger recombination. For $N_A \cdot N_D = 10^{32}$ cm^{-6} a value of 693 mV is the calculated limit of V_{OC} by assuming diffusion currents only as the restricting factor. This limitation is the reason why silicon heterojunctions replaced the homojunction in terms of efficiency.

2.4 The a-Si:H/c-Si heterojunction – a brief introduction

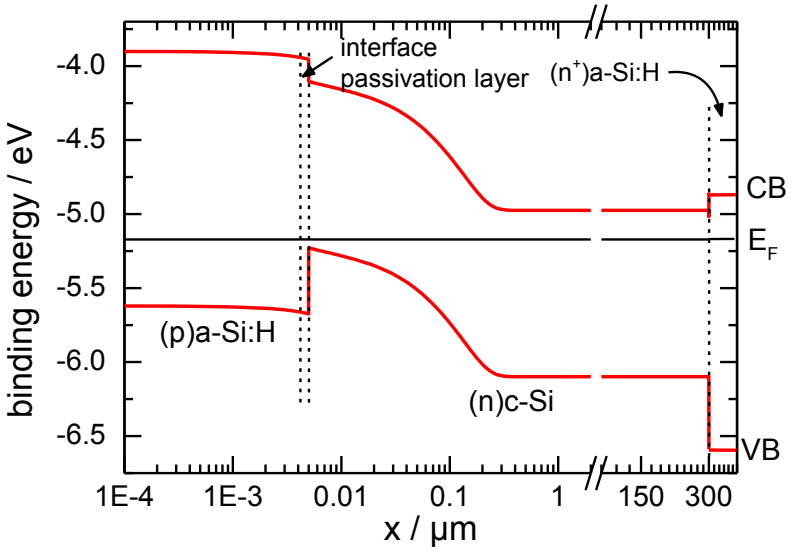

Fig. 13: Energy level alignment of an a-Si:H/c-Si heterojunction solar cell as calculated by the numerical device simulator AFORS-HET [59] using a n-type c-Si substrate and a p-doped a-Si:H emitter layer. Charge carrier selectivity is additionally achieved by the asymmetric band offsets provided by the (p)a-Si:H emitter and the (n^+)a-Si:H backside (back-surface field).

A device design which needs to be presented in an own chapter is the amorphous silicon/crystalline silicon (a-Si:H/c-Si) heterojunction.solar cell, often sloppy termed silicon heterojunction (SHJ). The a-Si:H/c-Si heterojunction combines thin-film techniques with Si wafer technology for a high-efficiency concept. Currently, this cell type holds the power conversion efficiency record for Si wafer-based solar cells. Panasonic presented a large area cell with 25.6 % [60], which is close to the theoretical limit of 29 % for a c-Si based solar cell [61]. The device combines a high band gap amorphous semiconductor, e.g. amorphous silicon, with a crystalline silicon absorber. The resulting band lineup of such a device is sketched in Fig. 13. The advantage of this concept is the high V_{OC} potential. While the highly doped emitter regions in homojunctions limit the open circuit voltage to about V_{OC} = 650 mV.

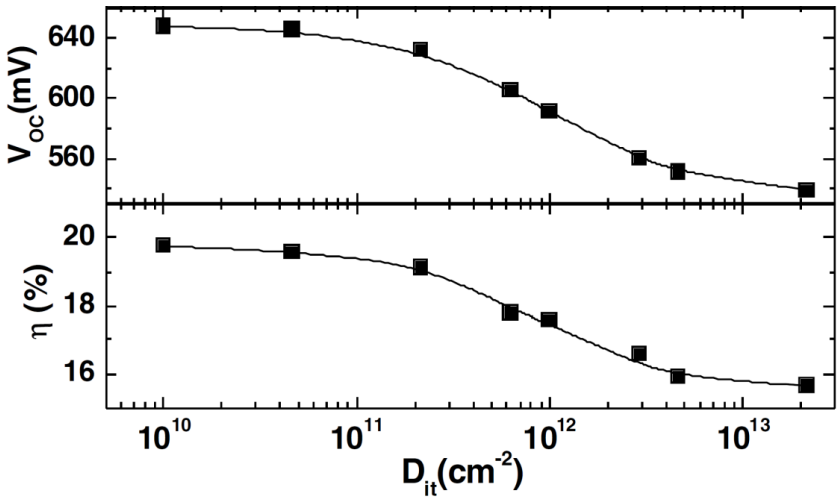

Fig. 14: Simulated dependency of the open circuit voltage V_{OC} and the efficiency η on the integrated interface state density Dit at the a-Si:H/c-Si interface [taken from [62]].

Heterojunctions have a much higher open circuit voltage potential. Consequently, the Panasonic record cell demonstrated a V_{OC} of 740 mV [60]. To achieve its full potential, the defect density of the surface must be kept low. Usually this can be achieved by an intrinsic interface passivation layer with a thickness of a few nanometers. The quality of this intrinsic interlayer is detrimental for the efficiency of a-Si:H/c-Si heterojunctions, as can be seen in Fig. 14. In this study, D_{it} is varied by three orders of magnitude. For $D_{it} < 5\times10^{10}\,cm^{-2}$ the V_{OC} remains almost constant. An increase in D_{it} to $2\times10^{12}cm^{-2}$ rapidly decreases V_{OC} to 560 mV. Moreover, the efficiency is reduced simultaneously from 19.8 % to 15.6 %. The results of this simulation can be easily tested by fabricating two devices, one with a high D_{it} and one with a low D_{it}. The high quality passivation was realized with a hydrogenated intrinsic amorphous silicon layer, which is known for its excellent interface passivation properties [63,64]. For the low quality passivation a simple natural oxide was used with D_{it} of 2×10^{12} $eV^{-1}cm^{-2}$ at midgap. The full distribution of the defect states regarding its energetic position in the band gap is shown in section 4.1. The consequence of the different interface passivation qualities is

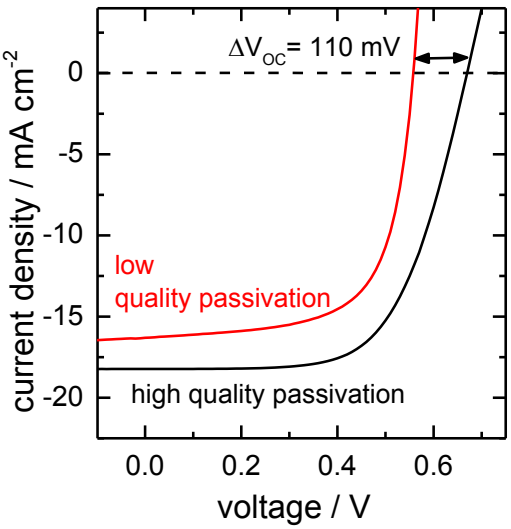

Fig. 15: j(V)-curves of spot test cells to determine the influence of passivation layers on the device performance in a-Si:H/c-Si heterojunction solar cells.

directly represented in the j(V)-curves displayed in Fig. 15. The V_{OC} values differ by 110 mV, reaching $V_{OC,a\text{-}Si}$ = 669 mV for the high quality passivation with an a-Si interlayer and $V_{OC,\ SiOx}$ = 558 mV for the low quality passivation by means of a tunneling SiO_X layer. These spot test cells nicely verify the results of the simulation with a higher V_{OC} for the low D_{it} than expected from the simulation. Additional a decrease in current and fill factor is observed, which can also be explained by the recombination at the interface [62,65]. The high diffusion lengths in crystalline silicon also make the devices sensitive on recombination on the back side. In this field free part of the wafer the band offsets prevent the charges from reaching the recombination active contacts (see also section 4.2). The a-Si:H/c-Si heterojunction is the successful combination of a low bandgap absorber and an amorphous wide band gap emitter and therefore very close to the device design of the hybrid heterostructure solar cells investigated in this thesis and may be of help to understand the physics behind the devices fabricated from the combination of organic and inorganic materials.

3. Experimental methods

In the present chapter measurement methods used in the thesis will be briefly explained. The focus is put on the measurement methods used for the material characterization or which require a certain knowledge regarding the analysis techniques. Among those are surface photovoltage spectroscopy, x-ray diffraction spectroscopy, photoelectron spectroscopy, charge carrier lifetime measurements, and Fourier-transform infrared spectroscopy.

3.1 Surface photovoltage measurements

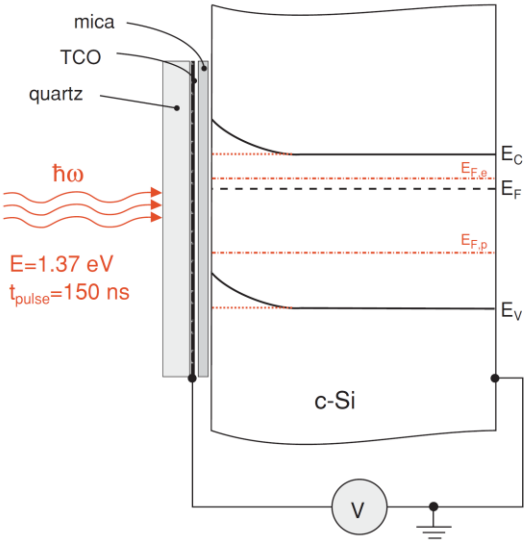

Fig. 16: Schematic sketch of the surface photovoltage measurement setup including a band scheme of c-Si. A MIS structure is formed between a TCO on a glass plate, the insulating mica plate and the c-Si sample (taken from [68]).

Surface photovoltage (SPV) is a well-established electrical characterization method for the determination of the density of surface states (D_{it}) [66] or the equilibrium band bending in silicon [67]. Surface photovoltage measurements utilize the change of the electrochemical potential in the space charge region of a semiconductor due to illumination with light of suitable wavelength and intensity. A metal-insulator-semiconductor (MIS) structure is formed between the transparent conductive oxide (TCO) layer on a glass plate, an insulating mica plate and the c-Si sample (see Fig. 16) [68]. The ohmic back contact is realized through a gold-coated chuck. The sample is excited by laser pulses ($t = 150$ ns, $\lambda = 900$ nm, $P_{Laser} = 210$ W) through the TCO layer. The absorption of the laser light in the semiconductor (here Si) gives rise to the change of the surface potential due to a redistribution of photogenerated charges, which is measured as a change in the capacitance of the MIS structure. Ideally, the laser intensity is high enough to create as many excess charge carriers to reach flat-band condition in the semiconductor and is in a steady state after the laser pulse is turned off. In that case, the maximum value of the SPV signal at the time $t = 0$ (immediately following the laser pulse) gives the band bending in the dark that has to be corrected by the Dember voltage [69,70]. The investigation of the energetic distribution of interface states

(D_{it}) is possible by applying an external bias voltage to the sample to change the energetic position of the Fermi-level [66].

3.2 X-ray diffraction spectroscopy

X-ray diffraction spectroscopy (XRD) allows defining the material composition and the structural quality, including the orientation of the crystallographic direction. An x-ray beam incident to the sample includes an angle of Θ to the lattice plane (see Fig. 17). This beam is deflected at the lattice planes and interferes with x-ray beams deflected from the neighboring lattice plane with the distance d. The angle for constructive interference of the incident x-rays to occur is determined by Bragg´s law [71]

$$2d \cdot sin(\Theta) = n \cdot \lambda \quad . \tag{19}$$

The prerequisite for constructive interference is a integer multiple n of the x-ray´s wavelength λ. Similar to the ideal grating, Bragg-peaks become sharper and higher order peaks evolve with an increasing number of lattice planes N. Additionally, The width of the first order peak is proportional to N^{-1}. From the width of the first order peak the crystallite height B can be estimated using Scherrer´s equation [72,73]:

$$B = -\frac{0.9 \cdot \lambda}{\cos(\Theta) \cdot \sqrt{(\Delta\Theta)^2 - b^2}} \quad . \tag{20}$$

ΔΘ is the half width of the Bragg peak and b the peak broadening due to instrumental contributions. Here, a value of 0.07° is assumed limiting the validity of the Scherrer´s equation to crystallite heights of ~150 nm. Another limitation is that the equation is only valid for thin films with a finite number of lattice planes and may not be used for thick crystals.

The samples were measured in a Bragg-Brentano-geometry with a SEIFERT theta-theta-diffractometer MZ VI using Cu-K_α = 0.154056 nm radiation and a secondary monochromator to filter undesired reflections.

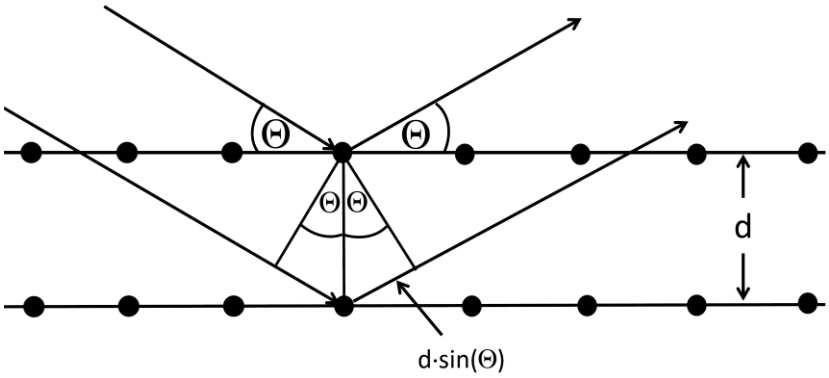

Fig. 17: Deflection of irradiated x-ray beams including the angle Θ and the optical retardation d×sin(Θ) to describe Bragg`s law.

3.3 Photoelectron spectroscopy

Photoemission is based on the photoelectrical effect, which was first observed by Hertz [74] and explained by Einstein [75]. Classically, it is described as a three step process [76]:

- Photo excitation of electrons
- Their transport to the surface and
- The escape over their work function barrier (surface) into vacuum

Ideally, electrons are not subjected to inelastic scattering until their escape into vacuum. These electrons carry the desired information about their initial state within the distribution of their kinetic energies. Monochromatic radiation is used for the excitation to define the amount of energy transferred to the electrons. Usually energy-selective detection is employed. The reference energy is the detector vacuum level E_{Vac} relative to which the kinetic energy E_{kin} of photoelectrons is detected. Sample and detector are electrically connected and therefore the Fermi energies are aligned (not the vacuum levels). The binding energy E_{bind} is measured relative to the Fermi energy. photoelectron spectroscopy is frequently used to determine the energy level alignment of molecules/polymers

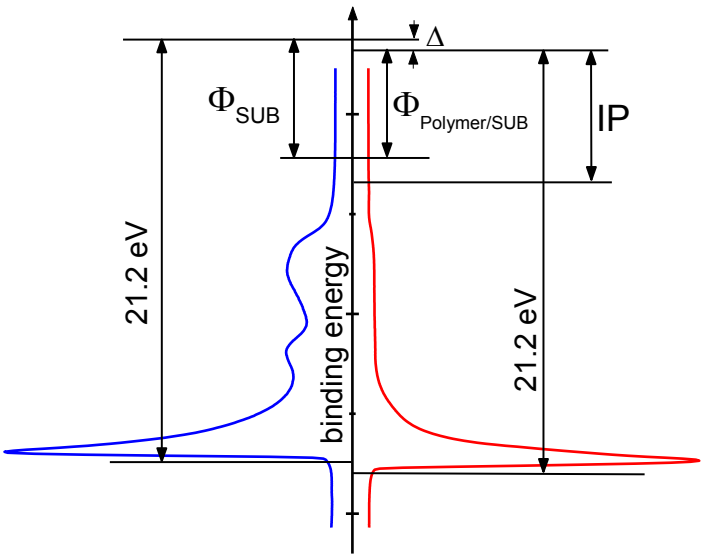

Fig. 18: Illustration of important parameters determined by UPS.

or inorganic compounds on surfaces. The important parameters probed are explained in Fig. 18 and are the following: The work function of the bare substrate Φ_{SUB}, the work function of the polymer coated substrate $\Phi_{Polymer/SUB}$. Both are determined by the energy of secondary electron cutoff (21.2 eV) and ionization potential of the sample (IP). Δ indicates shifts in the vacuum levels due to interface dipols.

Different variations of photoelectron spectroscopy are commonly used, often termed by the energy of the monochromatic light. X-ray photoelectron spectroscopy (XPS) or ultraviolet photoelectron spectroscopy (UPS) are the most common. The use of different excitation energies has further consequences. The mean free path λ_{mfp} of excited electrons in silicon has a broad minimum at the kinetic energy of $E_{kin} = 10…100$ eV due to electron-phonon and electron-electron interactions [77,78] (see Fig. 19). To probe more than the mere surface of the sample, the universal curve suggests that either high kinetic energies (as done for XPS) of the photoelectrons or very low energies which barely suffice to overcome the work function barrier would be desirable. In this work, the light sources used were the He I radiation ($h\nu = 21.22$ eV) of a helium discharge lamp and Mg Kα radiation

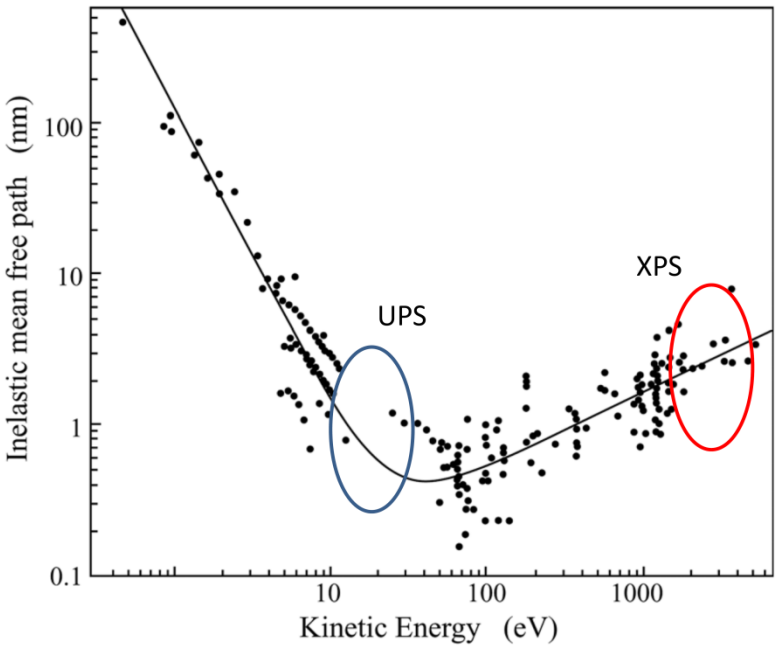

Fig. 19: Universal curve of the mean free path of electrons in solids dependent on their kinetic energy [taken from [79]]. Energy regions in which the XPS and UPS measurements in this work where done are highlighted.

($h\nu$ = 1253.6 eV) of a non-monochromatized X-ray source leading to a mean free path of $\lambda_{mfp} \leq 4\ldots8$ nm for both measurement methods.

3.4 Charge carrier lifetime measurements

The critical loss mechanism of recombination in solar cells can be probed by measuring the charge carrier lifetime. Therefore, a commercially available Sinton lifetime tester is used, which is well established in the silicon community. The measuring principle is based on the contactless measurement of photo-generated charge carriers in the Si wafer. The charge carriers are generated by a xenon flash lamp and are exposed to a periodically varied magnetic field. The induced current is proportional to the sample thickness W and conductivity σ. The induced current attenuates the amplitude of an oscillator circuit creating the measurement signal proportional to the product of W and σ.

3.5 Fourier-transform infrared spectroscopy

Infrared spectroscopy (IR) is a widely used non-destructive technique for the determination of molecular structure and for the identification of compounds. IR spectroscopy needs a change in the molecular dipole moment during the vibration [80] to be observable. Additionally, the vibrational excitation is achieved by radiating the sample with a broad-band source in the infrared region in the range from 4000 - 200 cm^{-1} (2.5 – 50 µm) wavelength. The molecules are excited to higher vibrational states by direct absorption of the infrared radiation. Experimentally the broad band IR radiation is sent through a Michelson interferometer (see Fig. 20). The resulting interferogram made by the moving mirror is shone through the sample and energy is absorbed by the molecules. Fourier transformation of the recorded spectrum results in the IR spectrum usually presented in wave numbers (cm^{-1}).

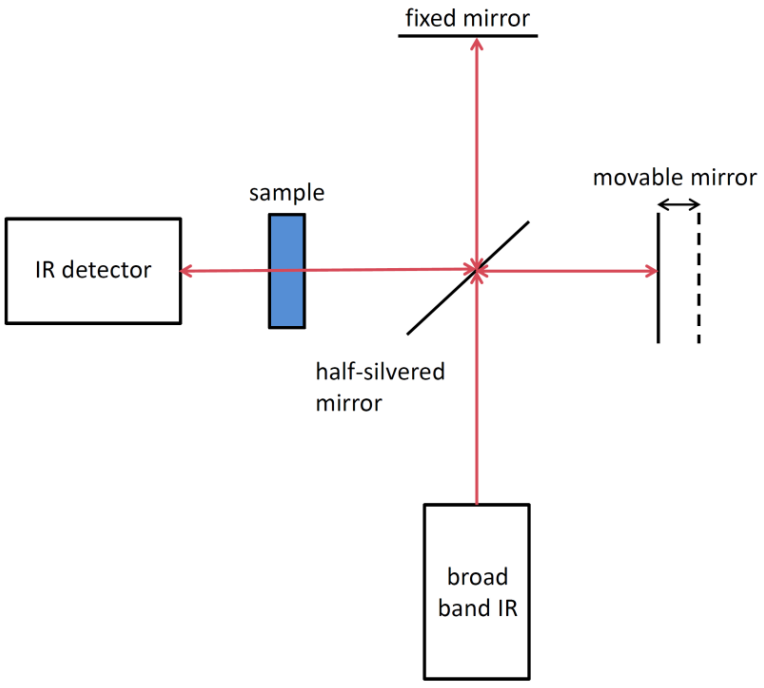

Fig. 20: Sketch of an experimental setup for Fourier-transform infrared spectroscopy measurement based on a Michelson interferometer.

4. Sample preparation and device geometry

The present chapter will focus on the preparation of the functional layers in the hybrid solar cells and starts with the cleaning and surface conditioning of the silicon substrates. The deposition of the back surface field via a PECVD process follows. This process was chosen for the back side preparation due to the high process stability and reproducibility, which makes it easier to recognize variations in solar cell efficiency caused by changes in the organic emitter layer only. Spin coating of polymers is briefly introduced and the influence of the substrate on the spin coating process is demonstrated. The device structure presented at the end of this chapter describes the first hybrid silicon/organic solar cells at the institute for silicon photovoltaics and is the groundwork for the following investigations and device optimization.

4.1 c-Si cleaning and surface conditioning

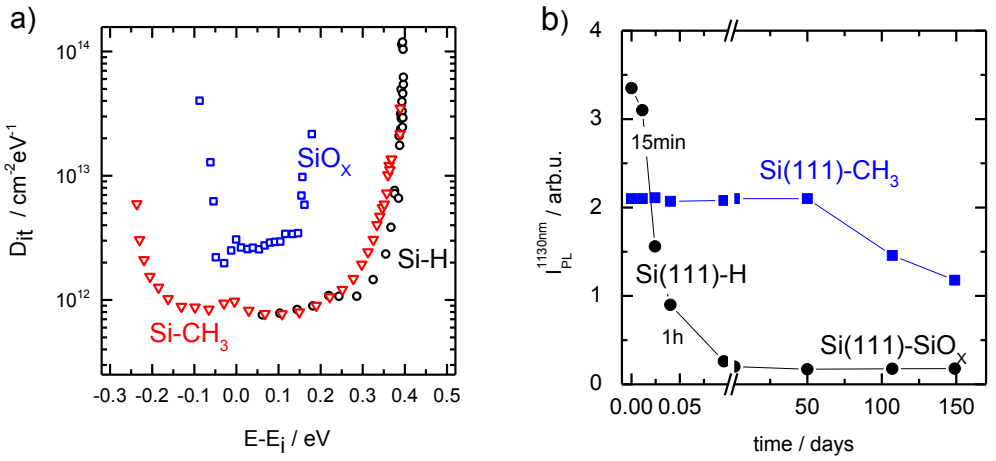

Fig. 21: a) Interface state density D_{it} for different surface treatments determined by SPV, **b)** PL intensity recorded at 1130 nm of H- and CH_3-terminated Si(111) surfaces as a function of time in ambient air.

The 280 µm thick crystalline silicon (c-Si) wafers with a resistivity of 1 – 10 Ω cm used as the inorganic absorber of the devices have been cleaned according to the process of the Radio Company of America (RCA clean) [81]. The phosphorus doped n-type float-zone wafer had ⟨100⟩-orientation with polished surfaces.

The front side passivation of the Si was either achieved through a natural oxide or a CH_3-termination [3]. Both surface conditionings required a hydrogen termination (H-termination) of the surface beforehand, which was achieved by a 90 s dip in diluted hydrofluoric acid (HF) with a concentration of 5 %.

For the natural oxide, the H-terminated Si wafer remained in the clean room atmosphere for > 10 hours. The resulting oxide had a thickness of 1.5 – 1.7 nm as determined by spectral ellipsometry (SE).

A one-step, electrochemical grafting process using methyl-Grignard passivated the silicon surface with covalently bonded methyl groups. The electrochemical modification of the Si surface was performed in a nitrogen

purged glove box using galvanostatic mode, where the H-terminated Si served as the working electrode (anode) and a Pt sheet as counter electrode (cathode). The methyl-Grignard (CH_3-MgBr) dissolved in diehtylether with a concentration of 3 mol/L was used as electrolyte. The reaction was started by sourcing a current of 0.5 mA through Si into the CH_3-MgBr solution. Afterwards, the sample was rinsed with the pure solvent and high purity water. Fig. 21a) presents the density of interface defects, D_{it}, for these three different interface terminations commonly used in hybrid solar cells (HSCs) as measured by surface photovoltage techniques (SPV) [67,82]. The low defect density of the H-termination (open circle) achieved by an HF-Dip was maintained by electrochemical grafting of CH_3-groups (open triangle) using the Grignard reagent. The D_{it} of a passivating thin tunneling oxide (open rectangle) is about a factor of 4 higher. The long time stability of the CH_3-termination of Si(111) is shown in Fig. 21 b) in comparison to a H-terminated Si(111) surface measured by photoluminescence spectroscopy (PL) as function of time in ambient air. The CH_3-termination shows no change in the surface recombination velocity and is stable for more than 50 days until it starts to decay at longer times in ambient air. The PL intensity of the H-terminated Si(111) surface is slightly higher in the beginning but the photoluminescence (PL) of the H-terminated Si(111) surface decays within 2 hours under the same environmental condition and turns into a SiO_X-passivated state of the Si surface. The resulting SiO_X/c-Si interface had more than a factor of 10 higher defect concentration compared to the CH_3-terminated Si surface.

4.2 a-Si deposition and back surface field

To avoid recombination of the photogenerated charge carriers and provide good selective collection of these charge carriers, an electron selective back contact (see Fig. 23) was used for the c-Si based HSCs [83]. With n-type silicon, this is usually achieved by the formation of an n/n^+-junction using highly phosphorus doped amorphous silicon, a so-called back surface field (BSF). This has been achieved by deposition of a 5 nm thick intrinsic a-Si:H passivation layer prior to the 25 nm (n^+)a-Si:H layer to suppress charge carrier

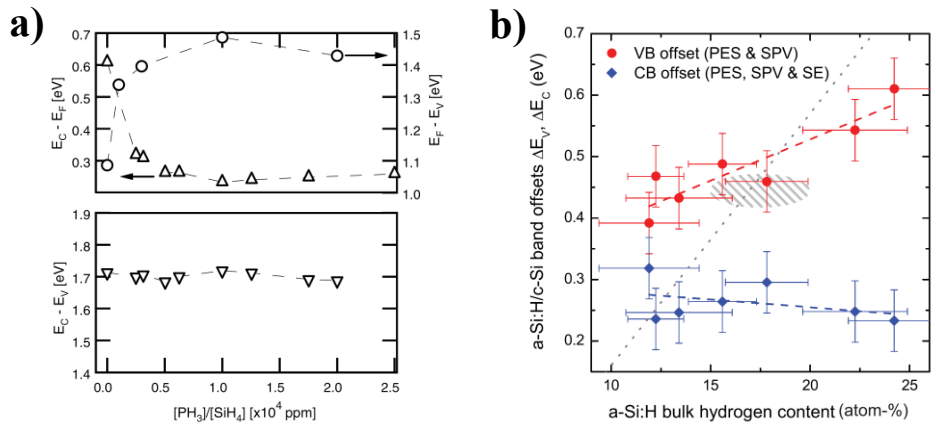

Fig. 22: a) Dependence of $E_F - E_V$, of $E_F - E_C$ and the calculated mobility gap of $E_C - E_V$ on gas phase doping (taken from[84]). **b)** Valence band offsets of (i)a-Si:H/(n)c-Si heterostructrues determined from a combination of PES and SPV measurements. Calculated conduction band offsets taking into account the band gap as determined by spectral ellipsometry (SE) (taken from [68]).

recombination on dangling bonds at the a-Si:H/c-Si interface. The samples were prepared on n-type c-Si(100) substrates with 1-10 Ω cm. After a RCA cleaning process followed an etching step in 1 % HF for 1 min before transferring the samples into vacuum. The hydrogenated amorphous silicon (a-Si:H) layers were deposited via **V**ery **H**igh **F**requency **P**lasma-**E**nhanced **C**hemical **V**apor **D**eposition (VHF-PECVD) (60MHz) at a base pressure of 10^{-7} mbar using semiconductor grade silane (SiH_4). Phosphine (PH_3) diluted to 1 % in hydrogen at a concentration of 2000 ppm was used for doping, resulting in a distance of $E_C - E_F = 0.3$ eV at a bandgap of 1.7 eV, independent of the doping concentration (see Fig. 22) [84]. The position of the Fermi - level in the band gap of c-Si is well known from its doping concentration. The doping concentration of 10^{15} cm^{-3} results in an energetic distance of $E_C - E_f = 0.4$ eV (see also Fig. 23). The band bending in the c-Si amounts to 0.13 eV and the conduction band offset to $\Delta E_C = 0.07$ eV. Due to the large density of rechargeable states that have been found in the band tails of a-Si:H and the dangling bond defects in the band gap, the electric field stemming from the immobile dopant ions in the c-Si is shielded close to the surface and therefore

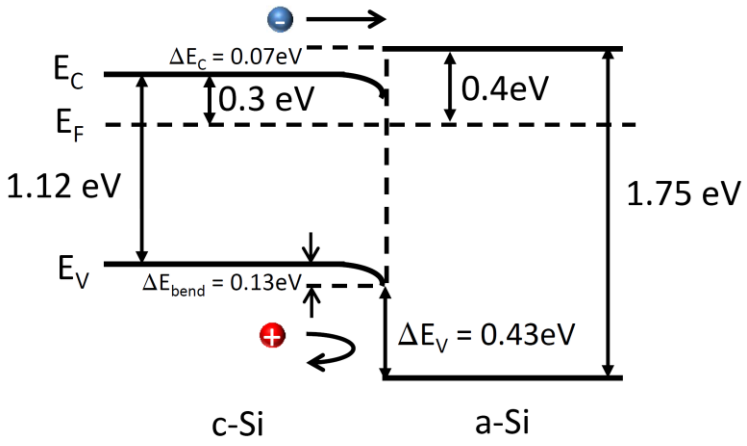

Fig. 23: Energy level alignment of the n/n$^+$ - back surface field used in the HSCs. Photogenerated holes are reflected at the valence band offset ΔE_V = 0.43 eV and still can be collected at the hole contact. Electron transport is not affected by the small conduction band offset ΔE_C = 0.07 eV.

only supports a negligible fraction of the overall band bending. The 5nm thick intrinsic layer is neglected for the energy level alignment as it only shields a small amount of the electric field, but reduces the density of states (DOS) in the band gap. The valence band offset varies with the hydrogen content of the a-Si:H layer, but is close to ΔE_V = 0.43 eV in the used range (probably slightly higher; see Fig. 22).

For the a-Si:H/c-Si reference cells p-type a-Si:H was deposited as an emitter layer, again, using the earlier mentioned VHF-PECVD process. P-type doping was achieved by substituting phosphine with diborane (B_2H_6). The doping concentration of diborane in the PECVD chamber was 2000 ppm and the deposited (p)a-Si:H emitter layers had a thickness of about 10 nm. One of the most desired properties of organic semiconducting polymer materials for the use in opto-electronic devices is the possibility of solution processing. These used polymers, i.e. P3HT, can be dissolved in various organic solvents at high concentrations. Production of thin organic films can be performed by a variety of techniques: dip coating, meniscus coating, extrusion coating, doctor blading, inkjet printing and spin coating. The latter is probably the most widely used as it is a simple method which can lead to very uniform films

4.3 Spin coating of polymer materials

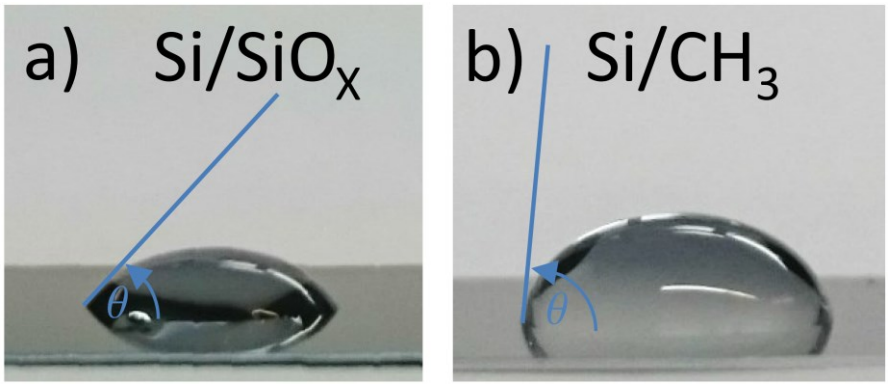

Fig. 24: Photograph of a drop of water on silicon with different surface modifications. **a)** Hydrophilic Si/SiO_X interface with a contact angel of 47° and **b)** hydrophobic CH_3-terminated surface with a contact angle of 84°.

with well-controlled thickness [85]. A large amount of solution is applied to the sample mounted on a rotating disk. The liquid layer thins as the solution flows radially outward during rotation. Additional evaporation of the solvent during rotation increases the viscosity and finally leads to the formation of a thin solid film with a thickness in the range of several nanometers up to micrometers [86].

4.3.1 Influence of the substrate

Polymer films were deposited from a solution of 1,2-Dichlorobenzene (DCB) in a nitrogen-filled glovebox as soon as available. If not, it will be indicated in the respective chapter. The film thickness was varied by adjusting the polymer concentration. The parameters spinning speed and duration were adjusted depending on the surface modification of the substrate (see section 4.1). While Si/SiO_2-interface has hydrophilic properties, the Si/CH_3-interface has the same hydrophobic properties as the H-terminated Si due to its non-polar nature [87]. Fig. 24 displays the different wetting properties of the two surface modifications by the different contact angles θ. The good wetting behavior of the SiO_X is represented with a small contact angle of 47 °. The non-wetting

CH_3-terminated surface has a contact angle of 85 °. The de-wetting of water on the CH_3 - modified surface shows its non-polar nature, much the same as in bare silicon or many self-assembled monolayers [87,88]. Consequently, different preparation methods for the spin-coated thin films were necessary, depending on the wetting behavior of the substrate. While on the natural oxide low polymer concentrations of 1 mg/ml already led to good cell results, polymer concentrations of 3 mg/ml were necessary on the methylated surfaces. Furthermore were the spin coating parameters adjusted. On the oxide surface polymer concentrations of 1 – 5 mg/ml were spin coated with 2000 rounds per minute (rpm) for 30 seconds. The resulting layers were 10 nm to 45 nm thick. On the methylated surfaces concentrations 3 – 5 mg/ml were spin coated with 2200 rpm for 45 seconds. The film thicknesses were in the range of 20 nm to 35 nm. The films were annealed on a conventional temperature-controlled hot plate at 70 °C for 20 min to remove residual solvent.

4.4 Metal deposition

The contact systems of the solar cells were deposited by thermal evaporation under high vacuum conditions. For the back contact aluminum with a thickness of 1.5 µm was used. Before deposition of the metal on the BSF the silicon oxide of the back side was removed by a HF drop with diluted HF at a concentration of 5 %. Afterwards the substrates were transferred into the glove box system for spin coating of the polymer layer. As front contact a 12 nm thick Au layer was deposited through a shadow mask, which defined the active area of the devices. During this thesis the cell size was increased from 0.13 cm^2 to 1 cm^2. The molybdenum oxide (MoO_X) buffer layer introduced in section 5.3, which is known to improve device efficiencies in organic photovoltaics [89,90,91] was applied during the same vacuum process step. Thermal evaporation of the 5 nm thick buffer layer was done immediately before the gold evaporation. The thicknesses of all layers deposited by thermal evaporation were monitored using a quartz crystal microbalance (QCM).

4.5 Basic device structure and first cell results

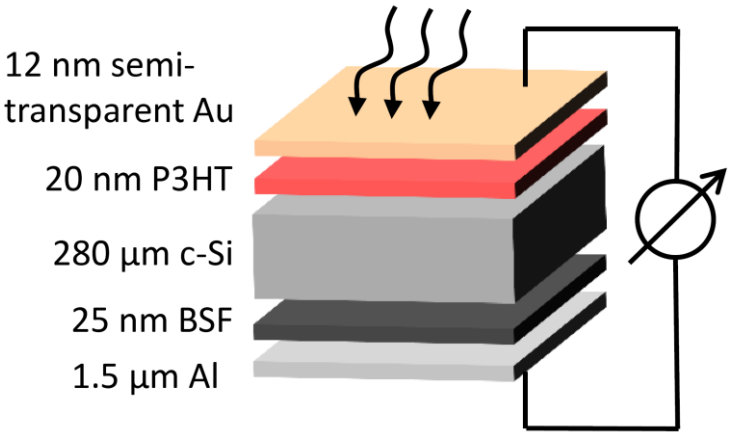

Fig. 25: Device design used for hybrid inorganic/organic heterostructure solar cells. For further developments during the thesis this cell design was used as a basis.

Fig. 25 depicts the device design of a typical hybrid inorganic/organic heterostructure at the institute for silicon photovoltaics with a solution processed emitter layer on an n-type crystalline silicon wafer. Similar device structures with a thermal evaporated semitransparent gold (Au) contact have been used in literature for investigations [14,92] mainly due to the high work function of the gold and to improve lateral conductivity. P3HT was chosen for the organic component of the solar cells. The position of the energy levels of P3HT (E_{HOMO} = - 4.60 eV; E_{LUMO} = - 2.70 eV) fit well to those of the n-type crystalline silicon (E_C = - 4.05 eV; E_V = - 5.17 eV) without impairing the charge transfer from the silicon to the polymer; an important requisite for high efficiency solar cells. For the first solar cell results the front side of the wafer was passivated with a natural oxide (see section 4.1). The electron-selective back surface field (see section 4.2) was fully covered with aluminum for good ohmic contact. Fig. 26 shows the j(V) - curve under illumination for a typical device with the just described cell structure and a cell size of 0.13 cm^2. The

device exhibits a reasonable efficiency of η = 3.2 % with a good fill factor of FF = 70.5 %. It is obvious that short circuit current as well as open circuit voltage offer major room for improvement. While the reason for the low current is easily identified by the optical properties of the solar cell, e.g. light absorption in the semitransparent metal contact, the low open circuit voltage needs a deeper understanding of the underlying device physics. Many different factors come into play, whose influences are not clear for this rather new device type. To name a few, the passivation of the dangling bond surface states of the crystalline silicon [93], the band alignment at the silicon/polymer interface [94, 95] or the band bending in the crystalline silicon [15]. The following parts of the thesis will focus on answering fundamental physical questions towards efficiency limiting factors. Optimizations to the cell design will be presented, including the implementation of Graphene as a low-cost, transparent and conductive electrode.

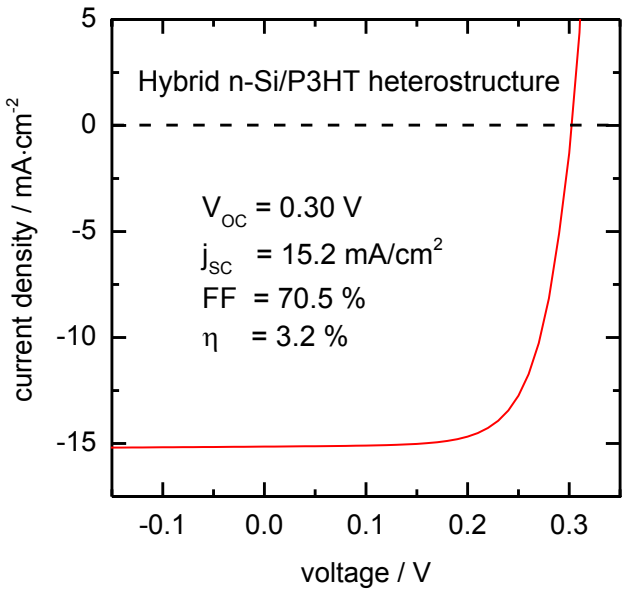

Fig. 26: j(V)-characteristics of a hybrid inorganic/organic heterojunction solar cell under illumination.

5. Side chain engineering of poly-thiophene and its impact on hybrid solar cells

The possibility of custom-tailoring a physical property, specially fitted to a specific problem is among the biggest advantages of organic materials. Often the band gap [96], the energy levels [97] or the microstructure [98] are systematically tuned. For the latter several possibilities exist to tweak the structure of a material. For P3HT, thin-film processing conditions [42], molecular weight [48] as well as regioregularity [99] have been identified as possible adjustment parameters. The scope of this chapter is to present a further method to influence the crystallinity of solution processed polymers. Using the abundantly investigated polymer P3HT as a reference the influence of oxygen atoms in the side chains is investigated. First, the materials will be introduced and is followed by a structural characterization using AFM, XRD and UV/Vis. Finally, hybrid solar cells are prepared form these materials and the findings of the structural characterization are used to interpret the device performances.

5.1 Materials and synthesis

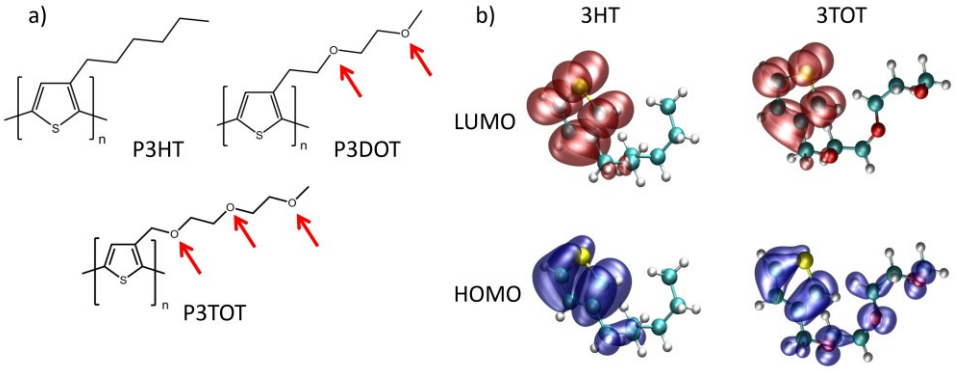

Fig. 27: a) Chemical structures of poly(3-hexylthiophene-2,5-diyl) (P3HT), poly(3-[3,6-dioxaheptyl]-thiophene) (P3DOT) and poly(3-[2,5,8-trioxanonyl]-thiophene) (P3TOT). Red arrows depict the oxygen atoms in the hydrophilic side chains. **b)** Electron density of HOMO and LUMO for the monomers 3HT and 3TOT calculated by density functional theory (DFT) [100].

Poly-thiophenes are an important class of semiconducting polymers and belong to the most thoroughly investigated π-conjugated materials. Unsubstituted poly-thiophenes are insoluble and cannot be processed form solution. To improve the solubility of poly-thiophenes alkyl chains are added to the thiophene ring. The most prototypical representative is probably poly(3-hexylthiophene-2,5-diyl). Its chemical structure is depicted in Fig. 27 a). But these side chains do not only promote solubility. Paloheimo et al. [101] found a decrease in mobility with an increase in alkyl chain length from butyl to decyl due to the insulating nature of the alkyl chains. P3HT exhibited the highest mobility of $\mu \sim 0.1$ cm^2/Vs. The degree of regioregularity also has a strong influence on the morphology. Depending on the synthesis route, three different conformations are possible to link the thiophene momomers: head-to-head (HH), head-to-tail (HT) and tail-to-tail (TT) (see Fig. 28 a)). Polymers only containing HT - couplings are called regioregular, (rr) all other conformations are called regiorandom (rra). The materials used in this chapter are all regioregular to promote a high degree of crystallinity [99]. P3HT was purchased from Ossila with a regioregularity of 98.5 %. The two other

polymers were synthesized at the Fraunhofer IAP in the group of PD Dr. S. Janietz. The chemical structures of these two materials are also shown in Fig. 27 a). The side chains of P3HT are substituted with 2 and 3 oxygen atoms containing side chains, respectively. Poly(3-[3,6-dioxaheptyl]-thiophene) (P3DOT) and poly(3-[2,5,8-trioxanonyl]-thiophene) (P3TOT) are expected to improve the wettability and therefore the thin-film formation on the oxidized Si surface due to the hydrophilic nature of the side chains; an important quality for spin coating of the polymer layers. However, it has to be ensured that the physical properties connected to the π-conjugated backbone of the polythiophene remain unimpaired. Fig. 27 b) depicts the electron density of the highest occupied molecular orbital (HOMO) and the lowest unoccupied molecular orbital (LUMO) for the monomers 3HT and, exemplarily, 3TOT. The higher electron density of the HOMO on the side chain of the 3TOT is located on the oxygen atoms and does not significantly alter the electron density in the ring. For both repeating units the LUMO is entirely localized on the ring, indicating that the side chains do not affect optical transitions or transport properties. The polymerization of P3DOT and P3TOT was carried out following the Grignard Metathesis Method (GRIM) as described by McCullough [102] and provides a high degree of regioregularity. The synthesis route is shown in Fig. 28 b). The synthesis results regarding molecular weights and polydispersity index values are summarized

Tab. 4: Molecular properties of the materials P3HT, P3DOT and P3TOT.

material	number average molecular weight (M_n)	weight average molecular weight (M_W)	polydispersity index (PDI)	monomer units/chain
P3HT	36250 g mol^{-1}	145000 g mol^{-1}	4.1	240
P3DOT	14700 g mol^{-1}	24100 g mol^{-1}	1.6	80
P3TOT	22400 g mol^{-1}	35100 g mol^{-1}	1.6	107

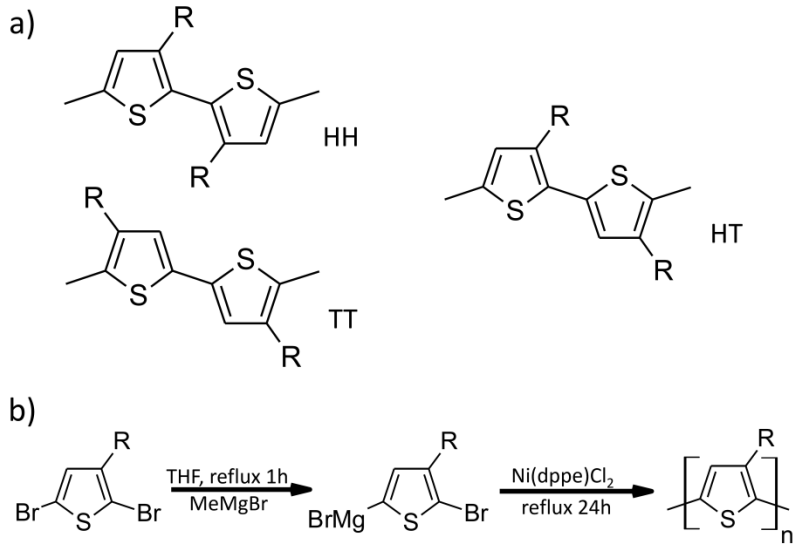

Fig. 28: a) Linking schemes head-to-head (HH), tail-to-tail (TT) and head-to-tail (HT) for poly(3-alkylthiophene). **b)** General **s**ynthesis route of poly(3-alkylthiophene).

in Tab. 4. All materials have a high number average molecular weight of $M_n > 14\,000$ g mol^{-1}. For easier comparability the monomer repeating units per chain are stated in the last column of Tab. 4. The high chain length of the commercial material P3HT stands out. However, according to a study by *Kline et al*.[103], which focused on changes in crystallinity and mobility connected to variations of the molecular weight showed that already ~ 100 repeating units of the 3HT monomer are enough for the highest performing polymers. No further improvements are expected using a higher molecular weight.

The synthesis grants high molecular weight, high regioregularity polymers comparable to the commercial product P3HT. DFT calculations imply that the change in electron density in the side chains does not impact the π-system of a single thiophene unit or the polymer chain. Changes in physical properties are only caused by a change in the layer formation due to a modified interaction with the substrate or the polymer strands among each other. Consequently, further characterizations can be interpreted directly using the commercially available and well-studied polymer P3HT as a model system.

5.2 Structural investigation of spin-coated polythiophene layers

5.2.1 Atomic Force Microscopy

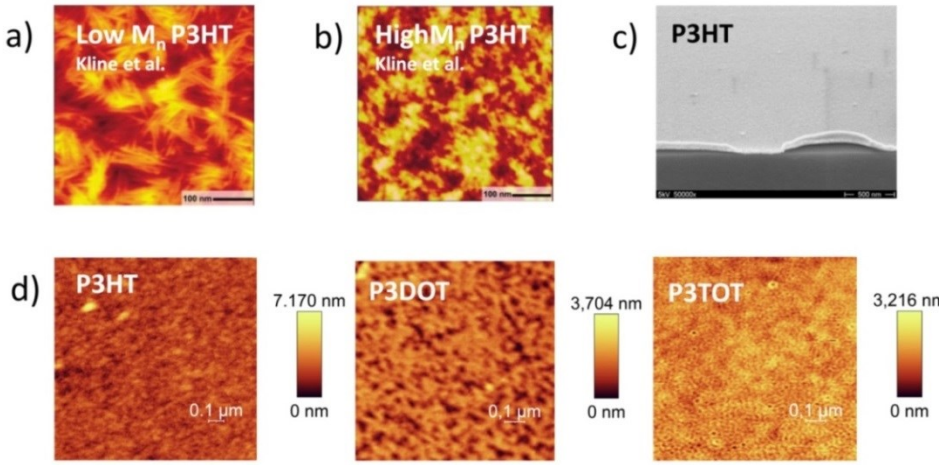

Fig. 29: Tapping mode atomic force microscope (AFM) images of **a)** a low and **b)** high molecular weight P3HT film [taken from [103]]. **c)** Cross section REM picture of a P3HT layer at an angle of 30°. **d)** Tapping mode AFM images of polymer films of P3HT, P3DOT and P3TOT.

Thin films of all three materials were prepared in according to section 4.3. Please note, that all sample preparation have been performed in ambient air if not stated otherwise. Atomic force microscope (AFM) images and an additional scanning electron microscopy (SEM) image of these films are presented in Fig. 29. Fig. 29 a) and b) are taken from *Kline et al.* [103]. The low M_n sample differs from the high M_n sample by the formation of clearly visible needle-like structures indicating a higher degree of crystallinity. Those are not visible for the materials used in this study or the high M_n sample from literature. SEM images show a homogenous film without any pinholes or crystalline domains, as well.

The results support the fact that all materials are high molecular weight despite the variations in chain length. Furthermore, the root-mean-square (rms) roughness is reduced with an increasing number of oxygen atoms in the side

chains. The values decline from 5.6 Å for P3HT to 4.2 Å for P3DOT to 3.1 Å for P3TOT and provide a first hint regarding the expected improved solution casting of the polymer films. However, the AFM data only provides an image of the top surface. The type of structure does not necessarily prevail throughout the film. Therefore the next chapters will present a more thorough structural investigation.

5.2.2 X-Ray Diffraction Spectroscopy

In Fig. 30 XRD spectra of annealed polymer films on Si/SiO_X substrates are shown. The data clearly indicate the existence of crystalline domains. For P3HT and P3DOT the (100) reflection is observed at $2\Theta \approx 5.1°$, which is due to a lamella structure [43,104]. It corresponds to a polymer chain spacing of 1.71 nm. The lamella structure is oriented parallel to the surface normal as depicted schematically in 2.2.4. A difference in the crystal structure related to the different length of the side chains for P3HT and P3DOT was not observed. The results obtained for P3HT and P3DOT are in

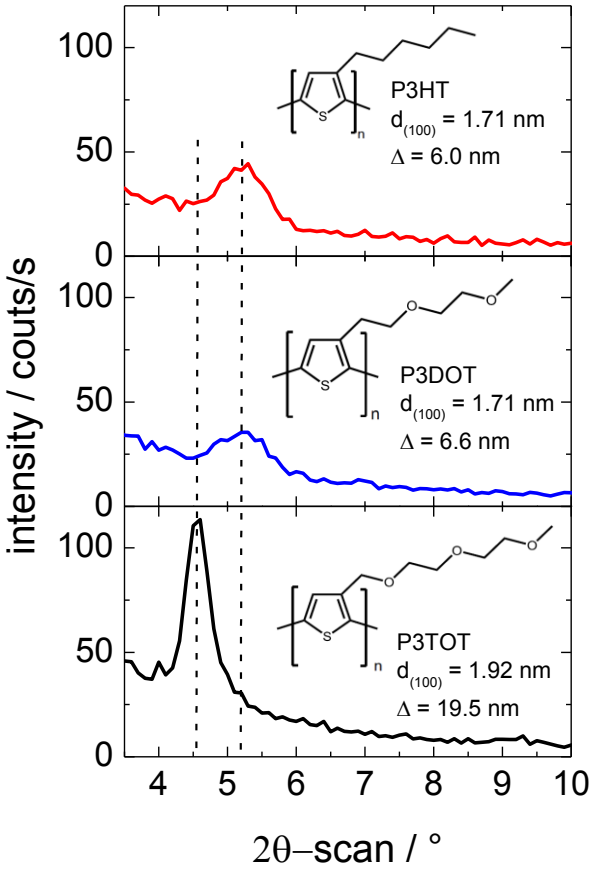

Fig. 30: XRD-data of polymer films prepared by spin-coating on Si substrates after annealing for 30 min at 70 °C. Measurement reveals a π-π-stacking of the polymer chains parallel to the substrate.

good agreement with literature [103] for high molecular weight regioregular P3HT. For P3TOT the lamella spacing is slightly increased to 1.92 nm, which is caused by the longer trioxanonyl side chains compared to the hexyl side chains [46,105]. The narrower (100) Bragg reflection of the P3TOT film points to a higher degree in crystallinity, compared to the other two polymers. According to the Scherrer formula [72] the average crystallite sizes of the polymers were determined to be 6 nm for P3HT and P3DOT and 19 nm for P3TOT, respectively.

5.2.3 Absorption spectroscopy

5.2.3.1 UV/VIS

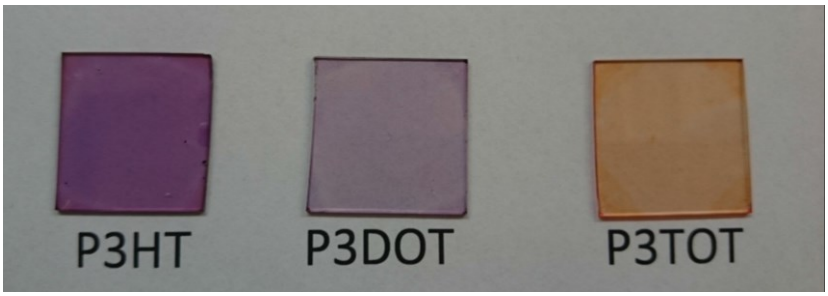

Fig. 31: Optical photographs of thin layers of the poly-thiophene derivatives prepared by spin-coating techniques.

Soluble polythiophenes have been studied to a great extent. A great effort was directed in the investigation of the influence of the molecular structure on the photophysics of conjugated polymers. The position of the maximum absorption wavelength [106] as well as the occurrence of a vibronic structure [55] in the solid state are connected to the degree of π-conjugation in the polymer chain and a result of the stabilization of a coplanar conformation of the polymer backbone. The stabilization of the coplanar state results from a van-der-Waals interaction of neighboring chains. As a consequence absorption measurements can make a sensitive tool for the investigation of structural properties in soluble polymers.

Solid layers of P3HT, P3DOT and P3TOT prepared by spin coating differ significantly in their optical appearance (see Fig. 31). The intense color of P3HT becomes lighter for P3DOT. This effect originates in the formation of a thinner layer during spin coating of P3DOT despite the same processing conditions (Conc.: 10 mg/ml in DCB, 2000 rpm, 30 s). For P3TOT the concentration of the polymer in solvent was increased by a factor of 3 for better perceptibility. The colors of the solid layers change from a dark red for P3HT and P3DOT to orange for P3TOT. The absorption spectra follow this

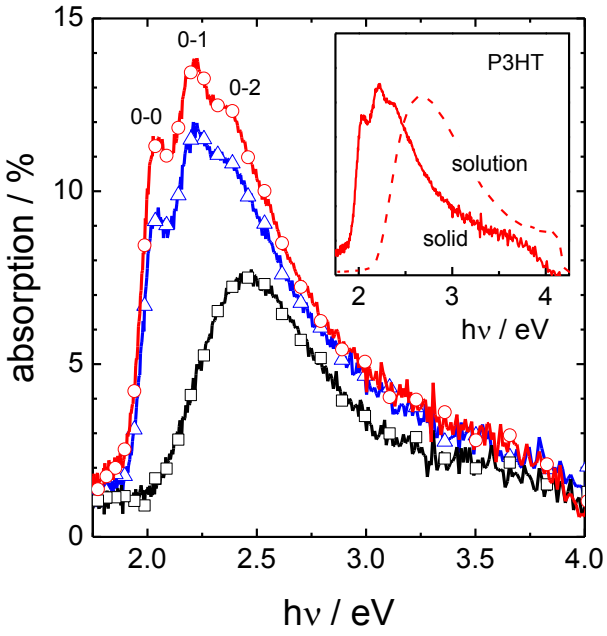

Fig. 32: Absorption spectra of the polymer thin-films on fused silica. The circles, triangles and squares represent P3HT, P3DOT, and P3TOT with a thickness of 20, 18, and 12 nm, respectively. The inset depicts the absorption spectra of P3HT in solution (dashed line) and after crystallization (solid line).

observation accordingly. Fig. 32 depicts the UV/VIS absorption spectra of the three polymers spin-coated on Si/SiO_X substrates. Prior to the measurement the samples were annealed at 70 °C for 30 min. The spectra of P3HT and P3DOT films exhibit a well resolved vibronic structure and a bathochromic shift of the peak maximum of 0.5 eV to lower energy (see inset of Fig. 32), as expected for poly(3-alkylthiophenes) [57]. The absorption spectrum of the P3TOT film shows no vibronic structure and a less pronounced bathochromic shift. Additionally, the shifted onset of absorption for P3TOT reflects the color change as observed in the photographs presented in Fig. 31. This change in the optical band gap is usually interpreted as a change in the effective conjugation length [106]. While the values for P3HT, P3DOT of $E_{Gap,P3HT} = E_{Gap,P3DOT} = 2.0$ eV represent the maximum conjugation length for P3HT, the effective conjugation for P3TOT reduces to $E_{Gap,P3TOT} = 1.9$ eV.

5.2.4 Interpretation of the structural characterization

While the absorption spectrum of P3TOT suggests little crystallinity, the XRD data reveal that the P3TOT film is crystalline with a higher structural order than the other polymer films (see Fig. 30). The clear discrepancies between the results of the UV/VIS and XRD measurements indicate that not only the structure of the resulting layer is changed by the variation of the side chains. The intrinsic properties of the molecules are dominantly determined by the π-electron system. The influence of the additional oxygen atoms in the side chains on the absorption is a difference within a single polymer strand. Thermochroism studies on poly(3-alkylthiophenes) identified the cause for the strong hypsochromic shift with increasing temperature to be an increasing twist between adjacent thiophene units [107]. A similar effect comes into play for P3TOT. For this type of molecule, a preferential ordering of the side chains within the plane of the main polymer backbone is expected. The resulting lamellar structure has a high degree of planarity along a single polymer chain,[108] resulting in the optical properties as can be observed for P3HT and P3DOT. However, P3TOT suffers from a steric hindrance of the side chains. The degree of planarity is lowered and results in a reduced degree of conjugation along the backbone. This has the following consequences. The red-shift that is commonly observed when the polymer is cast from a solution into a thin film is reduced for P3TOT and the vibronic structure vanishes (see Fig. 32) [57,107]. Vibrational properties of the polymers were investigated using FT-IR spectroscopy and are presented in the next paragraph.

5.2.5 Fourier-transform infrared spectroscopy

The symmetric stretching vibration of the thiophene ring is shown in Fig. 33 a). For P3HT the symmetric stretching vibration occurs at ≈ 1509 cm^{-1}. When O atoms are introduced into the side chains the vibrational mode shifts to 1511 and 1514 cm^{-1} for P3DOT and P3TOT, respectively. The increase in frequency by about 1 % indicates that the thiophene rings are subject to compressive strain. This is consistent with ab-initio density functional theory

calculations that show a decrease of the C – C bond length in the thiophene ring by about 1 % when 3 oxygen atoms are incorporated in the side chain [109]. Additionally, the presence of O atoms in the side chains gives rise to vibrational modes. Fig. 33 b) shows the spectral region where the C – O – C stretching vibrations occur. It is important to note that P3HT does not show vibrational modes in this spectral region, which clearly establishes that these local vibrational modes are due to the presence of O atoms in the side chains. In P3DOT and P3TOT two modes are observed at $\nu \approx 1108$ and 1135 cm^{-1} that correspond to asymmetric stretching vibrations of alkyl ethers [80]. With an increasing number of carbon atoms the IR band shifts to lower frequencies. However, a precise assignment of the frequencies to the position of the oxygen atoms in the side chain is challenging. Based on IR data of aliphatic ethers it is likely that the mode at $\nu \approx 1135$ cm^{-1} is related to the vibration of $–CH_2CH_2 – O – CH_3$ [80].

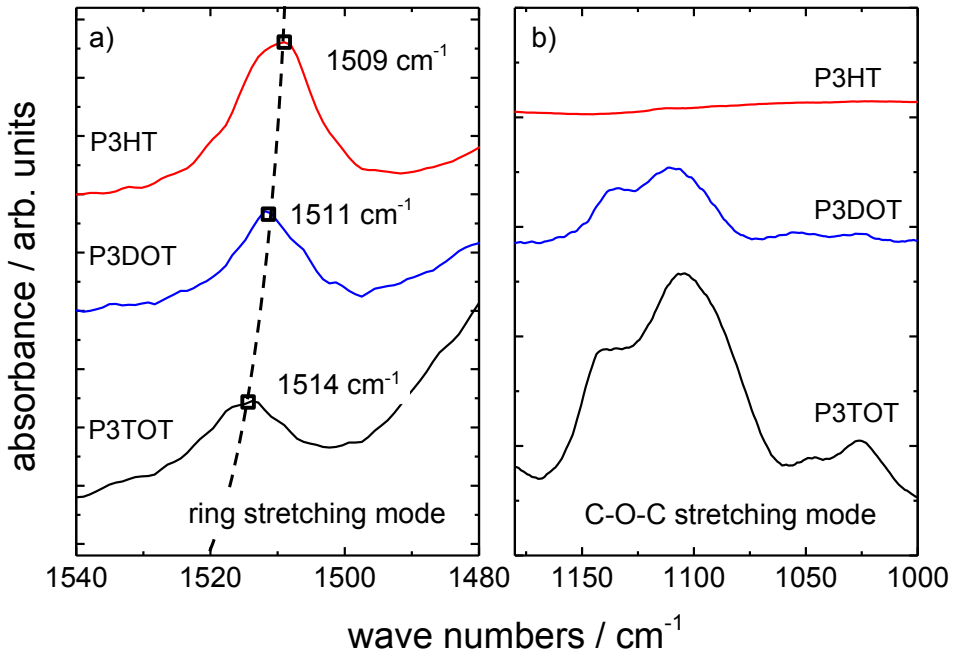

Fig. 33: FT-IR spectra of P3HT, P3DOT and P3TOT. The stretching mode of the thiophene rings is plotted in **a)** and **b)** shows the C – O – C stretching mode present in P3DOT and P3TOT.

5.2.6 Influence of side chain modifications on hybrid solar cell performance

The polymers P3HT, P3DOT and P3TOT were used to fabricate Si / polymer heterojunction solar cells according to chapter 4. In Fig. 34 the dark current voltage characteristics of hybrid solar cells with P3HT, P3DOT, and P3TOT are plotted. For comparison the j(V) curve of a metal-insulator-semiconductor (MIS) structure consisting of Au – SiO_X – c-Si is shown. The MIS and the P3HT based devices exhibit similar diode characteristics with saturation currents of about $j_0 = 1.6\times10^{-3}$ and 2.4×10^{-3} mA/cm^2, respectively. According to transmission electron microscopy data, the similarity is due to intermixing of Au and P3HT during the metal evaporation. On the other hand, when P3DOT and P3TOT are used to fabricate hybrid solar cells the saturation current-density decreases by about 2 orders of magnitude (see Fig. 34). For these devices intermixing of Au and the polymer layers was not observed. It is likely, that this is directly related to an improvement of the structural quality of the polymers due to the presence of the O atoms in the side chains (see Fig. 30). This clearly shows that side chain engineering can be used to improve device performance without the need for additional layers (i.e. diffusion barrier).

The hybrid solar cells were further characterized by measuring their j(V) curves under AM 1.5G illumination. The device characteristics are presented in Fig. 35. The performance of the MIS device is in good agreement with results from literature, approaching the theoretical limit for an Au/n-type Si diode with typical open circuit voltages below 0.3 V [110,111]. This value is mainly caused by the thermionic emission current flow of the electrons from the metal to semiconductor, limiting the open circuit voltage of Schottky devices compared to p–n junctions. A possibility to overcome this problem is the introduction of an interlayer, which further reduces the current flow across the barrier [112]. A basic precondition for the organic layers to perform this task is to prevent the direct contact of the metal to the semiconductor.

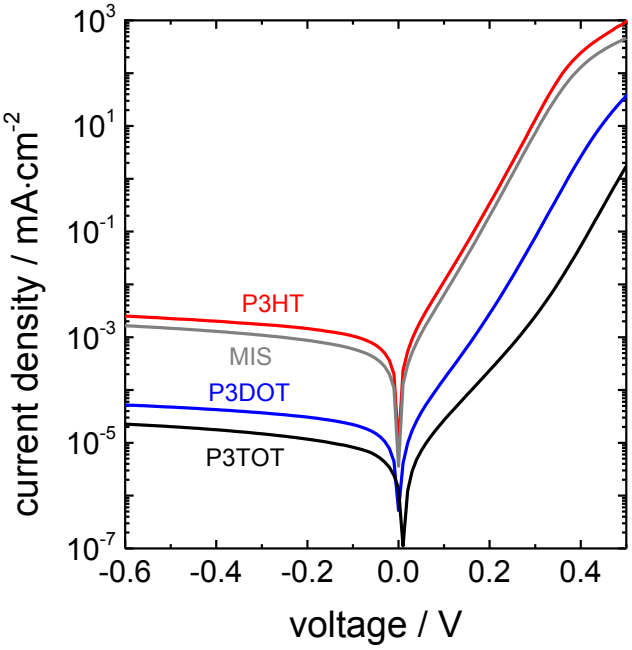

Fig. 34: Dark current-density as a function of the applied voltage, U, for hybrid heterojunction solar cells using P3HT, P3DOT, and P3TOT. For comparison the device characteristic of a MIS structure (Au – SiO_X – c-Si) is shown.

However, the similarity of the MIS device to the hybrid solar cell with a P3HT interlayer indicates that these devices suffer from the same problem. As already noted above side chain engineering overcomes this drawback. Adding oxygen atoms in the side chains leads to an increase of the open circuit voltage from 0.3 V to 0.46 V and to 0.5 V for P3HT, P3DOT, and P3TOT, respectively. This is consistent with the observed change of the saturation current-density (see Fig. 34) since $V_{OC} = nkT/e \times \ln(j_{SC}/j_0)$. Here j_{SC} denotes the short circuit current, e is the electric charge, n is the ideality factor of the diode, k is the Boltzmann constant, and T is the temperature. The solar cells fabricated with side chain engineered polymers exhibit a pronounced increase of the power conversion efficiency (see inset in Fig. 35). The devices prepared with P3DOT appear to be affected by shunting through pinholes, which leads to a reduced efficiency. On the other hand, hybrid solar cells prepared with P3TOT reach efficiencies close to $\eta = 10$ %. The device characteristic in

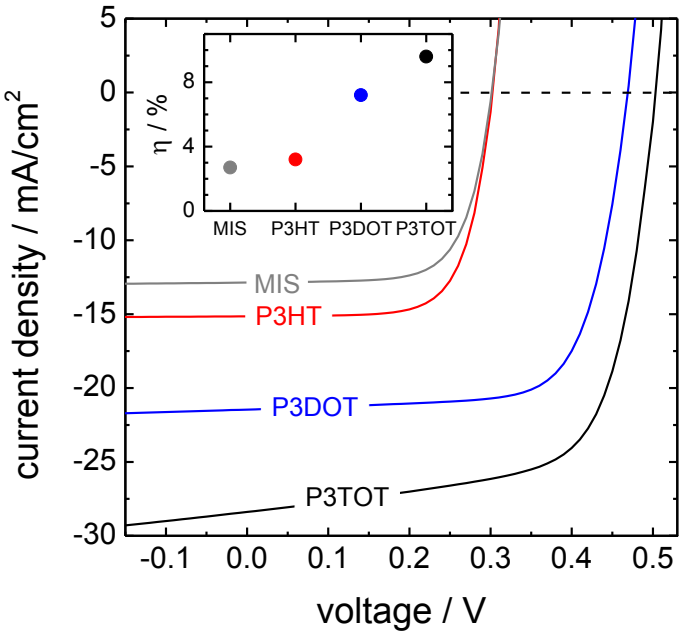

Fig. 35: Current-voltage characteristics of hybrid heterojunction solar cells with P3HT, P3DOT, and P3TOT layers. For comparison the device characteristic of a MIS structure (Au – SiO_X – c-Si) is shown (grey curve). The solar cells were measured under AM 1.5G illumination with a power density of 100 $mWcm^{-2}$. The inset shows the energy conversion efficiency, η, of the MIS device and the hybrid solar cells.

Fig. 35 indicates that the performance of the hybrid solar cell is limited by a series resistance. Most likely, this is due to poor charge-transport properties in the polymer layer. The dependence of the solar cell properties as a function of the emitter thickness of the three materials P3HT, P3DOT and P3TOT are plotted in Fig. 36 and compared to a metal insulator structure without polymer interlayer. As already mentioned, an increase in efficiency with increasing number of oxygen atoms in side chains is observed, mainly due to a boost in open circuit voltage (see Fig. 36 a)). Very thick layers (increasing polymer concentration of the solution) decrease the efficiency for all three materials and a clear maximum can be seen for P3TOT at a polymer concentration of 2 mg/ml which is followed by a systematic decrease for thicker films. For P3DOT the same trend seems to begin at a concentration of 4 mg/ml. P3HT almost gives constant values, obviously due to shunting of the gold to Si.

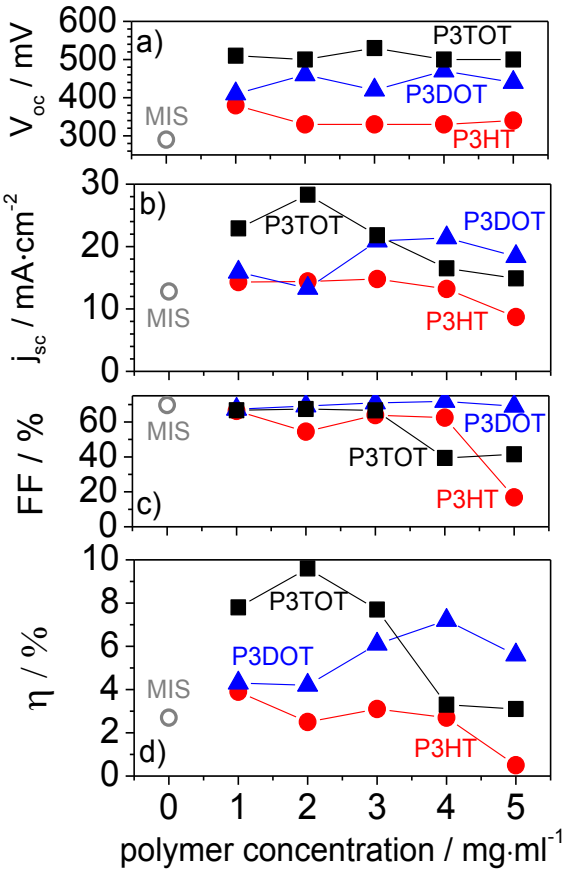

Fig. 36: a) V_{oc}, **b)** j_{sc}, **c)** fill factor, and **d)** power conversion efficiency of the MIS structure (grey open circles) and silicon hybrid solar cells under illumination (AM 1.5G, 100 mW·cm^{-2}) w/o anode buffer layers as a function of the polymer concentration used for the spin coating process (layer thickness), P3HT (red circles), P3DOT (blue triangles), and P3TOT (black squares).

5.3 Ultrathin molybdenum oxide anode buffer layer for hybrid solar cells

In the last chapter, it was shown that changes of the peripheral side chain of regioregular P3HT influence structural, electrical, and optical properties of the polymers and consequently the efficiency of the hybrid solar cells. The ether groups in the side chains of P3DOT and P3TOT resulted in better adhesion and therefore more homogeneous and electronically enhanced polymer/SiO_x interfaces. The high degree of crystallinity in side-chain modified poly-thiophenes could efficiently prevent the direct contact of Au and Si. Consequently, the efficiency of planar hybrid solar cells increased to $\eta = 9.6$ % for P3TOT. Au/Si interfaces suffer from fact, that Au atoms form mid-gap defects, which limit the height of rectifying Schottky barrier due to Fermi-level-pinning. Strong shunting of the thin and soft polymer emitter

prevents the investigation of the interface of interest, in our case the silicon/polymer interface. The introduction of an inorganic anode buffer material based on a metal oxide, e.g. molybdenum oxide (MoO_X) between the organic material and the transparent front contact is a possibility to preserve the silicon/polymer heterojunction. In organic light emitting devices MoO_X enhanced the hole injection properties [113,114]. As an anode buffer layer in organic solar cells [115] it was shown to additionally reduce the deposition damages to the polymer layer [116]. Furthermore, very thin MoO_X films between 6 nm and 22 nm already give the desired properties in the devices [89]. The metal oxide was deposited according to section 4.4. The results

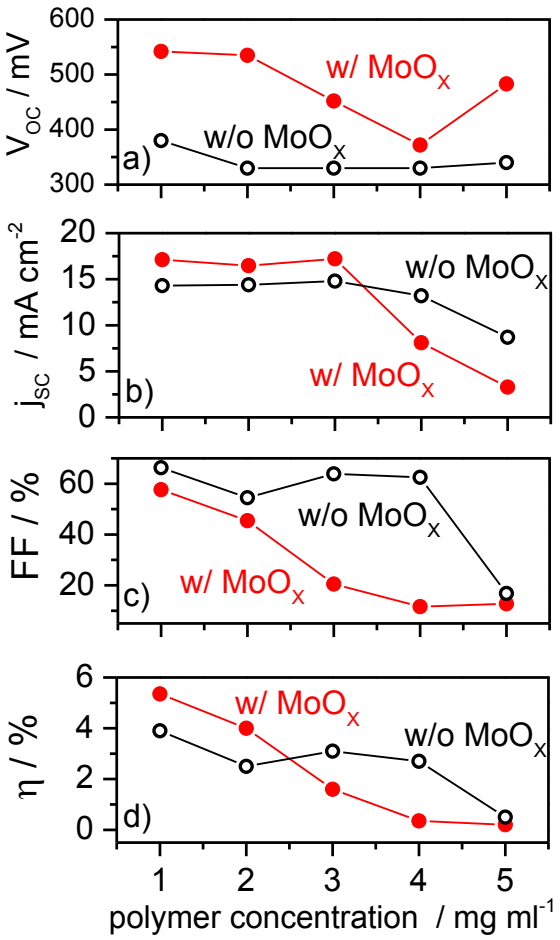

Fig. 37: a) V_{oc}, **b)** j_{sc}, **c)** fill factor, and **d)** power conversion efficiency of P3HT/silicon hybrid solar cells under illumination (AM 1.5G, 100 mW·cm^{-2}) w/ (red dots) and w/o (black circles) MoO_X anode buffer layers as a function of the polymer concentration used for the spin coating process (layer thickness).

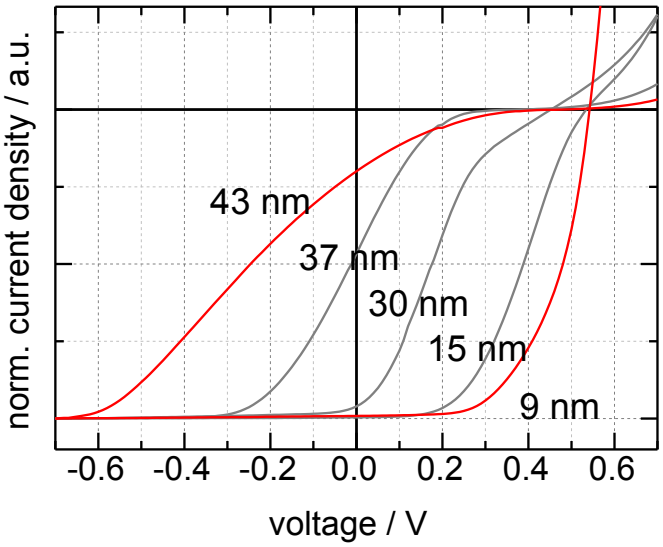

Fig. 38: Emitter thickness variation for P3HT/c-Si hybrid solar cells. Thicker emitter layers reduce the fill factor and lead to the development of s-shapes. Currents are matched at high negative bias voltages for sake of clarity.

with and without anode buffer layer are compared in Fig. 37. First, the increase in open circuit voltage to the level as obtained for P3TOT (see Fig. 36 a)) is striking. While the current only increases slightly and the fill factor even decreases. Furthermore, clear trends for the key figures become obvious now. The trend for thinner films being beneficial for the device performance has only been implied in the data before (see Fig. 36). Now the highest efficiency device has consequently the thinnest polymer layer. While open circuit voltages remain constant until a certain emitter thickness, the fill factor decreases immediately from 58 % to 11 %. The graph for the overall device efficiency resembles closely the shape of the graph for the thickness dependency of the fill factor. To understand this trends, the j(V)-characteristics of the devices with buffer layer are presented in Fig. 38. The thickness of the polymer emitter layer mainly affects the fill factor of these devices. The overall decrease in fill factor for the devices with MoO_X is caused by the increase in series resistance by the additional layer in the device structure. The decrease in open circuit voltage and short circuit current are merely due to the development of a strong s-shape, which starts to affect especially the short circuit currents. At high negative bias voltages the currents reach similar

values for all thicknesses. Short-circuit current variations at high bias voltages are smaller than 1 mA / cm^{-2} and can be treated as equal within the error. The emitter layer thickness does not affect the charge generation in the silicon wafer, but impedes the charge extraction for thick polymer layers. In combination with the wide band gap SiO_X passivation, only 15 nm of polymer are enough for the onset of s-shapes. This behavior originates most likely from charge transport limitations in the polymer layer.

A thin molybdenum oxide interlayer between the semitransparent Au front contact and the polymer layer increased the efficiency of the hybrid solar cells by increasing the open circuit voltage significantly. The solar cell performance with P3HT reached an efficiency of $\eta = 5.3$ % with an open circuit voltage $V_{OC} = 542$ mV, a short circuit current density of $j_{SC} = 17.1$ mA /cm^{-2} and a fill factor of FF = 57.6 %. The polymer no longer has to act as a mechanical barrier between the silicon and the gold and preserves the c-Si/P3HT heterojunction.

Comparison of P3HT, P3DOT and P3TOT with an anode buffer interlayer

The introduction of the metal oxide interlayer allows comparing the three different polymer/Si interfaces without being limited by the drawbacks of a conventional Schottky solar cell. Fig. 39 shows the best performing devices for the three polythiophenes. Please not that some of the device improvement is caused by a shift of the complete fabrication process into inert gas atmosphere. The influence of ambient conditions on the device performance will be investigated in a later chapter. The most obvious change compared to the devices without MoO_X (see Fig. 35) is the more similar performance of the three materials. The commercial available material P3HT provides the highest fill factors. This indicates that the longest polymer chains are connected to a high mobility. P3DOT and P3TOT on the other hand increase the open circuit voltage from 612 mV to 650 mV and 659 mV for P3TOT, P3DOT respectively. Please note that these values for P3DOT and P3TOT represent

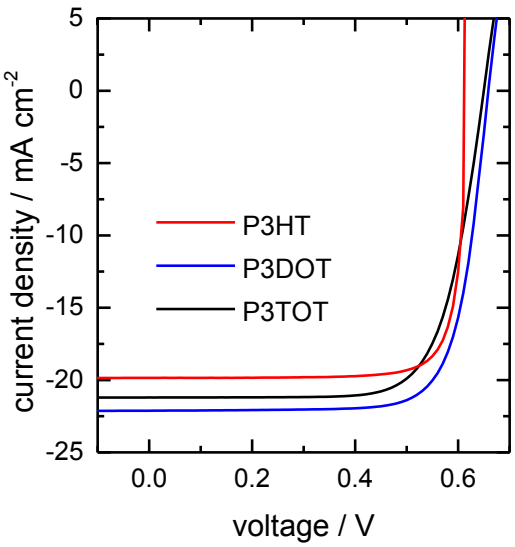

Fig. 39: Comparison of P3HT, P3DOT and P3TOT as solution processed emitter layer in Si-based hybrid solar cells. The polymer layers were protected using a MoO_X anode buffer layer before applying the Au contacts. The key figures are summarized in Tab. 5.

the highest reported for this device type of solar cells in literature [14,19,117]. The MoO_X anode buffer layer led to an increase in efficiency and reproducibility. Therefore it was possible to increase the cell size to 1×1 cm^2. With an optimized set of preparation parameters and the introduction of the MoO_X anode buffer layer solar cells with efficiencies up to $\eta = 11$ % were realized without any light trapping scheme. This leads to an optimistic outlook for this low temperature and solution processing solar cell preparation process when a light trapping scheme is introduced.

Tab. 5: Key figures of the best performing devices with P3HT, P3DOT and P3TOT. See also Fig. 39.

	V_{OC} / mV	j_{SC} / mA cm^{-2}	FF / %	η / %
P3HT	612	19.8	83.1	10.1
P3DOT	659	22.1	75.7	11.0
P3TOT	650	21.2	72.4	9.9

6. The crystalline silicon/polymer interface

The efficiency of heterojunction solar cells is always strongly dependent on the interface between the two materials combined. Numerous material parameters have to be taken into account to achieve a fundamental understanding. In organic photovoltaics the interface between two organic materials allows for the separation of photogenerated excitons. For this process to occur efficiently, the energy levels of the organic molecules, namely HOMO and LUMO, play an important role. Excitons reaching the heterojunction are separated into an electron on the acceptor and a hole on the donor if the energy step exceeds at least the exciton binding energy [118]*. More recently, the empirical correlation* [119]*,* $eV_{OC} = E_L^A - E_H^D - 0.3 \ldots 0.7\ eV$*, between the open circuit voltage* V_{OC} *and the energy difference between the hole transport level in the donor valence band* E_H^D *and the electron transport level at the acceptor conduction band* E_L^A *could be determined more accurately with the value 0.5 eV* [120]*. This value, effectively reducing the open circuit voltage, is ascribed to the formation of a lower energy charge transfer state at the interface* [121]*. Also in inorganic materials the interface plays a major role for the device performance. Next to the interface passivation of c-Si* [122,123]*, the band offsets* [124] *or the band bending in the absorber* [125] *are of particular interest for developing efficient photovoltaic devices. The combination of silicon with organic materials is quite a new field in which little work has been done so far. However, recent publications report that the use of PEDOT:PSS as an emitter drives the silicon in a state of strong inversion and causes the formation of an abrupt p/n-junction with high power conversion efficiencies* [15,126]*. Due to the "metal-like" highly doped conductive behavior of PEDOT:PSS, the results found with this material cannot necessarily be transferred to others. In this chapter, the silicon/polymer interface is investigated. In the first part the hybrid solar cells are compared to a-Si:H/c-Si solar*

cells. The main focus of attention is put on the excess charge carrier generation and the interface passivation. UPS/XPS measurements were used to determine a full energy level diagram of the P3HT/n-Si interface. This includes band offsets, position of the HOMO-LUMO energy levels in relation to the silicon valence and conduction bands, the influence of charges in the SiO_X and the band bending in the silicon upon deposition of the polymer. SPV measurements were used to determine the influence of additional layers not accessible with photoemission spectroscopy.

6.1 Comparison to a-Si:H/c-Si heterojunction solar cells

In heterojunction solar cells the interface is of special interest as it strongly determines the device efficiency by controlling the recombination in the device. Hybrid solar cells based on crystalline silicon commonly use three different types of passivation, e.g. a silicon oxide [127], a hydrogen termination achieved by dipping the silicon in HF [15] and a passivation by small organic methyl molecules [128]. While the first two are very easy to prepare, they both have certain disadvantages. The natural oxide provides a stable interface and a good substrate for the spin coating process, however, the interface defect concentration is high. The same passivation limits the open circuit voltage in a-Si:H/c-Si heterojunctions to values below $V_{OC} < 560$ mV (see chapter 2.4). The hydrogenated silicon surface, which provides a very good chemical passivation, is not stable in air and change of the surface during spin coating has to be taken into account. In section 4.1 the passivation of c-Si via H-termination, SiO_X and electrochemical grafting is explained and characterized. The CH_3-surface passivation provides good stability while preserving the high quality chemical passivation of the hydrogen.

To test for the influence of the passivation quality in hybrid solar cells devices were fabricated with a low quality SiO_X passivation and cells with the high quality and stable CH_3-passivation and compared to inorganic a-Si:H/c-Si heterojunctions with a high quality (5nm intrinsic a-Si:H) and a low quality passivation layer (SiO_X). The influence of the passivation layer in inorganic heterostructures is well known from literature and described in section 2.4. This chapter also shows the j(V) curves of the inorganic heterojunction solar cells, which were used as a reference in this chapter. These devices exhibit a difference of more than 100 mV open circuit voltage upon variation of the passivation layer. A similar behavior is expected from the hybrid solar cells. In addition, quantum efficiency measurements of both device types were conducted to determine parasitic absorption in the solar cell. To make the two device types more comparable regarding its optical properties, both used a thermally evaporated gold front contact. The hybrid solar cells had an

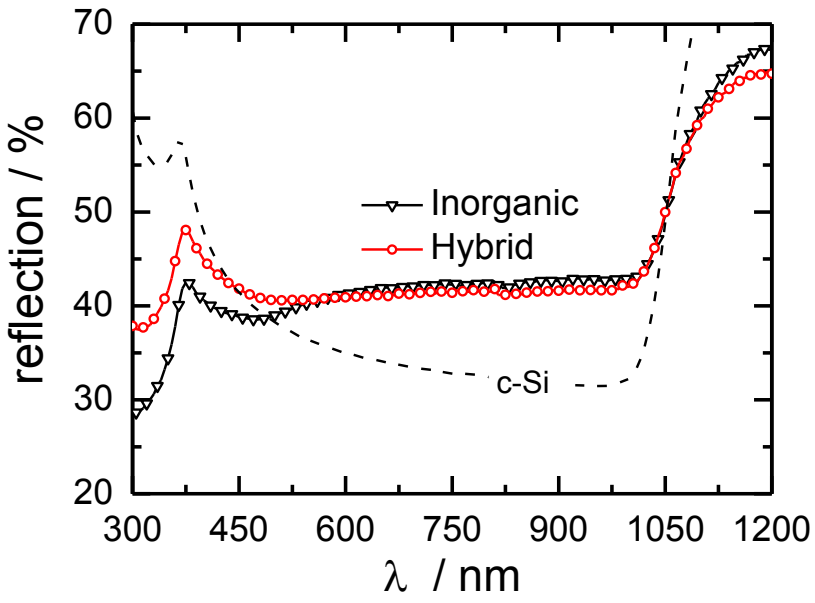

Fig. 40: Reflection spectra of a P3HT/c-Si hybrid solar cell (hybrid) and an a-Si:H/c-Si heterostructure (inorganic), each with a gold front contact. In both cases the reflection is dominated by the silicon wafer (c-Si).

additional molybdenum oxide anode buffer layer as introduced in 5.3. Neither the metal oxide nor any of the emitter layers influence the reflection of the device and therefore the amount of light absorbed. In both cases is the reflection dominated by a combination of the silicon wafer and the gold contact, which increases the overall reflection to approximately 40 % on average (see Fig. 40).

6.1.1 Excess carrier generation

The prerequisite to compare the hybrid solar cells to the inorganic heterojunctions is the absorption of roughly the same amount of light in both cell types. Using the same contact materials resulted in a similar reflection. The light is absorbed in the different layers of the solar cell and can potentially contribute to the current generated in the solar cell. Another possibility is the case in which a layer only absorbs light without contributing to the current.

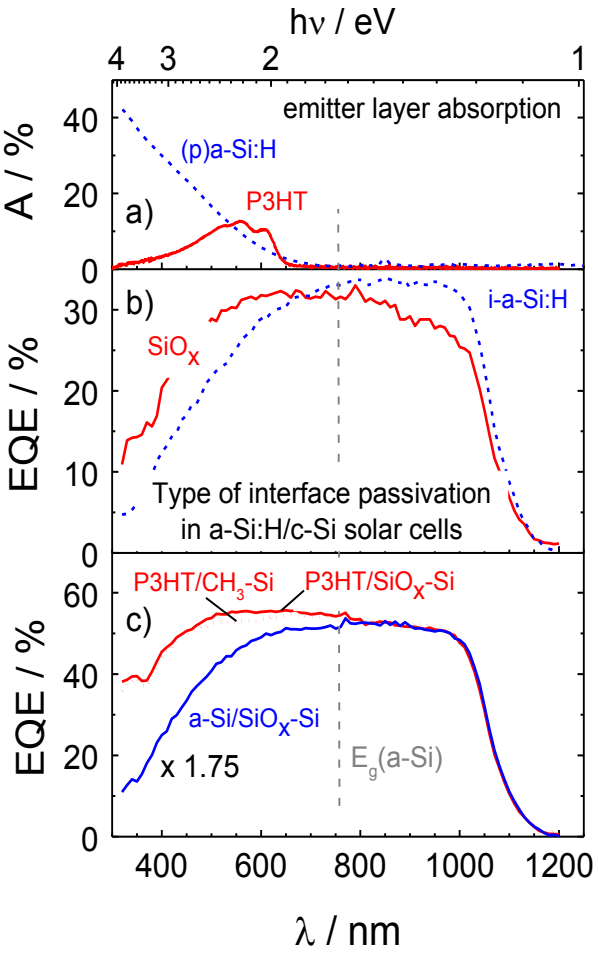

Fig. 41: a) Absorption spectra of 13 nm p-type a-Si (dashed line) and 15 nm P3HT (solid line) on glass substrates, **b)** external quantum efficiency (EQE) of a-Si:H/c-Si heterostructure solar cells with intrinsic a-Si (i-a-Si, dashed line) and SiO_X passivation (solid line) layers, **c)** EQE of P3HT/SiO_X/c-Si, a-Si/SiO_X/c-Si (solid lines), and P3HT/CH_3-Si (dashed line) solar cells

These layers are especially a problem when they are on the front side and therefore decrease the light for the active layer. This behavior is well known from silicon heterojunctions, in which the amorphous silicon layers do not contribute significantly to the current generated [129,130]. Layers, which can cause parasitic absorption are the emitter layers, passivation layers or the front contact. Fig. 41 a) shows the absorption spectra of a 13 nm p-type a-Si:H layer and a 12 nm P3HT layer on glass substrates. The HOMO to LUMO transition of P3HT starts at about 1.9 eV, has a maximum at 2.2 eV and decays towards higher energies. The absorption of a-Si starts at about 1.71 eV (E_g(a-Si)), outperforms that of the P3HT at about 2.3 eV, and finally increases with increasing light energy due to the direct proportionality of transition probability to the density of states in valence and conduction bands [131]. The

consequence of absorption in the amorphous silicon layer on the excess charge carrier generation is depicted in Fig. 41 b). By exchanging the 5 nm intrinsic a-Si:H layer with the wide band gap material SiO_X, the EQE is enhanced in the short wavelength region due to less absorption of SiO_X compared to the intrinsic a-Si layer in the a-Si/c-Si solar cell structure (see Fig. 41 a)). The reduced EQE in the long wavelength regime using SiO_X passivation is mainly a result of the much better passivation quality of the (i)a-Si/c-Si interface than of the SiO_X/c-Si interface. The current generated in the short wavelength region is even increased, when substituting the amorphous silicon emitter with the polymer layer. Fig. 41 c) compares the external quantum efficiency of hybrid solar cells with the a-Si/SiO_X/Si device. Please note that the inorganic cell in the last graph was scaled for the sake of clarity. The charge carrier generation up to 1200 nm clearly confirms the silicon as the absorber. Additionally, the CH_3-terminated Si surface in the P3HT/CH_3/c-Si solar cell device shows a slightly reduced EQE in the spectral regime of the HOMO-LUMO transition of P3HT. This is a result of an enhanced absorption by the somewhat thicker P3HT layer (~34 nm) on the hydrophobic CH_3 surface than prepared on the hydrophilic SiO_X surface (~15 nm). Nevertheless is the parasitic absorption in the emitter layer strongly reduced for the hybrid devices compared to the inorganic solar cells using intrinsic a-Si as passivation layer.

6.1.2 Influence of the interface passivation on the open circuit voltage of hybrid solar cells

Tab. 6 shows a comparison of the emitter thickness, type of interface passivation, open circuit voltage, short circuit current, fill factor, and power conversion efficiency (η) as measured for the different types of solar cell. As expected the j_{SC} is higher for the P3HT/c-Si than for the a-Si/(i)a-Si/c-Si devices due to stronger absorption of the a-Si layer in the short wavelength region compared to P3HT (see Fig. 41 a)). The relative low η of 8 % for the a-Si/(i)a-Si/c-Si solar cell is a result of the planar structure without any light trapping scheme as used for all devices presented in Tab. 6. The thicker P3HT layer in the P3HT/CH_3/c-Si solar cell led to a much smaller FF than for the thinner layer due to the higher resistance loss. Nevertheless, the P3HT/c-Si solar structures have a power conversion efficiency η of about 10 %. The more striking observation is the almost similar open circuit voltage for the high quality CH_3- and low quality SiO_X-passivation of 617 mV and 612 mV, respectively. These values differ by only 5 mV and were reproducible for several cell charges. Especially the fact that the SiO_X-passivation reaches values above 600 mV open circuit voltage is surprising and does show that the

Tab. 6: Comparison of emitter thickness, type of interface passivation, open circuit potential (V_{OC}), short circuit current (j_{SC}), fill factor (FF), and power conversion efficiency (η) as measured for different type of inorganic and hybrid planar c-Si based heterojunction solar cells on the 1x1 cm^2 active area.

cell type	emitter thickness (nm)	Interface passivation	V_{OC} (mV)	j_{SC} (mA/cm^2)	FF (%)	η (%)
a-Si/c-Si	13±1	(i)a-Si:H	669	18.1	66.3	8.0
a-Si/c-Si	13±1	SiO_X	558	16.4	62.4	5.6
P3HT/c-Si	15±2	SiO_X	612	19.8	83.1	10.1
P3HT/c-Si	34±3	CH_3	617	20.6	72.6	9.2
P3DOT/c-Si	18±2	SiO_X	659	22.1	75.7	11.0

hybrid solar cells differ from a-Si:H/(i)a-Si/c-Si heterojunctions despite its similar structure. Furthermore, with 659 mV and 650 mV respectively, the values for P3DOT and P3TOT even exceeded the value for P3HT and are close to the values of the reference. The key figures for the devices prepared with a P3DOT emitter layer as prepared in chapter 5.3 are included in Tab. 6. A possible reason for the higher V_{OC} as well as the strongly reduced dependency of the V_{OC} on the interface passivation could be caused by different passivation capabilities of the respective polymers when deposited onto the Si wafer surface. To verify this hypothesis, Si wafer lifetime measurements[1] on test structures were conducted. The effective wafer lifetime was measured for a wafer with a-Si passivation on the backside and an oxide passivation on the front side. Fig. 42 shows the measured lifetime, τ_{15}, at a minority carrier density equal to the doping level of c-Si was 19.6 µs and increases to 37.5 µs after deposition of P3HT on the SiO_X passivation layer of the same wafer. The bulk lifetime of the wafer was determined to be 2 ms. Furthermore, the effective wafer lifetime is correlated to the so called implied open circuit voltage (iV_{OC}), which is the maximum possible V_{OC} that can be obtained when only interface recombination is the main loss process of the charge carriers. The iV_{OC} for a lifetime of τ_{15} = 19.6 µs at one sun is about 570 mV and is in good agreement with the results obtained for the a-Si/c-Si device with oxide interface passivation (558 mV, see Tab. 6). The field effect passivation [132] (no chemical reactions are expected to occur on the surface) induced by the P3HT, however, is too little to explain the high V_{OC} of the P3HT/SiO_X/c-Si devices. The other polymers did not behave different in any way despite the fact, that they exhibit higher open circuit voltages in the devices than P3HT. No significant increase in lifetime was measured.

While poly-thiophene materials lead to a field effect passivation of c-Si, which is measured as an enhanced lifetime of photogenerated charges in the Si wafer, the observed trends in the devices cannot be explained by this

[1] The effective minority charge carrier lifetime in the structures was quantified with photoconductance decay measurements on a WCT-100 by Sinton Instruments, commonly termed a "Sinton lifetime tester" [186,65]

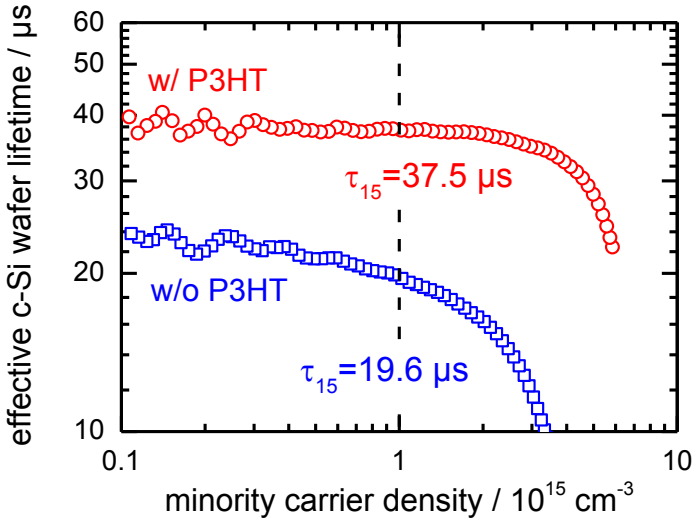

Fig. 42: Effective wafer lifetime of the same SiO_X passivated n-type c-Si wafer with and without a spin coated layer of P3HT.

effect. The lifetime values for P3HT are one order of magnitude to low, and for P3DOT lifetimes in the order of milliseconds would be necessary. The reason for the reduced dependency of the V_{OC} on the interface passivation quality is unclear so far. Further investigations are shown in the following chapters. However, the use of an organic emitter layer instead of amorphous silicon has advantages beyond the reduction of processing costs. The small absorption band of P3HT increases the absorption of the silicon in short wavelength region and therefore the charges generated in the Si wafer. Consequently, the hybrid solar cells had higher short circuit currents when using the same contact system and outperformed the inorganic solar cells fabricated for comparison.

6.2 Energetics at the c-Si/polymer interface

The combination of polymer and crystalline silicon provides an interface, which has not been investigated thoroughly, yet. The investigation of organic/inorganic interfaces rather concentrated on the situation of organic semiconductors deposited on metals or transparent conductive oxides, due to

the relevance as contacts for polymer-based electronics [133–136]. The new device type of hybrid solar cells sparked a new interest on interfaces between organic and inorganic semiconductors to determine the working principle of these devices. Naturally these efforts focus on the material combination exhibiting the highest efficiencies, namely c-Si/PEDOT:PSS. Most publications treat this interface as a Schottky device assuming a metal-like state of PEDOT:PSS [137–139]. Newer results report the formation of an inversion layer below the surface of the silicon, changing the physical properties of the device from a majority charge carrier dominated Schottky solar cell to a minority carrier determined pn-junction [15,126,140]. However, little work has been done in combination with other organic materials. Important factors like the energy level alignment, band offsets or exzitonic effects, which could influence the performance of hybrid solar cells, remain open to speculation. In this chapter UPS/XPS measurements were used to determine the underlying charge carrier generation mechanisms of the c-Si/SiO_X/polymer junction. Fig. 43 a) depicts an overview spectrum of the valence band region of a pristine Si/SiO_X substrate and of the substrates with the polymers P3HT, P3DOT and P3TOT (see section 5.1) as determined from UPS measurements. The enlarged energy range up to 2 eV below the Fermi energy, E_F, in Fig. 43 b) was used to determine the valence band onsets, corresponding to the HOMO delocalized states of the three polymer materials [141,142]. The onset for the SiO_X was found to be at $E-E_F = 4.5$ eV. The valence band onset of the substrate with P3DOT and P3TOT are similar to the value with P3HT. The values $E-E_F$ determined from the well resolved spectra in Fig. 43 b) are 0.25 eV, 0.21 eV and 0.51 eV for the polymers in the sequence P3HT, P3DOT, P3TOT. These values are comparable to the situation for polymers on a metal substrate with a low hole injection barrier [133,143]. The assumption of vacuum level alignment is not valid and according to the integer charge transfer model exhibit π-conjugated polymer molecules a minimum hole injection barrier independent of the substrate work function [144,145] rather than alignment of HOMO and the Fermi level of silicon. Therefore the energy levels of the polymer are pinned relative to the Fermi level of the substrate. The deviation of the value for P3TOT

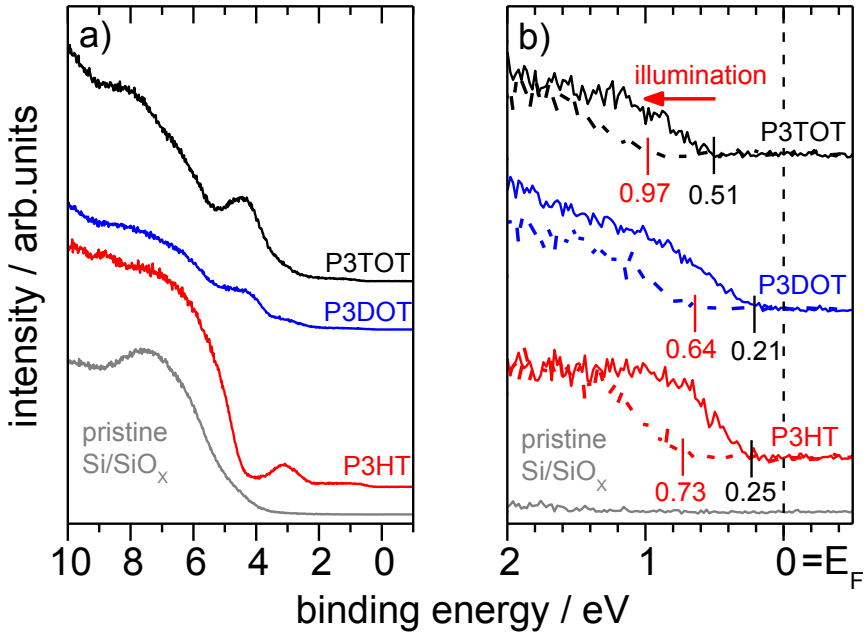

Fig. 43: **a)** Overview of the valance band region spectra of a pristine Si/SiO_x substrate and P3HT, P3DOT, and P3TOT films deposited on Si/SiO_x substrates. **b)** Valance band region spectra near E_F, solid lines were measured in the dark, dashed spectra were measured with additional white light illumination of the samples.

$E\text{-}E_F = 0.51$ eV for the valence band onset could be caused by a higher ionization energy of the polymer. The ionization energy of a polymer is orientation dependent [146] and P3TOT exhibits a strong preferential orientation parallel to the substrate of the π-stacking as described in chapter 5.2. However, variations of the substrates oxides could simply lead to pinning at a different energy level caused by the gap state distribution of the individual sample. Additional white light illumination with a halogen lamp shifts all spectra to higher binding energies. The corresponding spectra are shown in Fig. 43 and the values differ by 0.48 eV, 0.43 eV and 0.46 eV for P3HT, P3DOT and P3TOT, respectively. The shift has a photovoltaic origin and was not observed for the silicon substrate. The situation during the measurement is comparable to open circuit conditions. Charges are generated in the silicon and separated due to the silicon/polymer interface. The positive charges are accumulated in the polymer layer. The measured kinetic energy of the

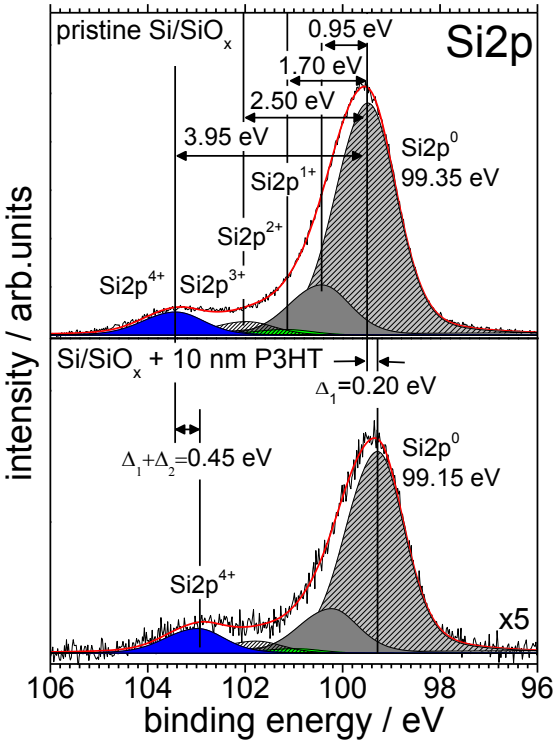

Fig. 44: Si2p core level spectra of a pristine Si/SiO_x substrate and after deposition of a thin P3HT film.

electrons is reduced and measured as an increase in binding energy. The silicon core level spectra were recorded additionally before and after the deposition of thin polymer layers. The data for P3HT in the region of the Si2p core levels are shown in Fig. 44. The dominant Si 2p peak is indicative of silicon with oxidation state zero. The peak appearing on the higher binding energy side between 101 eV and 104 eV signals for the silicon oxidation states +1…+4. The XPS spectra can be fitted using the tabulated peak positions for the different Si oxidation states [147,148]. XPS is very surface sensitive and the signal of the Si^0-peak is mostly generated from the Si atoms closest to the Si/SiO_X interface. Band bending in the silicon induced by an additional layer on top is therefore reflected in a shift of the binding energies measured with XPS. Of course, the layer deposited on top of the silicon has to be thin enough so the not oxidized silicon can still be probed. By rinsing the silicon substrate with the solvent after spin coating a very thin polymer layer for the

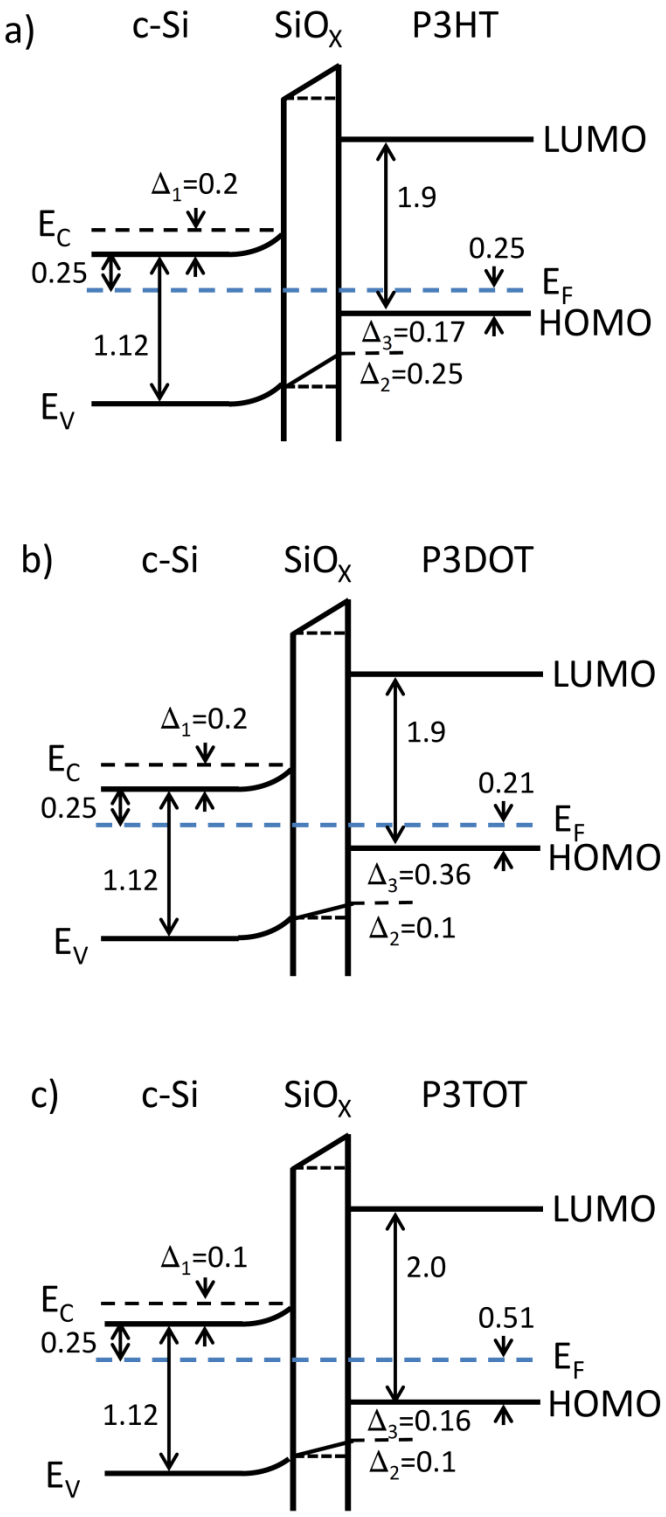

Fig. 45: Energy level alignment at the Si/SiO_X/polymer interface for **a)** P3HT, **b)** P3DOT, and **c)** P3TOT, energies in eV. The values were obtained using UPS and XPS measurements and UV-Vis spectroscopy (E_g from UV/Vis; Δ_1, Δ_2, and E_F - HOMO from Fig. 43 and Fig. 44; $E_F \cong 0.25$ eV below E_C and $E_g(Si) = 1.12$ eV from [23]. Not to scale.

measurements "Si/SiO_X + P3HT" in Fig. 44 were realized. The Si^0 and the Si^{4+} component of the spectrum shift to lower binding energies owing to the deposited polymer layer. The energy shifts amount to $\Delta_1 = 0.20$ eV and $\Delta_1 + \Delta_2 = 0.45$ eV for the Si^0 - and the Si^{4+} -peak, respectively. While the shift Δ_1 of the not oxidized silicon is directly associated to the formation of a depletion region in the Si upon deposition of the polymer, an additional potential shift $\Delta_2 = 0.25$ eV occurs across the silicon oxide layer. The analysis of the Si core level spectra upon deposition of P3DOT and P3TOT lead to the same qualitative observations. The results of all measurements have been summarized as the energy level alignments for all three c-Si/SiO_X/polymer interfaces in Fig. 45. The band gap of 1.12 eV and the position of the Fermi energy of 0.25 eV (E_C - E_F) in the Si wafer was taken from ref. [23] according to the manufacturer values for the doping density of $N_D = 10^{16}$ cm^3. The position of the HOMO energy levels allows for efficient hole transfer from Si into all three polymers. The slight band bending is in agreement with the field effect passivation observed in the previous chapter by electrostatically shielding the charge carriers from the interface by an internal electric field. This indicates that deposition of a polymer on the surface is comparable to additional fixed negative charges on the surface [149,150]. However, no systematic change regarding the number of oxygen atoms in the side chains was observed. This supports the thesis of the polymer acting as a blocking layer in a Schottky device that reduces the thermionic recombination current at the interface [14], which intrinsically restricts efficiencies in Schottky-type solar cells. The conduction band offsets of the bulk Si to the LUMO of P3HT, P3DOT, and P3TOT of about 1.4 eV, 1.44 eV and 1.24 eV are above the range in which thermionic emission is expected to be relevant. Especially, as these offsets exceed the band gap of silicon and are therefore larger than possible barrier heights for Schottky majority-carrier diodes [23]. However, the observation of high open circuit voltages using a low quality passivation cannot be explained by the introduction of a mere blocking layer. While the polymer prevents the generation of new defects by preventing the direct contact of metal and silicon, it does not passivate the defects already present at

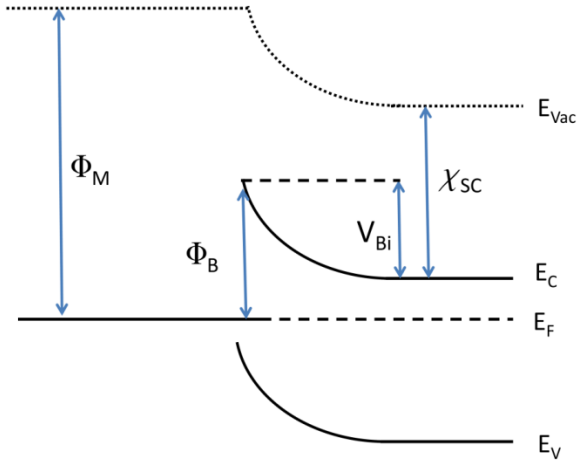

Fig. 46: Sketch of the Schottky-Mott model of an n-type semiconductor after contact with a high-work-function metal

the semiconductor surface. Structural dependence as well as reduced influence of surface states have been reported by *Green et al.* [151]. He concluded that dynamic effects of the surface states are generally negligible for MIS devices with an inversion layer at the interface [151] (IL-MIS device). Also surface defect states higher than 10^{13} cm^{-2} can be tolerated without significantly diminishing device performance. The underlying physics of inversion layer solar cells is the Schottky-Mott model in which a high-work-function metal is brought into contact with an n-type semiconductor as sketched in Fig. 46. The difference in the electrochemical potentials leads to a depletion of electrons in the semiconductor and consequently to the formation of the barrier $\Phi_B = \Phi_M - \chi_{SC}$ with the metal work function, Φ_M, and semiconductor electron affinity, χ_{SC}. The formation of this barrier is accompanied by band bending in the silicon amounting to $V_{Bi} = \Phi_M - E_F$. For a strong band bending the semiconductor surface is driven into inversion [140]. The term describes the following majority- and minority-carrier density situation in the semiconductor material. The majority- and minority-carrier densities will be termed [maj] and [min], the situation at the surface space charge region will be indexed with $_{SURF}$ and $_{BULK}$ in the bulk of the material. In general, the semiconductor surface is in

1. accumulation if $[maj]_{SURF} > [maj]_{BULK}$;
2. depletion if $[maj]_{SURF} < [maj]_{BULK}$.

Type-inversion is valid for an n-type semiconductor if the minority charge carrier density exceeds the majority concentration. Two cases can be distinguished:

3. inversion is valid if $[min]_{SURF} > [maj]_{SURF}$.

For cases of strong band bending

4. strong inversion occurs, in which $[min]_{SURF} > [maj]_{BULK}$.

Larger potential differences will be compensated by migration of holes from the bulk into the space charge region and no stronger depletion occurs. Under strong inversion, the minority charge carriers from the bulk form the majority charge carriers close to the semiconductors surface. A pn-junction is formed just below the surface [15,126,140] without the need for a diffusion process or any other defect-introducing steps. Analyzing Fig. 46 one can conclude that inversion occurs when $V_{Bi} > E_F - E_i$. For the strong inversion threshold the relation changes to $V_{Bi} > 2|E_F - E_i|$. With the dependence of the Fermi-energy E_F and the intrinsic Fermi-energy E_i, the inversion and the strong inversion threshold are dependent on the doping density of the silicon and are calculated for $N_D = 10^{16}$ cm^3 in Fig. 47. Fig. 47 itemizes the influence of the individual layers on V_{BI}. Every layer given in the x-axis is added to the previous one until the layer stack c-Si/SiO_X/20 nm P3HT/5 nm MoO_X/12 nm Au is complete. The band bending in the underlying silicon is measured with the surface photovoltage technique introduced in chapter 3.1. Compared to photoemission spectroscopy the measurement method is not restricted by the universal curve [79] for the penetration depth of electrons to generate its signal and allows for the measurement of the band bending in the Si substrate with the interface covered by several layers. SPV determines the flat band conditions by illuminating the sample with a 900 nm laser. Therefore it is possible to

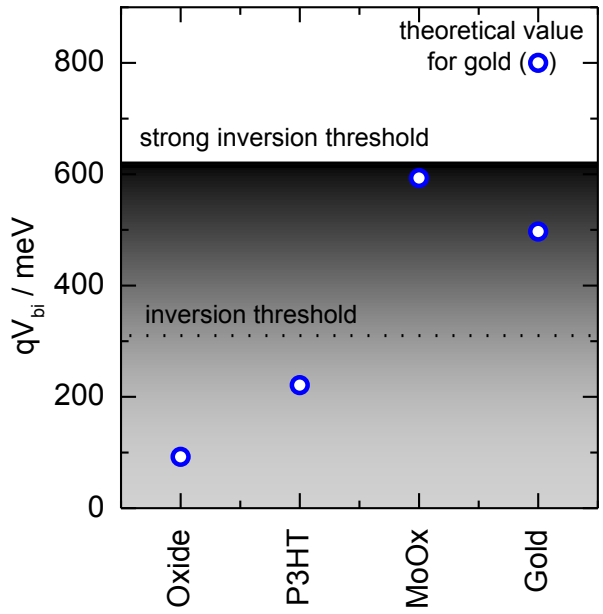

Fig. 47: Development of the band bending in hybrid solar cells for deposition of the individual functional layers

determine the band bending of 92 meV caused by charged defect states in the non-stoichiometric oxide [152,153] (see Fig. 44). As already established above, an additional poly-thiophene layer only yields to a minor band bending of roughly 200 meV in the Si. The value determined by SPV for P3HT is with 220 meV in good agreement with the UPS/XPS results. The amount of band bending resides below the threshold for inversion. Adding the MoO_X layer increases the band bending close to the strong inversion threshold. The result is not surprising as MoO_X is under investigation as a low absorption emitter for silicon [154]. The addition of the gold layer leads to a reduction of the measured band bending. However, this is most likely due to a restriction of the measurement method. The additional gold layer absorbs too much light intensity of the 900 nm laser. As a consequence, the prerequisite of flat band conditions in the silicon upon illumination is not satisfied and V_{Bi} is underestimated. On this account two measures were taken to estimate the error introduced by the measurement method. In Fig. 47, the theoretical value for

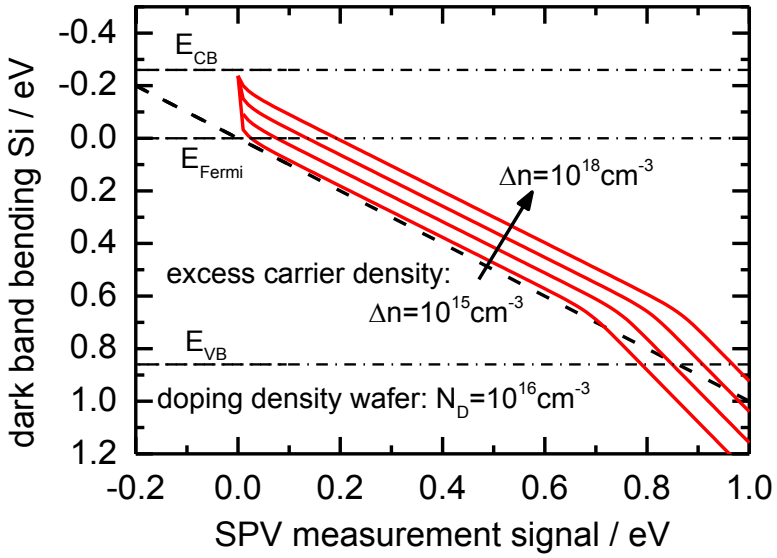

Fig. 48: Dependency between measured SPV-signal and dark band bending for a n-type silicon wafer with a doping density of $N_D=10^{15}cm^{-3}$ for different excess carrier densities. Position of the band edges, Fermi level and f(x)=-x are drawn for orientation.

gold according to the Schottky theory for a gold work function of $\Phi_{Au} = 5.2$ eV is added. This value is expected to overestimate the barrier height. For one, a typical value for a naturally passivated gold surface is probably lower [133,155]. However it is unlikely that the gold layer reduces the band bending in the silicon and indicates the formation of an inversion layer below the interface. Additionally, the dependency of the measured SPV-signal on the excess charge carrier density Δn was calculated according to the considerations of Heilig et al.[67] (see appendix). The result is displayed in Fig. 48. The excess carrier density for laser used was determined to 10^{17} cm^{-3} for the setup used [156]. The value depends on the laser intensity and the absorbed fraction of the laser, hence the optical properties of the sample. Fig. 48 identifies the limits of the SPV technique as a measurement method to determine the band bending in the Si. For low excess carrier densities, Δn, the measured SPV-signal reflects the actual band bending in Si. For higher Δn the SPV signal is shifted due to the increasing value of the Dember voltage, an additional part of the signal

resulting from the different mobility values for holes and electrons in Si [157]. However, this effect can be treated mathematically for known laser intensity and the respective excess carrier density Δn. At higher band bending, a deviation from unity (dashed black line) occurs and leads to an underestimation of V_{bi}, starting for values of 0.6 eV. While the 900 nm laser is not absorbed in the MoO_X or P3HT, the gold layer leads to an overestimation of Δn due to the strong absorption in the infrared light range. As a consequence, the measurement method of SPV systematically underestimates V_{bi}. Especially the value for gold in Fig. 47 is strongly underestimated and it is very likely that the band bending in the final device exceeds the strong inversion threshold.

In conclusion, comparing the hybrid devices to a-Si:H/c-Si solar cells, the polymer layer leads to an increase in short circuit current due to reduced parasitic absorption in the short wavelength region. While the inorganic heterojunctions discussed in this chapter show a strong dependency on the interface passivation, the hybrid devices are almost independent of surface defect density. To identify the reason for this behavior, the c-Si/polymer interface was investigated in detail. UPS/XPS measurements exhibited similarities to polymer/metal interfaces and a band bending in Si was associated to the deposited poly-thiophene layer. However, the main fraction of the band bending is caused by the front contact system MoO_X/Au, which shifts V_{bi} close to the strong inversion threshold. Due to a systematic error of the measurement method, the values for V_{bi} determined by SPV are underestimated. It is likely that even strong inversion occurs in the device. Consequently, the devices used in this thesis have the same working principle as reported for hybrid devices using PEDOT:PSS [15,126] as an emitter layer. However, the band bending is not caused by the organic layer. Moreover, the poly-thiophene layer in the solar cell act rather as an additional blocking layer in a Schottky-type solar cell. Nevertheless, the metal front contact should be avoided as it limits the short circuit current and ultimately the device efficiency. The following sections are focused on possibilities to circumvent the use of a gold front contact.

7. Large area CVD-graphene as a transparent and conductive contact system for Si based hybrid solar cells

One reason why graphene research has progressed that fast is the easy laboratory procedure for preparing high-quality graphene, namely the "Scotch-Tape" method [158]*. Many of its striking material characteristics as the high room-temperature electron mobility (2x10*^{5} $cm^2\ V^{-1}\ s^{-1}$*)* [159]*, the very high thermal conductivity (>3000* $W\ mK^{-1}$*)* [160] *or the optical absorption of exactly* $\pi \times \alpha \approx 2.3\%$ *(where* α *is the fine structure constant)* [161] *were measured on small graphene flakes. However, for most real-life applications large-area graphene is necessary. In this chapter, a study on the feasibility of large-area graphene as a transparent and conductive front contact for Si based hybrid solar cells is presented. High-quality and large-area graphene is synthesized on copper foil with a CVD process. The usual transfer process from the growth substrate on the sample is adapted for thin polymer layers as used in the hybrid solar cells. The quality of the graphene-sheet is quantified using the 2D-Mode of the Raman spectra after the deposition as the front contact of the solar cell. The electronic properties of graphene with different underlying polymer layers, e.g. PEDOT:PSS, PCBM, Spiro-MeOTaD and P3HT, is investigated to determine the influence of the underlying material on the conductivity of graphene. Solar cells fabricated with a single-layer of graphene reached a maximum external quantum efficiency of 6.17 % on a planar substrate. The overall efficiency of* $\eta = 4.7\ \%$ *is limited by the electronic properties of undoped graphene and the resulting low fill factor of FF = 36.7 %. The analysis of the graphene on the series resistance of the device indicates that the concept of the graphene anode could be optimized to overcome the restrictions connected to the low conductivity of single-layer graphene.*

7.1 Fabrication and transfer of graphene

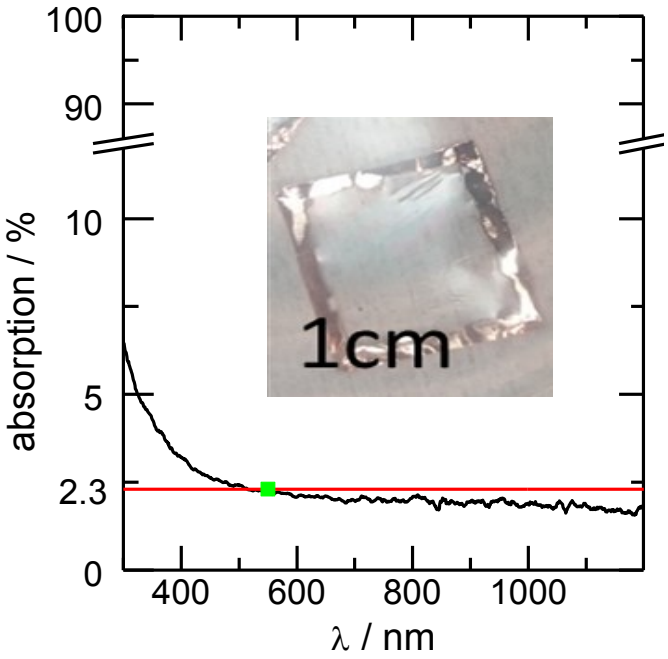

Fig. 49: Absorption spectrum of single-layer graphene. Red line indicates value for theoretical absorption in single-layer graphene of 2.3 %. The value is typically determined at 550 nm (green square). Inset shows graphene protected by nitrocellulose support just before transfer to any desired substrate.

Large-area CVD-graphene was deposited on a 25 µm thick copper foil via catalytic decomposition of methane. Beforehand the foil was polished and sonicated with acetone and isopropanol for 10 min. Additional sonication for 10 min with acetic acid removed any residual copper oxides. The actual growth process was carried out in a quartz tube furnace. The CVD growth of graphene used a two-step process. The first 30 min hydrogen (H_2) was streamed across the copper foil at a flow rate of 2 sccm to recrystallize the surface. The pressure amounted to 1 mbar and the temperature to 1000 °C. After additional 30 min at reduced hydrogen flow rate of 0.7 sccm the precursor gas methane was introduced to the process at a flow rate of 11.4 sccm. The actual growth process was carried out at 0.5 mbar for 1 h. The resulting graphene sheets had a typical size of several square centimeters and were cut to the desired size of ~ 1 cm^2 for use as a transparent front contact.

For the transfer process [162] from the growth substrate to the sample, nitrocellulose was spin-coated as a support for the graphene on the graphene-coated copper foil. Subsequently, the copper substrate was etched off with a 3M $FeCl_3$ solution and cleaned with high purity water. The inset in Fig. 49 shows a sheet of graphene stabilized by the nitrocellulose support just before transfer to any desired substrate. The copper frame is intentionally protected from being etched for easier handling. In the next step of the transfer a drop of a nonpolar solvent was put on the desired substrate and the graphene sheet was set floating on top. During evaporation of the solvent on a hotplate set to 55 °C, the graphene sheet adapts to the substrate. The solvent hexane was chosen to avoid dissolving of any underlying organic materials. The support can be removed afterwards by washing the sample in ethyl acetate.
For the absorption spectrum in Fig. 49 graphene was transferred onto a quartz substrate. The absorption of graphene provides an easy method to determine the number of layers. The red line quantifies the theoretical absorption of a single-layer graphene. The value of $A_1 \approx 2.3\%$ for a single layer is added for every additional layer [163], according to the simple correlation $A_n = nA_1$. In literature the term graphene is used for materials with $n \leq 5$ [164,165]. The transmission of the measured graphene layer is slightly higher, which could be caused by holes in the graphene. However, the measurement clearly shows the single-layered nature of the graphene.

Raman measurements provide another useful tool to characterize graphene. The Raman spectrum of graphene has two characteristic phonon peaks, The G-phonon mode at $\nu_G = 1580\ cm^{-1}$ and the 2D-phonon mode at $\nu_{2D} = 2700\ cm^{-1}$. These two modes are shown in the reference spectrum taken from graphene transferred onto glass in Fig. 50. A high intensity ration of $I_{2D}/I_G \approx 2$ of these two modes is an indication for high quality single-layer graphene [166]. However, it should be noted that other factors affect this intensity ratios, e.g. the Raman excitation energy [167] or the (field effect) doping [167,168]. The more reliable indicator for the quality of graphene layers is the D-mode, or defect mode at $\nu_D = 1350\ cm^{-1}$. While the G-phonon mode can be ascribed

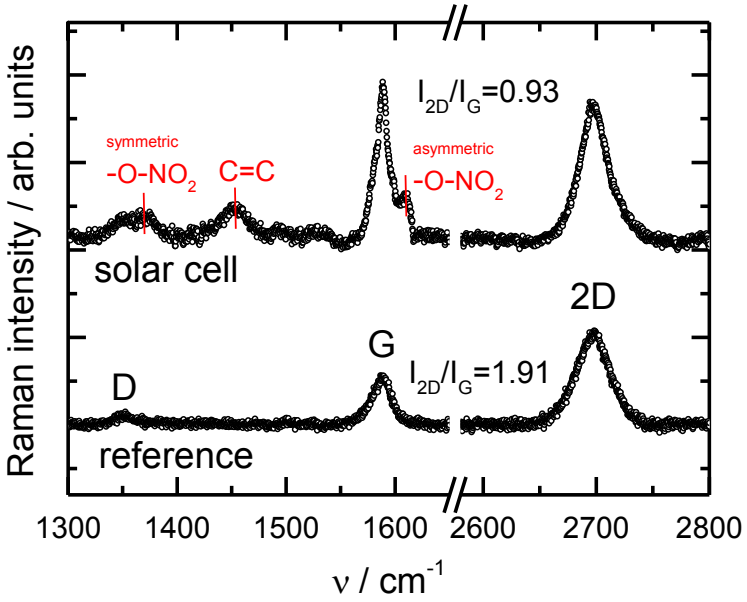

Fig. 50: Raman spectra of single-layer graphene transferred on glass as reference and as used in the solar cell. In the solar cell the nitrocellulose support is not removed.

to a first order scattering process and the 2D phonon mode to a second order scattering process occurring under the involvement of two phonons, the D mode only occurs in the presence of defects [169]. The low intensity of the D mode in the reference spectrum pinpoints the high quality of the graphene and the transfer process used in this study. The upper spectrum was taken from the graphene layer transferred onto the solar cell as a transparent front contact (Fig. 50 "solar cell"). The spectrum differs significantly from the reference spectrum. The ratio of the intrinsic Raman modes is reduced to $I_{2D}/I_G = 0.93$ the D mode seems to broaden. However, these observations as well as the occurrence of an additional peak at approx. 1450 cm^{-1} is connected to the nitrocellulose support, which was left on the device to avoid an additional solvent step necessary to wash off the support lack. The symmetric and asymmetric stretching bands of covalent nitrates (-O-NO_2) are located at 1285-1270 cm^{-1} and 1640-1620 cm^{-1}, respectively [80]. We also ascribe the altered intensity ratio of the 2D and G mode to the presence of the asymmetric stretching mode, which can also occur as a doublet. Field effect doping in the graphene due to the presence of the support provides a further explanation [168].

The peak at the C=C double bond position is caused by the oxygen containing 6-membered tetrahydropyran ring in the support. But more importantly, the changes in the spectrum can be easily explained by the presence of the support. The only mode which is not affected is the 2D mode. The shape of the 2D mode, as well as the intensity, does not differ significantly from the reference. Therefore, a high quality single-layer graphene can be assumed for the use as a transparent front contact.

7.2 Device design

The hybrid solar cells, on which the graphene was transferred on, were fabricated according to section 4 using the methyl surface passivation. As an electric contact for the graphene, two gold bus bars were evaporated on the solar cells. The graphene was deposited on top as shown in Fig. 51. This device structure allows for the measurement of the graphene sheet resistance. Furthermore, a reference solar cell was fabricated on the very same substrate using the contact system introduced in 5.3, before transferring the graphene in ambient.

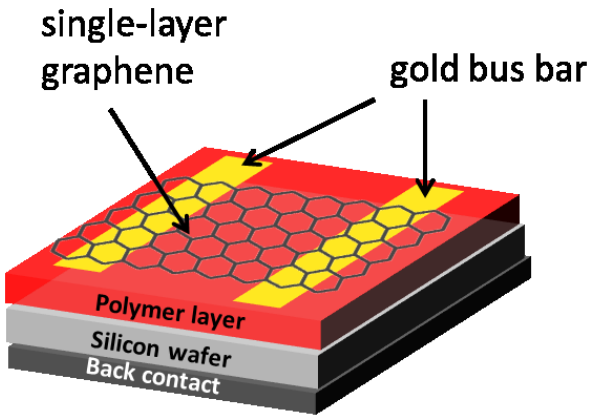

Fig. 51: Device design for hybrid solar cells with large-area graphene as a transparent front contact system.

7.3 Solar cell results

Two types of devices have been fabricated on the same substrates. Both were c-Si/P3HT heterojunctions with a methylpassivation. One device uses a single-layer graphene as front contact, the other our standard gold front contact. The j(V)-characteristics in the dark and illuminated are presented in Fig. 52 and the detailed parameters are summarized in Tab. 7. Please note that these devices were partly fabricated in ambient and therefore the efficiencies of chapter 5.3 are not reached. The effect of degradation is described in chapter 8.3. The reference cell reaches a power conversion efficiency of $\eta = 6.71$ % with a $j_{SC} = 21.8$ mA cm^{-2} , FF = 49.1 % and $V_{OC} = 582$ mV. It is interesting to note that the transfer process did not affect the junction quality by rinsing off the polymer P3HT and the graphene device reached the same high value for the open circuit voltage of $V_{OC} = 584$ mV. However, the win in short circuit current is much lower than expected. The low short circuit current

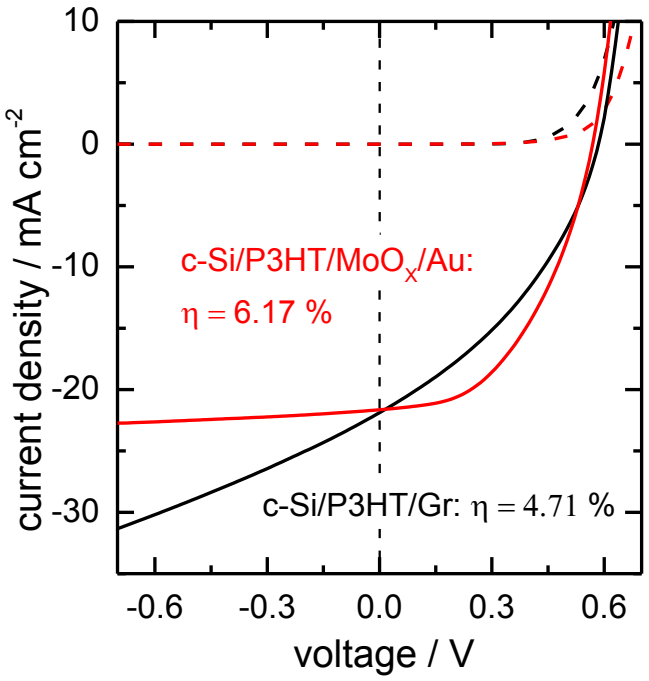

Fig. 52: j(V)-characteristics in the dark and illuminated with graphene front contact and the gold reference on the same substrate.

Tab. 7: Solar cell characteristics for the devices demonstrated in Fig. 52.

contact systeme	η / %	V_{OC} / mV	j_{SC} / mA cm^{-2}	$j_{SC,EQE}$ / mA cm^{-2}	FF / %
Graphene	4.71	584	22.0	25.4	36.7
Au	6.17	582	21.8	21.4	49.1

is connected to the fill factor of FF = 36.7 %, especially as the current values reach > 30 mA cm^{-2} for bias voltages of -0.6 V. The low fill factor is directly reflected in the series resistances. The reference has a series resistance of $R_{S,Au}$ = 22.4 Ω cm^{-2}. In the graphene device this value significantly higher ($R_{S,Gr}$ = 63.3 Ω cm^{-2}). Another fact worth to mention is the difference between the short circuit current determined under AM1.5G conditions and the current from the spectral response measurements, which was not observed for the Au-reference. Fig. 53 shows the external (EQE) and internal (IQE) quantum efficiency measurements for both devices. The gold reference had a maximum EQE of 54.3 % and the integrated current $j_{SC, Au}$ = 21.4 mA cm^{-2}, which matches the current from the j(V)-characteristics (see Tab. 7). The superior optical properties of the graphene-contact lead to an overall higher EQE with a maximum value of 67.1 % and the integrated current amounts to $j_{SC, Gr}$ = 25.4 mA cm^{-2}. A value, which is more than 3 mA cm^{-2} higher than the value determined under AM 1.5G conditions. Furthermore, the EQE of Graphene exhibits an interference pattern, caused by the support left on after the transfer. This pattern is reduced in IQE spectrum for graphene. When comparing the IQEs of the two contact systems, the relations are reversed. The IQE for gold reaches 91.6 %, while the IQE for graphene amounts to a lower value of 82.6 %. While good electrical properties are expected for a thermally evaporated gold contact, the high IQE is nevertheless surprising. However, the average reflection of 40 % with gold reduces the current compared to graphene significantly.

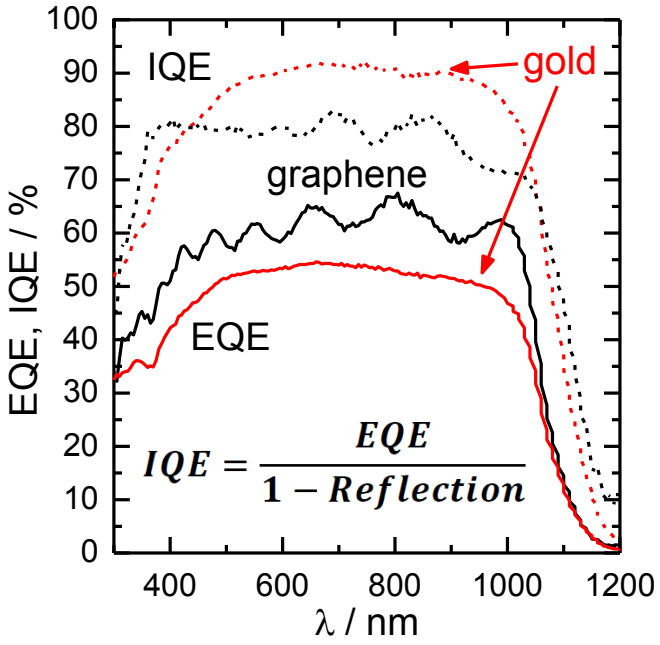

Fig. 53: EQE and IQE spectra of the gold and graphene contact. The higher EQE of the graphene contact points out the superior optical properties of the graphene.

7.4 Electrical properties of graphene

Additional to a high transmission (see Fig. 49), a good electric conductivity is a premise for a solar cell front contact. The combination of both is usually only found in metal oxides, e.g. zinc oxide or indium-tin oxide. These materials demand a rather harmful deposition process at elevated temperatures, which is incompatible with soft organic materials. Graphene combines promising electronic properties with a versatile room-temperature wet transfer process making it possible to deposit it on any desired substrate. Fig. 54 depicts the Hall measurement results of graphene on the organic hole conductors P3HT, PEDOT:PSS and Spiro-MeOTaD. These materials are commonly used in organic electronics and are therefore of particular interest. The measurements were conducted on glass (reference) and polymer-coated glass, respectively. The reference for the hexane transfer process exhibited the

highest values for the hole mobility μ_h and has already a slight p-type doping. The reference exhibits an increase in mobility and a reduction in positive charge carrier density under annealing and vacuum caused by the evaporation of adsorbates. This trend can also be observed for the samples with underlying PEDOT:PSS and P3HT, however strongly alleviated. Spiro-MeOTaD did behave different, as it was still capped. It was not possible to dissolve the support necessary for transfer without dissolving the hole conductor. More important, the presence of the organic hole conductor led to a p-type doping of the graphene as well as to a reduction of the mobility. Especially P3HT declines compared to the other materials. While the hole mobility is still at a high level, the charge carrier density limits the conductivity. Consequently, the value for the measured sheet resistance of single-layer graphene on P3HT ($R_{in\text{-}plane,\ Gr}$ = 384.6 Ω/sq.) is low. This reflects on the series resistance of the solar cell which directly impacts its output power. Power losses (P_{loss}) connected to the electrical properties of the front contact can be estimated by [170]

$$P_{loss} = (jlw)^2 R_{eff} \quad , \tag{21}$$

where $R_{eff} = r_s w/3l$. In (21) the assumption is made that the current production is approximately homogenous across a cell with the width w and the length l. The current is collected at the edge of the length l. Eq. (21) also explains the difference between EQE and the measurements under AM 1.5G-conditions. The lower light intensity of the monochromatic light for the EQE measurements reduces the current density occurring in the solar cell and therefore the electrical losses [171]. As an example one can now estimate the maximum tolerable cell width w, when limiting the fraction of power loss, $P_{loss}/(jlwV)$, to 10 %. For this estimation we take the open circuit voltage V_{OC} = 548 mV and maximum extractable current of $j_{SC,\ Max}$ = 32 mA cm^{-2} of the graphene contacted solar cell in Fig. 52. With the series resistance of r_S = 63.3 Ω cm^{-2} the cell width must be less than 0.17 cm. Similar

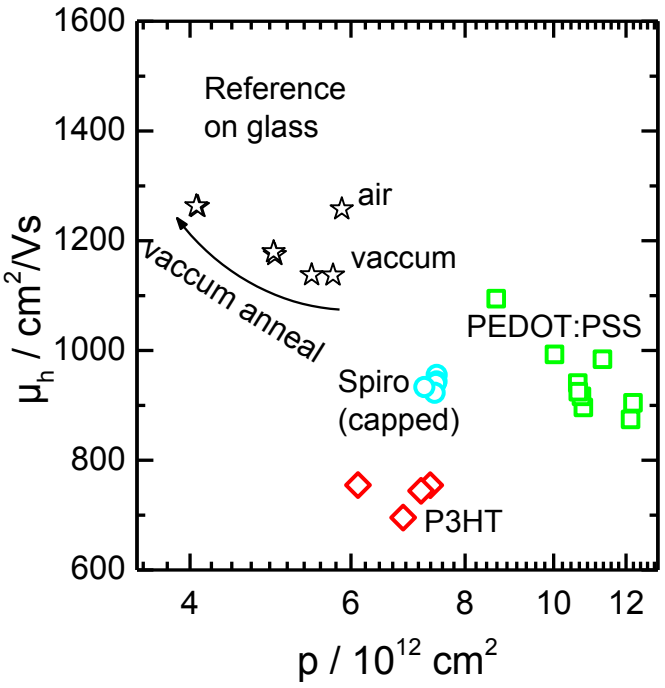

Fig. 54: Hole mobility versus charge carrier density (holes) of graphene on glass and on different underlying organic hole conductors determined by Hall measurements. Every sample was initially measured in air at room temperature and subsequently in vacuum while being annealed.

considerations led to an estimation for a maximum tolerable series resistance. Using the same values for V and j, a series resistance of $r_{S,\,Max} = 14.1\ \Omega\ cm^{-2}$ is necessary. This value translates to a maximum sheet resistance of $r_{sheet} \approx 20\ \Omega$/sq. when keeping power losses below 10 %. To reach this sheet resistance value with not intentionally doped graphene, multi-layer graphene is necessary. The actual number depends on the graphene quality, but at least 5 layers are realistic [163,172]. According to the linear dependence between absorption and layer number 11.5 % of the incident light would be lost in the graphene. Commercial Si solar cells with a similar current density typically combine emitters with a sheet resistance of 40-100 Ω/sq. [173] and Grid structures to keep losses from shadowing and r_s as low as possible. The same approach is promising for graphene. 2-3 layer graphene in combination with a grid structure matched to the electrical properties of the multilayer graphene

could significantly improve the device. The results for solar cells with a single-layer graphene front contact suggest that further optimization may lead to an alternative to ITO or ZnO, when non-destructive deposition techniques are necessary. The transfer process is compatible with soft organic materials which are commonly used and retained the open circuit voltage of $V_{OC} = 584$ mV compared to the reference design. The superior optical properties enhanced the EQE to 67.1 % on a planar substrate and the maximum extractable current reaches values of > 30 mA cm^{-2}. Due to the high current densities in typical Si solar cells, a combination of multilayer graphene and a grid structure is a promising approach to further optimize the solar cell device and making the graphene anode a relevant contact system.

8. Hybrid P3HT/polycrystalline silicon solar cells

The ultimate goal of the concept "hybrid solar cell" is a low-cost fabrication strategy by implementing organic materials without jeopardizing the efficiency potential of the inorganic material. Therefore a replacement of the cost intensive Si wafer by thin-film Si would be desirable. In this chapter, the first-time realization of such a device is presented in the combination P3HT/polycrystalline Si. The Si absorber material was prepared on glass using laser crystallization and requires a new device structure having a one-sided contact system. The resulting inverted device structure is illuminated through the glass side and reduces parasitic absorption compared to the wafer-based device design. Furthermore, the resulting device is stable and exhibits a shelf-lifetime of up to 3 month without any additional encapsulation.

8.1 Poly-Si absorber preparation and device structure

The absorber material poly-Si was prepared on commercially available Corning Eagle XG glass substrates with a size of 5×5 cm² using the following steps. After cleaning with alkaline solution (Mucasol®) an interlayer stack of 250 nm SiO_X, 80 nm SiN_X and 20 nm SiO_X was sputtered onto the glass substrates. This stack acts as diffusion barrier and anti-reflection coating (ARC) [174–176]. Then, a 10 µm thick a-Si layer was deposited using high-rate electron beam evaporation of float zone silicon at 600°C. A 5 nm thick highly phosphorous doped ($N_D \sim 10^{19}\,cm^{-3}$) a-Si layer sputtered on top of the thick a-Si layer served as dopant source during the laser crystallization process. The resulting poly-Si absorber had a final doping density of $N_D \sim 10^{16}\,cm^{-3}$. Crystallization of the complete layer stack was performed by moving a line shaped cw-laser beam across the substrate [174]. The laser had a wavelength of $\lambda_{Laser} = 808$ nm and was operated with a power density of $P_{Laser} = 2100\ W/cm^2$. Crystallization of the a-Si layer resulted in the formation of a poly-Si layer (see Fig. 55) with a preferential {100} grain orientation [177]. Prior to crystallization the samples were pre-heated to 700°C to reduce thermal stress in the glass substrate.

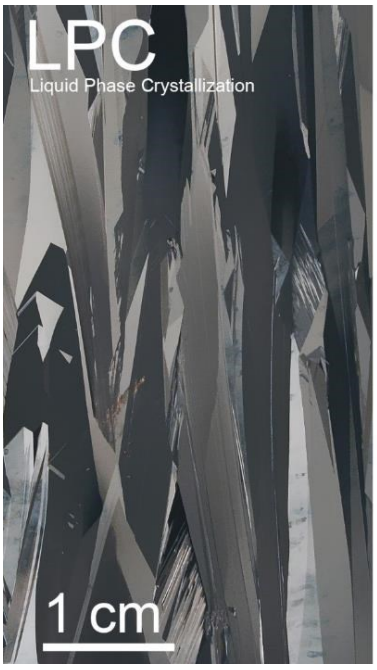

Fig. 55: Photograph of a laser crystallized poly-Si layer.

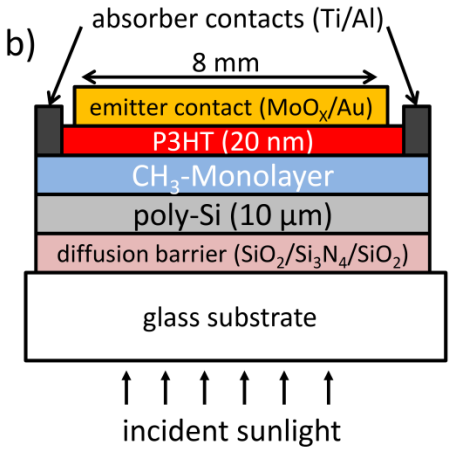

Fig. 56: Sketch of a P3HT/Poly-Si hybrid solar cell using a single-sided back contact system (illumination from glass side).

Finally, the layer stack was used to prepare the devices sketched in Fig. 56. The methyl passivation and the polymer (P3HT) were applied according to chapter 4.3. Before spin coating of the 20 nm P3HT layer as emitter, a stack of Ti/Al (20 nm/600 nm) was deposited as contact for the poly-Si absorber via a shadow mask. The MoO_X/Au (10 nm/600 nm) emitter contact was placed inside the Ti/Al absorber contact. The emitter contact defined the active area of the cell to 0.8×0.8 cm^2. The resulting staggered device structure was illuminated from the glass side. Furthermore, light trapping was implemented using an anti-reflection foil on the glass substrate that was provided by DSM Advanced Surfaces [178] to reduce reflection at the glass/air boundary.

8.2 Solar cell performance

Fig. 57 a) shows the current-voltage-characteristics with and without anti-reflection foil (ARF) of a P3HT/poly-Si hybrid solar cell as sketched in Fig. 56. A high power conversion efficiency of $\eta = 6.6$ % was achieved with an ARF. The open circuit voltage amounts to a high value of $V_{OC} = 552$ mV and the fill factor was FF = 49.8 %. The solar cell parameters are summarized in Tab. 8, including the key figures of Si wafer-based devices fabricated for comparison. The cell design of the conventional Si wafer-based devices was

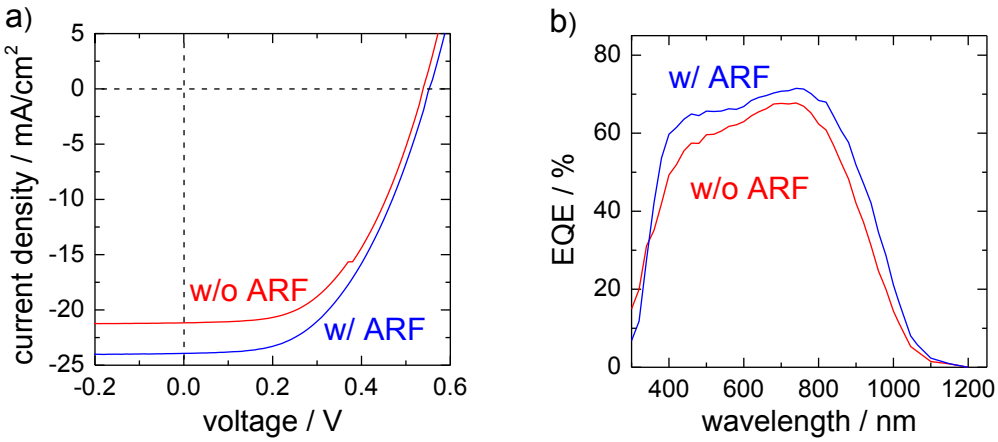

Fig. 57: a) j(V)-curves and **b)** spectral dependence of external quantum efficiencies of poly-Si thin films with and w/o anti-reflection foil (ARF).

the same as used in the chapter 5.3. The short circuit current density of the as-prepared solar cell reached a value of j_{SC} = 16 mA/cm^2 and a high open circuit voltage of V_{OC} = 617 mV was obtained. The fill factor was FF = 81.2 %, leading to a power conversion efficiency of η = 8 %. The main efficiency limiting factor is the rather low current density for a c-Si wafer-based device. State-of-the-art high efficiency c-Si solar cells reach current densities higher than 40 mA/cm^2 [179]. Most likely this is due to different optical properties. These cells are usually optimized with an anti-reflection etching in combination with an anti-reflection coating, such as a TCO at an adequate thickness to reach a minimum of reflection losses. Compared to devices which use PEDOT:PSS as emitter, the currents are also rather low. PEDOT:PSS acts as an anti-reflection layer for the absorber [180]. The front contact combination P3HT/MoO_X/Au has no pronounced anti-reflection abilities. For the inverted poly-Si solar cell the

Tab. 8: Solar cell parameter of a conventional stacked c-Si device and the inverted poly-Si thin-film devices.

Cell	V_{OC} (mV)	j_{SC} (mA/cm^2)	FF	η (%)
c-Si (conventional)	617	16.01	81.2	8.0
poly-Si (inverted)	539	21.2	52.1	5.9
poly-Si (inverted) w/ ARF	552	24.3	49.8	6.6

rather low value of the fill factor is the main efficiency limiting factor and a consequence of the used device structure. Here, the emitter contact is placed outside of the absorber and all charge carriers generated have to move from the emitter contact through the absorber resulting in a high series resistance of $R_S = 7.4\ \Omega/cm^2$ and consequently in a low fill factor. But these restrictions can be surmounted using a different contact system, e.g.: interdigitated back contacts [181]. SunsV_{OC} measurements of our cells indicated that a fill factor of up to 70.4 % will be possible for this type of back-contact solar cell with a more evolved contact scheme.

Fig. 57 b) depicts the external quantum efficiency w/ and w/o ARF. The ARF reduced the reflection at air/glass-interface. The use of the ARF lead to 4.2 % increase of the external quantum efficiency to EQE = 71.7 % at 750 nm. Additionally, a slight decrease of the EQE below 350 nm was observed due to absorption in the ARF. The high short circuit current of $j_{SC} = 24.3\ mA/cm^2$ is comparable to reported values for fully inorganic devices with a 10 µm thick poly-Si absorber [174,182] and emphasizes the good charge carrier extraction properties of the poly-Si/P3HT heterojunction. Furthermore, significant advantages result from the use of the presented inverted, rear-junction, rear contact device architecture. For a better understanding we will compare these devices to our standard wafer-based hybrid solar cell design, which is described in detail in the chapter 5.3.

8.3 Stability of Si-based hybrid solar cells

Fig. 58 a) shows the j(V)-curve of the poly-Si device in the inverted structure w/o ARF as prepared and after different times of storage in ambient air. No pronounced change in j(V) curve was observed for storage times up to three month. Fig. 58 b) depicts the same time dependence for storage in ambient air for a device utilizing our conventional stacked Si wafer-based cell design. In contrast to the inverted device design used for the P3HT/poly-Si device, the j(V) curves change drastically with time. After one the solar cell lost more than 50 % of its initial efficiency. Within a week the solar cell performance

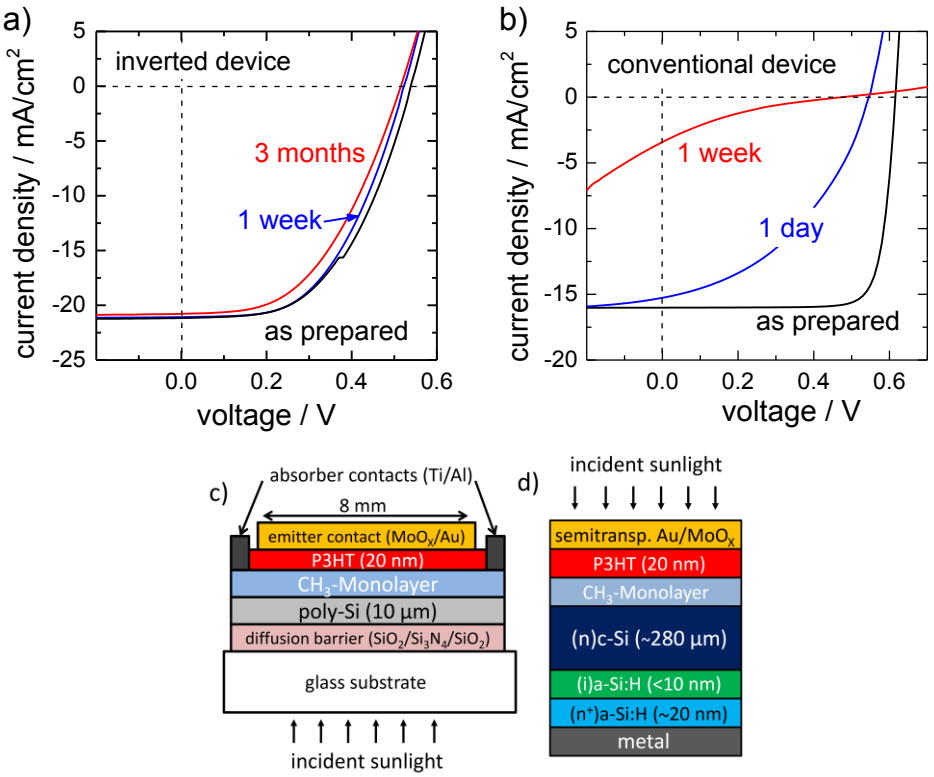

Fig. 58: j(V)-curves of the initial and the degraded devices of **a)** the inverted device structure solar cell (P3HT/poly-Si) and **b)** the conventional Si wafer based device (P3HT/c-Si). Sketch of the respective device structure in **c)** (inverted) and **d)** (conventional) for comparison.

vanished nearly completely due to degradation of the organic semiconductor P3HT.

Fig. 59 depicts the improved stability of the inverted device structure. The normalized efficiencies of the inverted poly-Si device (black squares) and the conventional-stacked Si wafer-based device (red dots) are plotted versus time. While the conventional stacked device lost almost all of its photoactive properties, the inverted device still operates at 87 % of its initial efficiency after 3 months.

In the poly-Si based solar cells, the high work-function metal Au in combination with a metal oxide successfully protects the polymer against degradation. With a thicker metal layer the device remains stable for about 3 months without any additional encapsulation. However, the thin metal layer

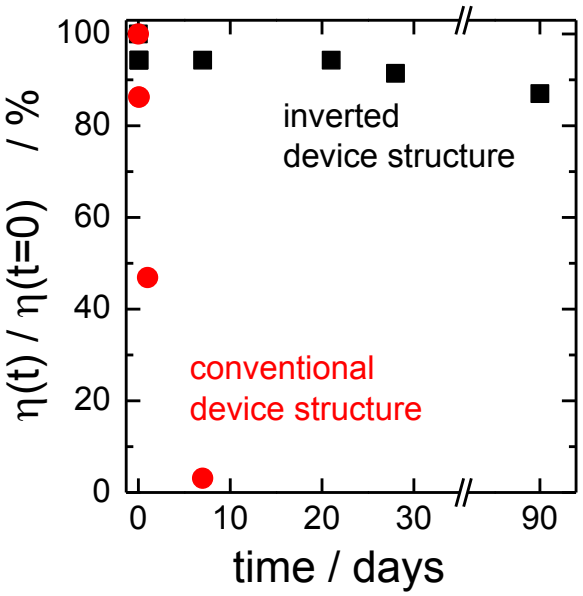

Fig. 59 : Time dependence of the normalized efficiency of Si wafer-based (red circles) and the inverted structure of the poly-Si thin-film hybrid solar cells (black squares). The devices were stored in ambient air between measurements.

used in the conventional stacked device is not able to protect the polymer from photo-oxidation. In combination with the stable, covalently bond methyl groups, improved device stability is achieved, which is inherent to the inverted device structure. At this point, it has to be noted that other processes related to the hygroscopic and acidic properties of PEDOT:PSS [183,184] and chemical degradation of the metal electrode [185], which can cause a significant degradation of solar cells, are avoided by the use of P3HT.

Additionally to the increased device stability, the inverted device structure circumvents the parasitic absorption resulting from a metal front contact.

9. Conclusion

The objective of this thesis was the fabrication and examination of hybrid solar cells based on silicon absorber in combination with a thin polymer layer. Intrinsic material aspects as well as fundamental device characteristics comprising this type of junction were explored towards a basic understanding of these photovoltaic devices.

Characterization of organic polymer materials

Different poly-thiophene materials were used in this thesis, namely, poly(3-hexylthiophene-2,5-diyl) and its two derivatives poly(3-[3,6-dioxaheptyl]-thiophene) and poly(3-[2,5,8-trioxanonyl]-thiophene) with two and three ether groups in the side chains, respectively. The hydrophilic side chains used in the derivatives lead to thinner and more homogeneous films when spin coated on SiO_X covered Si surface. Furthermore, the crystallinity of the solution processed polymers is increased for P3TOT as measured by XRD. The crystallite size was determined to 19, 6, and 6 nm for P3TOT, P3DOT, and P3HT, respectively. Additionally, a twist in the polymer backbone caused by a steric hindrance of the oxygen atoms in the side chains was identified for P3TOT.

The use of these polymers in hybrid solar cells led to an increase in efficiency from below 4 % to 9.6 % with the increasing number of oxygen atoms in the side chains. Shunting of the polymer layer was established as the restricting factor for P3HT. The higher crystallinity led to more rigid polymer layers for P3DOT and P3TOT that successfully prevented the diffusion of the evaporated gold top contact towards the interface. Consequently, Fermi level pinning in the silicon was avoided. These results were confirmed by introducing a molybdenum oxide buffer layer between the polymer and the gold. The MoO_X layer prevented shunting even for the P3HT layer on Si, which finally led to an power conversion efficiency close to that of the P3TOT/n-Si device. Furthermore, the anode buffer layer improved reproducibility and the cell size could be increased to 1 cm^2.

Analysis of Si wafer-based solar cells

After the realization of a stable solar cell fabrication process with an average efficiency of $\eta \sim 10$ % (the highest η was 11 %), investigations regarding the underlying working principles of this device type were performed. For this reason, the hybrid solar cells were compared to its inorganic counterpart, the a-Si:H/c-Si heterojunction. Measuring the external quantum efficiencies an advantage regarding charge carrier generation in the short wavelength region was revealed. Surprisingly, the formation of an inversion layer beneath the silicon surface was observed. This inversion layer strongly reduced the influence of the silicon interface passivation. UPS/XPS measurements were used to quantify the band bending in silicon covered with the polymer layers. The slight band bending of 0.1…0.2 eV is in accordance with a small field effect passivation and indicates a similar behavior as expected for fixed surface charges deposited on silicon. Furthermore, the measurements exhibited similarities to a polymer/metal interface. Additionally, surface photovoltage measurements determined that the main fraction of the silicon band bending is caused by the front contact combination MoO_X/Au. Similar to a Schottky solar cell, inversion occurs in the device when the metal is applied. Moreover, the organic layer takes the function of an electron blocking layer and additionally protects the silicon from defect formation. An ideal p/n-junction is formed below the silicon surface and the influence of the surface defects is reduced.

Even so, the semitransparent gold contact used for the c-Si based hybrid solar cells absorbs too much light, limits power conversion efficiency and therefore should be replaced. One attempt that has been carried out in this work is the implementation of graphene as a transparent front contact on the polymer layer of the Si wafer-based hybrid solar cells. The carbon monolayer absorbs only 2.7 % of the incident light and has excellent electronic properties. The CVD grown graphene sheet with a lateral size of 1 cm^2 and was transferred on top of the solar cell using a non-destructive and water-free transfer process. The remaining high graphene quality after transfer was verified by Raman spectroscopy, while the same open circuit voltage as the

reference with the gold contact on the same substrate proved the non-destructive transfer process. However, the power conversion efficiency was restricted by the low fill factor due to a low charge-carrier density in the graphene. A calculation based on the electrical losses indicated that the problem could be overcome by a combination of multilayer graphene and an additional metal grid structure to increase conductivity.

Inverted polycrystalline Si/P3HT hybrid solar cells

Nevertheless, thicker gold layers as a contact system have been used in the inverted device structure as applied for the hybrid solar cells made from thin-film polycrystalline silicon absorbers on glass.

These devices were illuminated from the glass side and had emitter and absorber contacts on the backside. This contact concept allowed for the use of thicker metal contacts. The inverted device structure had a number of advantages: (i) the parasitic absorption in the gold was circumvented, (ii) the polymer was successfully protected from photo-oxidation and (iii) the device stability increased strongly (more than three months without additional encapsulation). A power conversion efficiency of 6.6 % was obtained for this new type of hybrid solar cell.

Appendix: Calculating the dark band bending in SPV-measurements

The calculation of the dark band bending $\Delta\varphi_0$ from the SPV-signal $\Delta\varphi_{SPV}$ follows the considerations of Heilig et al. [67]. The measurement principle is based on the physical effect of a reduction of the surface band bending due to generation of additional charge carriers under illumination. For the calculation, two basic prerequisites have to be satisfied. The initial charge carrier density Δn_{Laser} after excitation has to be known. The surface charges Q_S creating the band bending have to be constant for the duration of the laser pulse. Starting from the equation for the charge carrier density in the space charge region (SCR) before and after illumination, it follows:

$$Q_{SCR}(\Delta n = 0, \Delta p, \Delta\varphi_0) = Q_{SCR}\left(\Delta n_{Laser}, \Delta p, \Delta\varphi_{0,ill}\right) \quad , \tag{21}$$

with

$$Q_{SCR}(\Delta n, \Delta p, \Delta\varphi) = \mathrm{sign}(\varphi)\sqrt{2\frac{\varepsilon_0\varepsilon_r}{q^2}} \cdot F(\Delta n, \Delta p, \Delta\varphi) \quad , \tag{22}$$

and

$$F(\Delta n, \Delta p, \Delta\varphi) = \sqrt{\varphi(N_A - N_D) + k_B T((p_0 + \Delta p)\left(e^{\frac{\varphi}{k_B T}} - 1\right) + (n_0 + \Delta n)\left(e^{\frac{\varphi}{k_B T}} - 1\right))} \tag{23}$$

Δn and Δp term the electron and hole excess carrier density, respectively. $\Delta\varphi_{0,ill}$is the remaining band bending in Si under illumination and is 0 for flat band conditions. ε_0 and ε_r are the vacuum permittivity and relative dielectric constant. N_A and N_D are the acceptor and donor dopant concentration, k_B the

Boltzmann constant, T the temperature, and n_0 and p_0 the equilibrium bulk hole concentrations.

Assuming that $\Delta n = \Delta p$, the band bending in Si can be calculated as following:

$$\Delta\varphi_0 = -k_B T \cdot \ln\left(a - sign\left(\Delta\varphi_{SPV}\right)\sqrt{a^2 + 2b^2}\right) \quad , \tag{24}$$

with

$$\mathrm{a} = \frac{1}{c}\left(\left(\frac{1}{\lambda} - \lambda\right)\frac{\Delta\varphi_{SPV}}{k_B T} + \frac{2\Delta n}{n_i}\right) \quad , \tag{25}$$

$$\mathrm{b} = \frac{1}{c}\left(\lambda - \left(\lambda + \frac{\Delta n}{n_i}\right)e^{-\frac{\Delta\varphi_{SPV}}{k_B T}}\right) \quad , \tag{26}$$

$$\mathrm{c} = 2\left(\left(\frac{1}{\lambda} + \frac{\Delta n}{n_i}\right)e^{-\frac{\Delta\varphi_{SPV}}{k_B T}} - \frac{1}{\lambda}\right) \quad , \tag{27}$$

$$\lambda = \frac{n_i}{n_0} \quad . \tag{28}$$

n_i is the intrinsic charge carrier density in c-Si. The measured SPV signal has to be corrected for the Dember voltage $\Delta\varphi_{\mathrm{Dember}}$ according to $\Delta\varphi_{\mathrm{SPV}} = \Delta\varphi_0 + \Delta\varphi_{\mathrm{Dember}}$. The Dember voltage is given by:

$$\Delta\varphi_{Dember} = \frac{k_B T}{e}\frac{b-1}{b+1} ln\left(1 + \Delta n \frac{b+1}{n_0 b + p_0}\right) \tag{29}$$

with $\mathrm{b} = \frac{\mu_n}{\mu_p}$ is the ratio between electron and hole mobility values [157].

For the setup used, $\Delta n_{\mathrm{Laser}}$ was estimated to $10^{17}\mathrm{cm}^{-3}$ [156]. Errors on $\Delta n_{\mathrm{Laser}}$ are unknown. In any case variations between samples with different surface properties, e.g. parasitic absorption and difference in reflectivity, will lead to change in $\Delta n_{\mathrm{Laser}}$.

Bibliography

[1] G. Hodes, Science **342**, 317 (2013).

[2] P.J. Hagrman, D. Hagrman, and J. Zubieta, Angew. Chemie Int. Ed. **38**, 2638 (1999).

[3] F. Yang, K. Roodenko, R. Hunger, K. Hinrichs, K. Rademann, and J. Rappich, J. Phys. Chem. C **116**, 18684 (2012).

[4] T. Shimoda, Y. Matsuki, M. Furusawa, T. Aoki, I. Yudasaka, H. Tanaka, H. Iwasawa, D. Wang, M. Miyasaka, and Y. Takeuchi, Nature **440**, 783 (2006).

[5] T. Masuda, N. Sotani, H. Hamada, Y. Matsuki, and T. Shimoda, Appl. Phys. Lett. **100**, 253908 (2012).

[6] T. Bronger, P.H. Wöbkenberg, J. Wördenweber, S. Muthmann, U.W. Paetzold, V. Smirnov, S. Traut, Ü. Dagkaldiran, S. Wieber, M. Cölle, A. Prodi-Schwab, O. Wunnicke, M. Patz, M. Trocha, U. Rau, and R. Carius, Adv. Energy Mater. **4**, (2014).

[7] M.A. Green, K. Emery, Y. Hishikawa, W. Warta, and E.D. Dunlop, Prog. Photovoltaics Res. Appl. **23**, 805 (2015).

[8] N.C. Giebink, G.P. Wiederrecht, M.R. Wasielewski, and S.R. Forrest, Phys. Rev. B - Condens. Matter Mater. Phys. **83**, 1 (2011).

[9] M.J. Sailor, E.J. Ginsburg, C.B. Gorman, A. Kumar, R.H. Grubbs, and N.S. Lewis, Science **249**, 1146 (1990).

[10] L. Tsakalakos, J. Balch, J. Fronheiser, B.A. Korevaar, O. Sulima, and J. Rand, Appl. Phys. Lett. **91**, 233117 (2007).

[11] J.R. Maiolo, B.M. Kayes, M. A. Filler, M.C. Putnam, M.D. Kelzenberg, H. A. Atwater, and N.S. Lewis, J. Am. Chem. Soc. **129**, 12346 (2007).

[12] V. Gowrishankar, S.R. Scully, M.D. McGehee, Q. Wang, and H.M. Branz, Appl. Phys. Lett. **89**, 2006 (2006).

[13] W. Wang and E. A. Schiff, Appl. Phys. Lett. **91**, 133504 (2007).

[14] S. Avasthi, S. Lee, Y.-L. Loo, and J.C. Sturm, Adv. Mater. **23**, 5762 (2011).

[15] S. Jäckle, M. Mattiza, M. Liebhaber, G. Brönstrup, M. Rommel, K. Lips, and S. Christiansen, Sci. Rep. **5**, 13008 (2015).

[16] S.-C. Shiu, J.-J. Chao, S.-C. Hung, C.-L. Yeh, and C.-F. Lin, Chem. Mater. **22**, 3108 (2010).

[17] S. Jeong, E.C. Garnett, S. Wang, Z. Yu, S. Fan, M.L. Brongersma, M.D. McGehee, and Y. Cui, Nano Lett. **12**, 2971 (2012).

[18] Y. Zhang, F. Zu, S.-T. Lee, L. Liao, N. Zhao, and B. Sun, Adv. Energy Mater. **4**, (2014).

[19] R. Liu, S.-T. Lee, and B. Sun, Adv. Mater. **26**, 6007 (2014).

[20] M. Pietsch, S. Jäckle, and S. Christiansen, Appl. Phys. A **115**, 1109 (2014).

[21] S. Garreau, J.L. Duvail, and G. Louarn, Synth. Met. **125**, 325 (2002).

[22] S. Kirchmeyer and K. Reuter, J. Mater. Chem. **15**, 2077 (2005).

[23] S.M. Sze, *Physics of Semiconductor Devices*, 2nd Editio (John Wiley & Sons, 1981).

[24] J. Nelson, *The Physics of Solar Cells* (Imperial College Press, 2003).

[25] J.C. Slater and G.F. Koster, Phys. Rev. **94**, 1498 (1954).

[26] ITRPV, *International Technology Roadmap for Photovoltaic (ITRPV)* (2015).

[27] W. Shockley and H.J. Queisser, J. Appl. Phys. **32**, 510 (1961).

[28] J.R. Chelikowsky and M.L. Cohen, Phys. Rev. B **10**, 5095 (1974).

[29] W. Warta and N. Karl, Phys. Rev. B **32**, 1172 (1985).

[30] K. Hannewald, V.M. Stojanović, J.M.T. Schellekens, P.A. Bobbert, G. Kresse, and J. Hafner, Phys. Rev. B **69**, 75211 (2004).

[31] N. Sato, H. Inokuchi, and E.A. Silinsh, Chem. Phys. **115**, 269 (1987).

[32] D. Bimberg, I. Eisele, W. Fuhs, H. Kahlert, and N. Karl, *Landolt-Börnstein Numerical Data and Functional Relationships in Science and Technology* (Springer-Verlag Berlin, 1985).

[33] M.A. Green, AIP Adv. **3**, 112104 (2013).

[34] B. Schweitzer and H. Bässler, Synth. Met. **109**, 1 (2000).

[35] E.P. Donovan, F. Spaepen, D. Turnbull, J.M. Poate, and D.C. Jacobson, Appl. Phys. Lett. **42**, 698 (1983).

[36] O. Renner and J. Zemek, Czechoslov. J. Phys. **23**, 1273 (1973).

[37] M. Schwoerer and H.C. Wolf, *Organische Molekulare Festkörper* (WILEY-VCH, 2005).

[38] P.W. Atkins and J. de Paula, *Physikalische Chemie*, 4th ed. (WILEY-VCH, Weinheim, 2006).

[39] A. Tsumura, H. Koezuka, and T. Ando, Appl. Phys. Lett. **49**, 1210 (1986).

[40] M. Granström and O. Inganäs, Appl. Phys. Lett. **68**, 147 (1996).

[41] Y. Kim, S. Cook, S.M. Tuladhar, S. A. Choulis, J. Nelson, J.R. Durrant, D.D.C. Bradley, M. Giles, I. McCulloch, C.-S. Ha, and M. Ree, Nat. Mater. **5**, 197 (2006).

[42] D.M. DeLongchamp, B.M. Vogel, Y. Jung, M.C. Gurau, C.A. Richter, O. A. Kirillov, J. Obrzut, D.A. Fischer, S. Sambasivan, L.J. Richter, and E.K. Lin, Chem. Mater. **17**, 5610 (2005).

[43] R.J. Kline, M.D. McGehee, E.N. Kadnikova, J. Liu, J.M.J. Fréchet, and M.F. Toney, Macromolecules **38**, 3312 (2005).

[44] J. Chang, B. Sun, D.W. Breiby, M.M. Nielsen, T.I. Sölling, M. Giles, I. McCulloch, and H. Sirringhaus, Chem. Mater. **16**, 4772 (2004).

[45] K. Tashiro, K. Ono, Y. Minagawa, M. Kobayashi, T. Kawai, and K. Yoshino, J. Polym. Sci. Part B Polym. Phys. **29**, 1223 (1991).

[46] T.J. Prosa, M.J. Winokur, J. Moulton, P. Smith, and A.J. Heeger, Macromolecules **25**, 4364 (1992).

[47] R. Zhang, B. Li, M.C. Iovu, M. Jeffries-El, G. Sauvé, J. Cooper, S. Jia, S. Tristram-Nagle, D.M. Smilgies, D.N. Lambeth, R.D. McCullough, and T. Kowalewski, J. Am. Chem. Soc. **128**, 3480 (2006).

[48] A. Zen, M. Saphiannikova, and D. Neher, Macromolecules **39**, 2162 (2006).

[49] C.J. Takacs, N.D. Treat, S. Krämer, Z. Chen, A. Facchetti, M.L. Chabinyc, and A.J. Heeger, Nano Lett. **13**, 2522 (2013).

[50] R. Noriega, J. Rivnay, K. Vandewal, F.P. V Koch, N. Stingelin, P. Smith, M.F. Toney, and A. Salleo, Nat. Mater. **12**, 1038 (2013).

[51] A. Kohler and H. Bässler, *Electronic Processes in Organic Semiconductors: An Introduction* (WILEY-VCH, Weinheim, 2015).

[52] W. Schnabel, *Polymers and Electromagnetic Radiation*, Weinheim (WILEY-VCH, 2014).

[53] R.Q. Albuquerque, C.C. Hofmann, J. Köhler, and A. Köhler, J. Phys. Chem. B **115**, 8063 (2011).

[54] W.W. Parson, *Modern Optical Spectroscopy* (Springer Berlin Heidelberg, Berlin, Heidelberg, 2007).

[55] P. Brown, D. Thomas, A. Köhler, J. Wilson, J.-S. Kim, C. Ramsdale, H. Sirringhaus, and R. Friend, Phys. Rev. B **67**, 1 (2003).

[56] H. Yang, S.W. Lefevre, C.Y. Ryu, and Z. Bao, Appl. Phys. Lett. **90**, 28 (2007).

[57] O. Inganäs, W.. Salaneck, J.-E. Österholm, and J. Laakso, Synth. Met. **22**, 395 (1988).

[58] T. Dittrich, *Materials Concepts For Solar Cells* (Imperial College Press, 2015).

[59] R. Stangl, M. Kriegel, K. V. Maydell, L. Korte, M. Schmidt, and W. Fuhs, Conf. Rec. IEEE Photovolt. Spec. Conf. 1556 (2005).

[60] K. Masuko, M. Shigematsu, T. Hashiguchi, D. Fujishima, M. Kai, N. Yoshimura, T. Yamaguchi, Y. Ichihashi, T. Mishima, N. Matsubara, T. Yamanishi, T. Takahama, M. Taguchi, E. Maruyama, and S. Okamoto, IEEE J. Photovoltaics **4**, 1433 (2014).

[61] M.J. Kerr, A. Cuevas, and P. Campbell, Prog. Photovoltaics Res. Appl. **11**, 97 (2003).

[62] K. V. Maydell, L. Korte, A. Laades, R. Stangl, E. Conrad, F. Lange, and M. Schmidt, J. Non-Cryst. Sol. **352**, 1958 (2006).

[63] A. Descoeudres, L. Barraud, S. De Wolf, B. Strahm, D. Lachenal, C. Guérin, Z.C. Holman, F. Zicarelli, B. Demaurex, J. Seif, J. Holovsky, and C. Ballif, Appl. Phys. Lett. **99**, 128 (2011).

[64] M. Mews, T.F. Schulze, N. Mingirulli, and L. Korte, Energy Procedia **38**, 855 (2013).

[65] M. Reusch, M. Bivour, M. Hermle, and S.W. Glunz, Energy Procedia **38**, 297 (2013).

[66] Y.W. Lam, J. Phys. D. Appl. Phys. **4**, 1370 (1971).

[67] K. Heilig, Surf. Sci. **44**, 421 (1974).

[68] T.F. Schulze, L. Korte, F. Ruske, and B. Rech, Phys. Rev. B **83**, 165314 (2011).

[69] L. Korte, A. Laades, K. Lauer, R. Stangl, D. Schaffarzik, and M. Schmidt, Thin Solid Films **517**, 6396 (2009).

[70] H. Dember, Phys. Zeitschrift **33**, 207 (1932).

[71] W.H. Bragg and W.L. Bragg, Proc. R. Soc. A Math. Phys. Eng. Sci. **88**, 428 (1913).

[72] P. Scherrer, Nachr. Ges. Wiss. Göttingen **2**, 98 (1918).

[73] U. Holzwarth and N. Gibson, Nat. Nanotechnol. **6**, 534 (2011).

[74] H. Hertz, Ann. Der Phys. Und Chemie **267**, 983 (1887).

[75] A. Einstein, Ann. Phys. **4**, 132 (1905).

[76] W.E. Spicer, Phys. Rev. **112**, 114 (1958).

[77] E.O. Kane, Phys. Rev. **159**, 624 (1967).

[78] E.O. Kane, Phys. Rev. **147**, 335 (1966).

[79] M.P. Seah and W.A. Dench, Surf. Interface Anal. **1**, 2 (1979).

[80] D. Lin-Vien, N.B. Colthup, W.G. Fateley, and J.G. Grasselli, *The Handbook of Infrared and Raman Characteristic Frequencies of Organic Molecules* (Academic Press, London, 1991).

[81] W. Kern, J. Electrochem. Soc. **137**, 1887 (1990).

[82] H. Angermann, T. Dittrich, and H. Flietner, Appl. Phys. A **197**, 193 (1994).

[83] T. Dittrich, *Materials Concepts For Solar Cells*, 1st ed. (Imperial College Press, 2015).

[84] L. Korte and M. Schmidt, J. Non. Cryst. Solids **354**, 2138 (2008).

[85] D. Meyerhofer, J. Appl. Phys. **49**, 3993 (1978).

[86] D.B. Hall, P. Underhill, and J.M. Torkelson, Polym. Eng. Sci. **38**, 2039 (1998).

[87] R. Williams and A.M. Goodman, Appl. Phys. Lett. **25**, 531 (1974).

[88] D. Janssen, R. De Palma, S. Verlaak, P. Heremans, and W. Dehaen, Thin Solid Films **515**, 1433 (2006).

[89] T. Hori, T. Shibata, V. Kittichungchit, H. Moritou, J. Sakai, H. Kubo, A. Fujii, and M. Ozaki, Thin Solid Films **518**, 522 (2009).

[90] V. Shrotriya, G. Li, Y. Yao, C.-W. Chu, and Y. Yang, Appl. Phys. Lett. **88**, 73508 (2006).

[91] Y.-C. Tseng, A.U. Mane, J.W. Elam, and S.B. Darling, Sol. Energy Mater. Sol. Cells **99**, 235 (2012).

[92] F.S. Freitas, R.B. Merlo, F.C. Marques, and A.F. Nogueira, Phys. Status Solidi **211**, 2657 (2014).

[93] A.G. Aberle, Prog. Photovoltaics Res. Appl. **8**, 473 (2000).

[94] C.J. Brabec, A. Cravino, D. Meissner, N.S. Sariciftci, T. Fromherz, M.T. Rispens, L. Sanchez, and J.C. Hummelen, Adv. Funct. Mater. **11**, 374 (2001).

[95] M. Mews, M. Liebhaber, B. Rech, and L. Korte, Appl. Phys. Lett. **107**,

(2015).

[96] L. Dou, J. You, J. Yang, C.-C. Chen, Y. He, S. Murase, T. Moriarty, K. Emery, G. Li, and Y. Yang, Nat. Photonics **6**, 180 (2012).

[97] M. Brendel, S. Krause, A. Steindamm, A.K. Topczak, S. Sundarraj, P. Erk, S. Höhla, N. Fruehauf, N. Koch, and J. Pflaum, Adv. Funct. Mater. **25**, 1565 (2015).

[98] T. Bilkay, K. Schulze, T. Egorov-Brening, A. Bohn, and S. Janietz, Macromol. Chem. Phys. **213**, 1970 (2012).

[99] S. Pankaj, E. Hempel, and M. Beiner, Macromolecules **42**, 716 (2009).

[100] DFT calculations were conducted by Prof. N.H. Nickel

[101] J. Paloheimo, H. Stubb, P. Yli-Lahti, and P. Kuivalainen, Synth. Met. **41**, 563 (1991).

[102] M.C. Stefan, A.E. Javier, I. Osaka, and R.D. McCullough, Macromolecules **42**, 30 (2009).

[103] R.J. Kline, M.D. McGehee, E.N. Kadnikova, J. Liu, and J.M.J. Fréchet, Adv. Mater. **15**, 1519 (2003).

[104] C. Yang, F.P. Orfino, and S. Holdcroft, Macromolecules **29**, 6510 (1996).

[105] H.J. Fell, E.J. Samuelsen, J. Als-Nielsen, G. Grübel, and J. Mårdalen, Solid State Commun. **94**, 843 (1995).

[106] H. Meier, U. Stalmach, and H. Kolshorn, Acta Polym. **48**, 379 (1997).

[107] W.R. Salaneck, O. Inganäs, B. Thémans, J.O. Nilsson, B. Sjögren, J.-E. Österholm, J.L. Brédas, and S. Svensson, J. Chem. Phys. **89**, 4613 (1988).

[108] D. Neher, Adv. Mater. **7**, 691 (1995).

[109] N.H. Nickel, M.A. Gluba, and J. Rappich, Subbmitted Publ. (n.d.).

[110] J.P. Ponpon and P. Siffert, J. Appl. Phys. **47**, 3248 (1976).

[111] D.R. Lillington and W.G. Townsend, Appl. Phys. Lett. **28**, 97 (1976).

[112] S.J. Fonash, J. Appl. Phys. **46**, 1286 (1975).

[113] W. Shin, J. Lee, J.C. Kim, T. Yoon, T. Kim, and O. Song, Org. Electron. **9**, 333 (2008).

[114] H. You, Y. Dai, Z. Zhang, and D. Ma, J. Appl. Phys. **101**, 2005 (2007).

[115] F. Liu, S. Shao, X. Guo, Y. Zhao, and Z. Xie, Sol. Energy Mater. Sol. Cells **94**, 842 (2010).

[116] Y. Sun, C.J. Takacs, S.R. Cowan, J.H. Seo, X. Gong, A. Roy, and A.J. Heeger, Adv. Mater. **23**, 2226 (2011).

[117] S. Jäckle, M. Mattiza, M. Liebhaber, G. Brönstrup, M. Rommel, K. Lips, and S. Christiansen, Sci. Rep. **5**, 13008 (2015).

[118] C.W. Tang, Appl. Phys. Lett. **48**, 183 (1986).

[119] M. Riede, T. Mueller, W. Tress, R. Schueppel, and K. Leo, Nanotechnology **19**, 424001 (2008).

[120] A. Wilke, J. Endres, U. Hörmann, J. Ziederhausen, R. Schlesinger, J. Frisch, P. Amsalem, J. Wagner, M. Gruber, A. Opitz, A. Vollmer, W. Brütting, A. Kahn, and N. Koch, Appl. Phys. Lett. **101**, 233301 (2012).

[121] K. Vandewal, A. Gadisa, W.D. Oosterbaan, S. Bertho, F. Banishoeib, I. Van Severen, L. Lutsen, T.J. Cleij, D. Vanderzande, and J. V. Manca, Adv. Funct. Mater. **18**, 2064 (2008).

[122] E. Yablonovitch, D.L. Allara, C.C. Chang, T. Gmitter, and T.B. Bright,

Phys. Rev. Lett. **57**, 249 (1986).

[123] M.J. Kerr, J. Schmidt, A. Cuevas, and J.H. Bultman, J. Appl. Phys. **89**, 3821 (2001).

[124] M. Liebhaber, M. Mews, T.F. Schulze, L. Korte, B. Rech, and K. Lips, Appl. Phys. Lett. **106**, 31601 (2015).

[125] L. Korte, E. Conrad, H. Angermann, R. Stangl, and M. Schmidt, Sol. Energy Mater. Sol. Cells **93**, 905 (2009).

[126] A.S. Erickson, A. Zohar, and D. Cahen, Adv. Energy Mater. **4**, 1 (2014).

[127] J. Sheng, K. Fan, D. Wang, C. Han, J. Fang, P. Gao, and J. Ye, ACS Appl. Mater. Interfaces **6**, 16027 (2014).

[128] F. Zhang, D. Liu, Y. Zhang, H. Wei, T. Song, and B. Sun, ACS Appl. Mater. Interfaces **5**, 4678 (2013).

[129] H. Fujiwara and M. Kondo, J. Appl. Phys. **101**, 1 (2007).

[130] Z.C. Holman, A. Descoeudres, L. Barraud, F.Z. Fernandez, J.P. Seif, S. De Wolf, and C. Ballif, IEEE J. Photovoltaics **2**, 7 (2012).

[131] P.Y. Yu and M. Cardona, *Fundamentals of Semiconductors: Physics and Material Properties*, 3rd ed. (Springer, 2005).

[132] C. Leendertz, N. Mingirulli, T.F. Schulze, J.P. Kleider, B. Rech, and L. Korte, Appl. Phys. Lett. **98**, 10 (2011).

[133] W. Osikowicz, M.P. de Jong, S. Braun, C. Tengstedt, M. Fahlman, and W.R. Salaneck, Appl. Phys. Lett. **88**, 193504 (2006).

[134] Y. Sohn and J.T. Stuckless, Appl. Phys. Lett. **90**, 171901 (2007).

[135] C. Tengstedt, W. Osikowicz, W.R. Salaneck, I.D. Parker, C.-H. Hsu, and M.

Fahlman, Appl. Phys. Lett. **88**, 53502 (2006).

[136] M. Fahlman, A. Crispin, X. Crispin, S.K.M. Henze, M.P. de Jong, W. Osikowicz, C. Tengstedt, and W.R. Salaneck, J. Phys. Condens. Matter **19**, 183202 (2007).

[137] M.J. Price, J.M. Foley, R. A. May, and S. Maldonado, Appl. Phys. Lett. **97**, 10 (2010).

[138] Y. Zhu, T. Song, F. Zhang, S.-T. Lee, and B. Sun, Appl. Phys. Lett. **102**, 113504 (2013).

[139] M. Sailor, E. Ginsburg, and C. Gorman, Sci. (New York, **63**, (1990).

[140] R. Har-Lavan and D. Cahen, IEEE J. Photovoltaics **3**, 1443 (2013).

[141] W.R. Salaneck, O. Inganäs, B. Thémans, J.O. Nilsson, B. Sjögren, J.-E. Österholm, J.L. Brédas, and S. Svensson, J. Chem. Phys. **89**, 4613 (1988).

[142] P. Dannetun, M. Boman, S. Stafström, W.R. Salaneck, R. Lazzaroni, C. Fredriksson, J.L. Brédas, R. Zamboni, and C. Taliani, J. Chem. Phys. **99**, 664 (1993).

[143] J.E. Lyon, A. J. Cascio, M.M. Beerbom, R. Schlaf, Y. Zhu, and S. A. Jenekhe, Appl. Phys. Lett. **88**, 1 (2006).

[144] S. Braun, W.R. Salaneck, and M. Fahlman, Adv. Mater. **21**, 1450 (2009).

[145] N. Koch, A. Elschner, J.P. Rabe, and R.L. Johnson, Adv. Mater. **17**, 330 (2005).

[146] S. Duhm, G. Heimel, I. Salzmann, H. Glowatzki, R.L. Johnson, A. Vollmer, J.P. Rabe, and N. Koch, Nat. Mater. **7**, 326 (2008).

[147] I. Jiménez and J.L. Sacedón, Surf. Sci. **482–485**, 272 (2001).

[148] F. Himpsel, F. McFeely, A. Taleb-Ibrahimi, J. Yarmoff, and G. Hollinger, Phys. Rev. B **38**, 6084 (1988).

[149] S.W. Glunz, D. Biro, S. Rein, and W. Warta, J. Appl. Phys. **86**, 683 (1999).

[150] E. Yablonovitch, B.J. Skromme, R. Bhat, J.P. Harbison, and T.J. Gmitter, Appl. Phys. Lett. **54**, 555 (1989).

[151] M. A. Green, Appl. Phys. Lett. **33**, 178 (1978).

[152] P.J. Caplan, E.H. Poindexter, B.E. Deal, and R.R. Razouk, J. Appl. Phys. **50**, 5847 (1979).

[153] S.K. Lai, J. Appl. Phys. **54**, 2540 (1983).

[154] J. Ziegler, M. Mews, K. Kaufmann, T. Schneider, A.N. Sprafke, L. Korte, and R.B. Wehrspohn, Appl. Phys. A 2 (2015).

[155] H. Kuchling, *Taschenbuch Der Physik*, 11th ed. (Hanser Verlag, 1988).

[156] C. Leendertz, Effizienzlimitierende Rekombinationsprozesse in Amorph/kristallinen Und Polykristallinen Siliziumsolarzellen, 2012.

[157] P.Würfel, Physik Der Solarzellen, Springer, 1995.

[158] K.S. Novoselov, Rev. Mod. Phys. **83**, 837 (2011).

[159] A.S. Mayorov, R. V. Gorbachev, S. V. Morozov, L. Britnell, R. Jalil, L. A. Ponomarenko, P. Blake, K.S. Novoselov, K. Watanabe, T. Taniguchi, and A. K. Geim, Nano Lett. **11**, 2396 (2011).

[160] A. Balandin, Nat. Mater. **10**, 569 (2011).

[161] R.R. Nair, P. Blake, A.N. Grigorenko, K.S. Novoselov, T.J. Booth, T. Stauber, N.M.R. Peres, and a K. Geim, Science (80-.). **320**, 1308 (2008).

[162] F. Lang, M. A. Gluba, S. Albrecht, J. Rappich, L. Korte, B. Rech, and N.H.

Nickel, J. Phys. Chem. Lett. **6**, 2745 (2015).

[163] Y. Wang, S.W. Tong, X.F. Xu, B. Özyilmaz, and K.P. Loh, Adv. Mater. **23**, 1514 (2011).

[164] T. Ohta, A. Bostwick, J.L. McChesney, T. Seyller, K. Horn, and E. Rotenberg, Phys. Rev. Lett. **98**, 206802 (2007).

[165] P.H. Tan, W.P. Han, W.J. Zhao, Z.H. Wu, K. Chang, H. Wang, Y.F. Wang, N. Bonini, N. Marzari, N. Pugno, G. Savini, A. Lombardo, and A.C. Ferrari, Nat. Mater. **11**, 294 (2012).

[166] P. Zhao, A. Kumamoto, S. Kim, X. Chen, B. Hou, S. Chiashi, E. Einarsson, Y. Ikuhara, and S. Maruyama, J. Phys. Chem. C **117**, 130416213951007 (2013).

[167] A. Eckmann, A. Felten, I. Verzhbitskiy, R. Davey, and C. Casiraghi, Phys. Rev. B **88**, 35426 (2013).

[168] Q. Hao, S.M. Morton, B. Wang, Y. Zhao, L. Jensen, and T. Jun Huang, Appl. Phys. Lett. **102**, 11102 (2013).

[169] L.M. Malard, M. A. Pimenta, G. Dresselhaus, and M.S. Dresselhaus, Phys. Rep. **473**, 51 (2009).

[170] A.K. Goetzberger, J. Knobloch, and B. Voss, *Crystalline Silicon Solar Cells* (Wiley, West Sussex, 1998).

[171] V. V. Brus, M. A. Gluba, X. Zhang, K. Hinrichs, J. Rappich, and N.H. Nickel, Phys. Status Solidi Appl. Mater. Sci. **211**, 843 (2014).

[172] S. Bae, H. Kim, Y. Lee, X. Xu, J.-S. Park, Y. Zheng, J. Balakrishnan, T. Lei, H. Ri Kim, Y. Il Song, Y.-J. Kim, K.S. Kim, B. Özyilmaz, J.-H. Ahn, B.H. Hong, and S. Iijima, Nat. Nanotechnol. **5**, 574 (2010).

[173] V. Yelundur, K. Nakayashiki, M. Hilali, and A. Rohatgi, in *Conf. Rec.*

Thirty-First IEEE Photovolt. Spec. Conf. 2005. (IEEE), pp. 959–962.

[174] J. Dore, R. Evans, U. Schubert, B.D. Eggleston, D. Ong, K. Kim, J. Huang, O. Kunz, M. Keevers, R. Egan, S. Varlamov, and M.A. Green, Prog. Photovoltaics Res. Appl. **21**, 1377 (2013).

[175] C. Becker, D. Amkreutz, T. Sontheimer, V. Preidel, D. Lockau, J. Haschke, L. Jogschies, C. Klimm, J.J. Merkel, P. Plocica, S. Steffens, and B. Rech, Sol. Energy Mater. Sol. Cells **119**, 112 (2013).

[176] J. Dore, R. Evans, B.D. Eggleston, S. Varlamov, and M.A. Green, MRS Proc. **1426**, 63 (2012).

[177] S. Kühnapfel, N.H. Nickel, S. Gall, M. Klaus, C. Genzel, B. Rech, and D. Amkreutz, Thin Solid Films **576**, 68 (2015).

[178] C. Ulbrich, A. Gerber, K. Hermans, A. Lambertz, and U. Rau, Prog. Photovoltaics Res. Appl. **21**, 1672 (2013).

[179] L. Mazzarella, S. Kirner, B. Stannowski, L. Korte, B. Rech, and R. Schlatmann, Appl. Phys. Lett. **106**, 23902 (2015).

[180] J.P. Thomas, S. Srivastava, L. Zhao, M. Abd-Ellah, D. McGillivray, J.S. Kang, M.A. Rahman, N. Moghimi, N.F. Heinig, and K.T. Leung, ACS Appl. Mater. Interfaces **7**, 7466 (2015).

[181] E. Van Kerschaver and G. Beaucarne, Prog. Photovoltaics Res. Appl. **14**, 107 (2006).

[182] J. Haschke, D. Amkreutz, L. Korte, F. Ruske, and B. Rech, Sol. Energy Mater. Sol. Cells **128**, 190 (2014).

[183] M. Junghanns, J. Plentz, G. Andrä, A. Gawlik, I. Höger, and F. Falk, Appl. Phys. Lett. **106**, 83904 (2015).

[184] K. Kawano, R. Pacios, D. Poplavskyy, J. Nelson, D.D.C. Bradley, and J.R.

Durrant, Sol. Energy Mater. Sol. Cells **90**, 3520 (2006).

[185] M. Jørgensen, K. Norrman, and F.C. Krebs, Sol. Energy Mater. Sol. Cells **92**, 686 (2008).

[186] R.A. Sinton and A. Cuevas, Appl. Phys. Lett. **69**, 2510 (1996).

Publications

Publications in the framework of this thesis

Peer-reviewed journal articles

M.Zellmeier, S. Kühnapfel, B. Rech, N.H. Nickel, and J. Rappich, "Enhanced Stability of P3HT/Poly-crystalline Si Thin Film Hybrid Solar cells," *Phys. Status Solidi A,* DOI:10.1002/pssa.201532772, 2016.

M. Zellmeier, J. Rappich, M. Klaus, C. Genzel, S. Janietz, J. Frisch, N. Koch, and N. H. Nickel, "Side chain engineering of poly-thiophene and its impact on crystalline silicon based hybrid solar cells," *Appl. Phys. Lett.*, vol. 107, no. 20, p. 203301, 2015.

V. V. Brus, M. Zellmeier, X. Zhang, S. M. Greil, M. Gluba, A. J. Töfflinger, J. Rappich, and N. H. Nickel, "Electrical and photoelectrical properties of P3HT/n-Si hybrid organic–inorganic heterojunction solar cells," *Org. Electron.*, vol. 14, no. 11, pp. 3109–3116, Nov. 2013.

Conference Contributions

Talks

M. Zellmeier; S. M. Greil; V. V. Brus; S. Janietz; J. Rappich; N. H. Nickel, "Alternatives to P3HT for silicon based organic-inorganic hybrid solar cells," Hybrid-Photovoltaics 2013 Berlin, 15.05.2013 - 17.05.2013 (2013)

M. Zellmeier; J. Frisch; S. Janietz; N. Koch; J. Rappich; N. H. Nickel; “Highly Efficient Silicon/Polythiophene Hybrid Solar Cell Devices;” DPG-Frühjahrstagung Dresden, 30.03.2014 - 04.04.2014 (2014)

M. Zellmeier; S. Janietz; S. Soulis; V. Syritski; K. Hinrichs; N. H. Nickel; J. Rappich: “Highly Efficient Silicon/Polythiophene Hybrid Solar Cell Devices;” Baltic Polymer Symposium, Laulasmaa, Estland, 24.09.2014 - 26.09.2014 (2014)

M. Zellmeier; T. Brenner; S. Janietz; N. H. Nickel; J. Rappich; “A Comparative Study of Polythiophene/c-Si Hybrid Solar Cells and Inorganic a-Si:H/c-Si Devices;” DPG Tagung 2015 Berlin, 15.02.2015 - 20.03.2015 (2015)

M. Zellmeier; S. Kühnapfel; J. Rappich; N.H. Nickel; “Enhanced stability of P3HT/polycrystalline silicon hybrid solar cells;” 26th International Conference on Amorphous and Nanocrystalline Semiconductors (ICANS 26) Aachen, Germany, 13.09.2015 - 18.09.2015 (2015)

J. Rappich; M. Zellmeier; F. Rösicke; K. Hinrichs; N. H. Nickel; “Passivation and functionalization of Silicon surfaces by small organic molecules and polymers;” Workshop: From materials to electro-optical devices Athen, Greece, 17.02.2015 - 17.02.2015 (2015)

S. Soulis; M. Zellmeier; G. Sun; K. Hinrichs; J. Rappich; “Electropolymerization of thiophene derivatives onto Si surfaces activated by interfacial layers for use in hybrid photovoltaic cells,” 7th International Symposium on Flexible Organic Electronics (ISFOE14) Thessaloniki, Greece, 09.07.2014 - 12.07.2014 (2014)

Poster

M. Zellmeier; M. Klaus; C. Genzel; S. Janietz; N. H. Nickel; J. Rappich; "Highly Efficient Silicon/Polythiophene Hybrid Solar Cell Devices," Hybrid and Organic Photovoltaics Lausanne, Schweiz, 11.05.2014 - 14.05.2014 (2014)

M. Zellmeier; S. Soulis; S. Janietz; N. H. Nickel; J. Rappich; "Interface Characterization of Silicon/Polythiophene Solar Cells using Spectral Response Measurements," 2014 MRS Fall Meeting & Exhibit Boston, Massachusetts, 30.11.2014 - 05.12.2014 (2014)

M. Zellmeier; S. Kühnapfel; J. Rappich; N.H. Nickel; "Hybrid P3HT/polycrystalline silicon solar cells;" Hybrid Photovoltaics 2015 Berlin, 10.12.2015 - 11.12.2015 (2015)

F. Lang; M. Zellmeier; M. A. Gluba; S. Albrecht; J. Rappich; L. Korte; B. Rech; N. H. Nickel; "Graphene on Hybrid Solar Cells: from Silicon and Perovskite towards Tandem Solar Cells," Hybrid Photovoltaics 2015 Berlin, 10.12.2015 - 11.12.2015 (2015)

S. Soulis; M. Zellmeier; G. Sun; K. Hinrichs; J. Rappich; "Modification of silicon surface by electrochemical Grignard reactions for hybrid photovoltaic cells." The 10th International Conference on Organic Electronics Modena, Iltalien, 11.06.2014 - 13.06.2014 (2014)

Acknowledgments

I would like to express my gratitude to my supervisors **Prof. Dr. Norbert H. Nickel**, **Dr. Jörg Rappich** and **Prof. Dr. Bernd Rech** from the Helmholtz-Zentrum Berlin, institute silicon photovoltaics. They gave me the opportunity to carry out this work and always had an open door to help me with any problem I encountered. I learned so much and like to thank them for that.

Just as much I would like to thank **Prof. Dr. Norbert Koch** for the supervision of this thesis on behalf of the Humboldt-University Berlin and **Dr. Johannes Frisch** for conducting the photoemission spectroscopy measurements as well as helpful discussions.

I´d like to thank **my colleagues** at the HZB for the good time and numerous discussions. I especially want to mention **Dr. Stefanie Greil** for the support and supervision at the beginning of the thesis, **Dr. Marc Gluba** for continuous help throughout the thesis and **Dr. Victor V. Brus**, whose work marked the start of my topic. And of course the helping hands of **Marion Krusche, Kerstin Jacob, Erhard Conrad** and **Thomas Lußky** for taking work off of me.

My friends **Kathi, Verena & Bacel, Sabi & Dominikus, Lisa & Phillipp, Gerald** and **Patti** for taking me in, having a beer with me, taking my mind of things or simply making my time in Berlin livable and never making me regret my decision to come here from the moment I moved.

But mostly I am thankful for the continuous and unconditional support of **my family** I can always be sure of.

Selbstständigkeitserklärung

Ich erkläre hiermit, dass ich die vorliegende Arbeit selbstständig verfasst habe und keine anderen als die angegebenen Quellen und Hilfsmittel verwendet habe.

Darüber hinaus versichere ich, mich nicht anderweitig um einen Doktorgrad beworben zu haben, oder einen Doktorgrad zu besitzen. Die dem Verfahren zu Grunde liegende Promotionsordnung der Mathematisch-Naturwissenschaftlichen Fakultät der Humboldt-Universität zu Berlin habe ich zur Kenntnis genommen.